# MOLECULAR MOTIONS AND CHARGE CARRIER DYNAMICS IN ELECTRIC FORCE MICROSCOPY

A Dissertation

Presented to the Faculty of the Graduate School

of Cornell University

in Partial Fulfillment of the Requirements for the Degree of

Doctor of Philosophy

by

Swapna Lekkala

August 2013

© 2013 Swapna Lekkala

ALL RIGHTS RESERVED

MOLECULAR MOTIONS AND CHARGE CARRIER DYNAMICS IN ELECTRIC FORCE MICROSCOPY

Swapna Lekkala, Ph.D.

Cornell University 2013

Since its invention in 1981 [4] by Gerd Binnig and Heinrich Rohrer, scanning probe microscopy is used to image a surface by probing various sample properties at resolutions from 100 nm to 1 Angstrom. In this work, the measurements of electric force microscopy where a cantilever oscillates above the sample are studied. A theoretical framework to calculate the experimental observables, noncontact friction and cantilever frequency fluctuations, is provided. The dynamical fluctuations probed by electric force microscopy are shown to be related to sample properties such as dielectric fluctuations, carrier dynamics, and Coulomb interactions between charge carriers. The theoretical calculations are compared to the measured data and found to be within reasonable error, on organic thin films, organic transistor and doped Si samples.

The cantilever frequency noise on organic thin films is shown to be from the dielectric fluctuations. A semi-infinite semiconductor is used as a model to study the effect of dielectric fluctuations, carrier dynamics, and inter-carrier interactions on frequency noise. A semi-infinite semiconductor model was developed which predicts a suppression in frequency noise with increase in carrier density, in disagreement with noise measurements on organic transistor where the frequency noise is independent of carrier density. The semi-infinite model is therefore extended to a layered structure, enabling the evaluation of the effects of finite thickness of semiconductor and the confinement of the charge

carriers to few monolayers close to the semiconductor-insulator interface in organic transistor. The layered structure explains the cantilever frequency noise measurements on an organic transistor, and predicts that noncontact friction measurements can be used to assess the effects of inter-carrier Coulomb interactions on charge motion in organic semiconductors. Noncontact friction data on doped Si has a one-over-square root dependence in charge density that is also explained by our semi-infinite model.

## BIOGRAPHICAL SKETCH

Swapna comes from Hyderabad, India, a city with bustling activity. She moved to the great Mumbai city to get an Integrated Masters degree in chemistry (5 years) at the Indian Institute of Technology(IIT), Mumbai. After research internships in organic chemistry at the Indian Institute of Sciences, experimental physical chemistry at the University of Bayreuth, and a masters project in molecular dynamics simulations of proteins at IIT, she decided to enter Cornell to pursue a Ph. D degree in theoretical chemistry. She will be moving to University of California at Irvine to work as a postdoctoral researcher.

This document is dedicated to my father.

# ACKNOWLEDGEMENTS

I greatly enjoyed doing science with my advisor Prof. Roger F Loring and I am indebted to my advisor for the immense help during my Ph. D. I also thank my reasearch co-advisor Prof. John A Marohn and his group, for all the help in providing experimental details and bringing to my notice the work of other groups.

I thank Prof. Greg Ezra, Prof. Ben Widom, and Prof. Roald Hoffmann for the inspiration. I thank my friends and family for all the support during these 5 years. My life at Cornell is enriched by various experiences (teaching and outdoor activities) and I thank all the people I met during this time.

## TABLE OF CONTENTS

Biographical Sketch . . . iii
Dedication . . . iv
Acknowledgements . . . v
Table of Contents . . . vi
List of Tables . . . viii
List of Figures . . . ix

**1 Introduction 1**
1.1 Electric force microscopy . . . 1
1.1.1 Parallel Motion . . . 4
1.1.2 Perpendicular Motion . . . 6
1.2 Experimental observables . . . 7
1.2.1 Noncontact friction . . . 7
1.2.2 Frequency jitter . . . 9
1.2.3 Anharmonic corrections . . . 11
1.3 Calculation of the potential auto-correlation function . . . 13

**2 Molecular motions probed by electric force microscopy 15**
2.1 Experiment . . . 16
2.2 Theoretical modelling . . . 16
2.3 Results and discussion . . . 21
2.4 Summary . . . 30

**3 Charge carrier dynamics and interactions in electric force microscopy 32**
3.1 Theoretical modelling . . . 33
3.1.1 Maxwell's equations coupled to charge transport . . . 33
3.2 Results and Discussion . . . 39
3.3 EFM measurements on an organic field effect transistor . . . 50
3.4 Summary . . . 58

**4 Quantitative comparison to measured data on an organic field-effect transistor and doped silicon 61**
4.1 Model I . . . 62
4.2 Model II . . . 65
4.3 Results and discussion . . . 67
4.3.1 Frequency Jitter . . . 67
4.3.2 Noncontact friction . . . 77
4.4 Summary . . . 88

**5 Concluding remarks 91**

**A appendix to chapter 3 93**

**B appendix to chapter 4** **96**

**Bibliography** **98**

## LIST OF TABLES

## LIST OF FIGURES

1.1 A schematic sketch of an electric force microscopy measurement. Cantilever tip is shown near a sample of dielectric layer of thickness $h$ on metal. The tip-sample height is $d$ and a voltage $V_{\mathrm{ts}}$ is applied between the cantilever tip and metal. The choice of coordinate system is as shown. Figure reproduced from Ref.[69], with permission. . . . . . . . . . . . . . . . . . . . . . . . . . 3

2.1 Electric force microscopy measurements on a thin layer of organic film of thickness $h$ over a conductor. The cantilever tip is positioned at a distance $d$ above the sample surface. The inset shows scanning electron microscope (SEM) image of the cantilever tip. The tip-radius is read as 40 nm from this image. Figure reproduced from Ref.[21], with permission. . . . . . . . . . . 17

2.2 Spectral density of cantilever frequency fluctuations at heights $d$ = 90 nm (blue, upper line) and 240 nm (red, lower line), for tip voltages ranging from −4 V to +4 V, measured on PVAc. A 1/f guideline is shown. Figure reproduced from Ref.[21], with permission. . . . . . . . . . . . . . . . . . . . . . . . . . . . . . . . 21

2.3 Cantilever frequency jitter as a function of tip voltage at various tip-sample separations (50 nm - ◇, 62 nm - ×, 90 nm - □, 180 nm - +, 240 nm - ∘). $J_L$ in A is integration from 0.4 to 3 Hz of L-region in Fig. (2.2) and $J_H$ in B is integration from 23 to 25 Hz of H-region in Fig. (2.2). Solid lines are fits to experimentally measured data: $J_L$ is $\propto V_{\mathrm{ts}}^2$ and $J_H$ is $\propto V_{\mathrm{ts}}^4$. Figure reproduced from Ref.[21], with permission. . . . . . . . . . . . . . . . . . . . 22

2.4 Measured capacitance second derivative, $C_2$, versus tip height (∘). The solid lines are the predicted contributions from a 40 nm sphere, a cone with a half angle of 16 deg, and both sphere plus cone. The dashed lines show predictions for a cone angle of 20 deg. Inset: Fit coefficient $c$ in $J_{\mathrm{H}} = c\, V_{\mathrm{ts}}^4$ from Fig. (2.3B) (circles) and prediction (line) from vibration noise determined by interferometry. Figure reproduced from Ref.[21], with permission. 24

2.5 Measured dielectric spectrum of PVAc. Figure reproduced from Ref.[21], with permission. . . . . . . . . . . . . . . . . . . . . . . . 25

2.6 Jitter measured (∘) on PVAc versus tip-sample height. Solid lines are jitter calculated from the sphere model of capacitance by integrating Eq. (2.23) from 0.4 to 3 Hz. The solid line (bottom) is calculated for an effective tip-sample height of $d + R$, with the total charge located at the centre of the sphere. The solid line (top) is for an effective tip-sample height of $d$ when the charge is located at the bottom of the sphere. The jitter is predicted to lie within the shaded grey region, in excellent agreement with experiment. The dashed lines add contributions from anharmonic tip-sample interactions to the solid lines. Figure reproduced from Ref.[21], with permission. . . . . 27
2.7 Total jitter calculated (topmost solid line) with an effective tip-sample height of $d$ and jitter data (∘) versus tip-sample height, drawn from Fig. (2.6). The rest of the lines are contributions to the total jitter (top most solid line) from individual terms in the power spectrum Eq. (2.23) integrated from 0.4 to 3 Hz. In increasing order of magnitude of contribution, these are: $J_0$ (dashed line), arising from the autocorrelation of voltage fluctuations, $J_1$ (dot-dashed line), from a cross-correlation of electric field and voltage fluctuations, $J_2$ (dotted line), arising from both the autocorrelation in electric field and cross-correlation of electric field gradient and voltage, $J_3$ (solid line with ∘), arising from a cross-correlation of electric field and electric field gradient, and $J_4$ (solid line with □), arising from autocorrelation of field gradient fluctuations. Figure reproduced from Ref.[21], with permission. . 29

3.1 Autocorrelation function of fluctuations in potential, denoted as $C_{00}(f)$ on the y-axis, vs. frequency, at a tip-sample height $d$ = 100 nm for charge carriers diffusing in vacuum. Solid curves for interacting carriers are calculated from Eq. (3.20) with $\epsilon_{\rm rel} = 1$, while dashed curves for non-interacting carriers are calculated using Eq. (3.28). The charge carrier densities are as indicated. Figure reproduced from Ref.[32], with permission. . . . . 40
3.2 Autocorrelation function of fluctuations in potential, denoted as $C_{00}(f)$ on the y-axis, vs. frequency, at a tip-sample height $d$ = 100nm for charge carriers diffusing in a dielectric medium. Various charge densities are indicated and the characteristic frequencies are marked $f_1$,$f_2$ and $f_3$. Details in text. Figure reproduced from Ref.[32], with permission. . . . . 41
3.3 Power spectrum of cantilever resonance frequency fluctuations denoted $P_{\delta f_c}(f)$ as a function of frequency, at a tip-sample height $d$ = 100 nm above the vacuum-sample interface for the same parameters as in Fig. (3.2). Figure reproduced from Ref.[32], with permission. . . . . 42

3.4 Power spectrum of cantilever resonance frequency fluctuations denoted $P_{\delta f_c}(f)$ as a function of frequency, at a tip-sample height $d$ = 100 nm above the vacuum-sample interface for various charge densities. The relative dielectric function has the Debye form with a relatively long relaxation time, $\tau$ = 20 s. Figure reproduced from Ref.[32], with permission. . . . . . . . . . . . . . . 45
3.5 Power spectrum of cantilever resonance frequency fluctuations denoted $P_{\delta f_c}(f)$ as a function of frequency, at a tip-sample height $d$ = 100 nm above the vacuum-sample interface for various charge densities. The relative dielectric function has the Debye form with a relatively short relaxation time, $\tau = 10^{-5}$ s. Figure reproduced from Ref.[32], with permission. . . . . . . . . . . . . . 46
3.6 The solid line shows cantilever frequency jitter as a function of tip-sample height for carrier density $\bar{\rho} = 10^{21}$ m$^{-3}$. Other lines indicate contributions to jitter from auto- and cross-correlation of fluctuations in potential, electric field, and electric field gradient (Eq. 1.30). Label $z,\phi$ is the crosscorrelation function of fluctuations in the $z$ component of the electric field and potential and, $zz,z$ is that of $z$-gradient of the $z$ component of the electric field and the $z$ component of the electric field. Details in text. Figure reproduced from Ref.[32], with permission. . . . . . . . . . . . . . 48
3.7 Cantilever frequency jitter is shown as a function of tip-sample separation. The charge carrier densities are as indicated. Jitter calculated from potential autocorrelation in Eq. (3.20) are the solid curves and jitter calculated from potential autocorrelation in Eq. (3.25) with an effective relative dielectric function that includes conductivity are the dashed curves. Both the calculations are in good agreement in the limit of large $d$. Figure reproduced from Ref.[32], with permission. . . . . . . . . . . . . . . . . . . . . . 49
3.8 Charged cantilever tip is positioned above an organic field-effect transistor. Figure reproduced from Ref.[32], with permission. . . 51
3.9 Measured power spectra of cantilever frequency fluctuations above an organic field effect transistor are shown for various tip-sample separations. The tip-sample and gate voltages are respectively $V_{\mathrm{ts}} = -3$ V and $V_G = -40$ V. The frequency dependence $f^{-1}$ is shown. Figure reproduced from Ref.[32], with permission. . . 52

3.10 Observed cantilever frequency noise (jitter) integrated from 0.2 Hz to 3.0 Hz as a function of tip sample distance $d$ above a TPD transistor. The frequency noise was measured at applied gate voltages of $V_G = 0$ (circles), $V_G = -20$ V (squares), $V_G = -40$ V (crosses), and, as a control experiment, over the source electrode (x). The jitter for $V_G = -40$ V is obtained from frequency integration of the spectra in Fig. 3.9. Also shown is a prediction from freely diffusing carriers in the absence of a dielectric (solid blue line). Figure reproduced from Ref.[32], with permission. . . 54
3.11 Voltage noise for a dielectric with mobile charges at $\bar{\rho} = 10^{18}$ m$^{-3}$ (dots) is similar at both low and high frequencies to the noise produced by dielectric relaxation alone at $\bar{\rho} = 0$ (dot-dash). Noise at $\bar{\rho} = 10^{18}$ m$^{-3}$ is overestimated at low frequency by a calculation based on diffusion of noninteracting carriers at the same density in vacuum (dashes). At a higher density $\bar{\rho} = 2.6 \times 10^{24}$ m$^{-3}$, the solid curve shows suppression of noise at low frequency. Figure reproduced from Ref.[32], with permission. 56

4.1 A sketch of model I where a point charge is located at a tip-sample separation $d$. The point charge here represents the cantilever tip. The sample is represented by a semiconductor layer of thickness $h_s$ on a semi-infinite dielectric base. The relative dielectric function of the semiconductor is $\epsilon_s(\omega)$, and that of the base is $\epsilon_d(\omega)$. . . . . . . . . . . . . . . . . . . . . . . . . . . . . 64
4.2 A sketch of model II where a point charge is located at a tip-sample separation $d$. The point charge in the model is at the locaton of the cantilvere tip in EFM. The sample is represented by a dielectric overlayer of thickness $h_d$ on a semi-infinite semiconductor. The relative dielectric function of the semiconductor is $\epsilon_s(\omega)$, and that of the dielectric overlayer is $\epsilon_d(\omega)$. . . . . . . . . 66
4.3 (a) Power spectrum of frequency fluctuations vs. frequency at a tip-sample height of $d = 100$ nm calculated from model I for different carrier densities. (b) Integrated cantilever frequency jitter for different charge densities. Following parameters were used in the calculations from model I in (a) and (b): semiconductor thickness $h_s = 70$ nm, carrier mobility $\mu = 2.7 \times 10^{-10}$ m$^2$V$^{-1}$s$^{-1}$, semiconductor dielectric function $\epsilon_{rel} = 3.4 - i\ 0.05$, dielectric constant of $SiO_2$ base $\epsilon_d = 4.85$, tip-radius $R = 40$ nm, cantilever resonance frequency $f_c = 65$ kHz, and tip-sample voltage $V_{ts} = 3$ V. . . . . . . . . . . . . . . . . . . . . . . . . . . . . . . . . . . 68

4.4 The power spectrum of frequency fluctuations vs. frequency at a tip-sample height of $d$ = 100 nm from model I for different thicknesses $h_s$ of the semiconductor layer. The carrier density corresponds to a gate voltage of −40 V, $\rho = 5.2 \times 10^{24}$ m$^{-3}$. All the other parameters are the same as listed for Fig. (4.3a). . . . . . . 71
4.5 (a) The power spectrum of cantilever frequency fluctuations vs. frequency at tip-sample height of $d$ = 100 nm shown for model II for different charge carrier densities. (b) Integrated cantilever frequency jitter for different charge densities. The following parameters were used in the calculations from model II in (a), and (b): the thickness of the dielectric overlayer is $h_d$ = 69 nm, the dielectric function of the dielectric and the semiconductor are taken to be $\epsilon_{rel} = \epsilon_d = 3.5 - i\,0.05$, and the rest of the parameters are the same as in Fig. (4.3a). . . . . . . . . . . . . . . . . . . . . . 72
4.6 The power spectrum of cantilever frequency fluctuations vs. frequency at a tip-sample height of $d$ = 100 nm from model II for different thicknesses $h_d$ of the dielectric overlayer. The carrier density is corresponding to a gate voltage of −40 V, $\rho$ = $5.2 \times 10^{24}$ m$^{-3}$. All the other parameters are the same as listed for Fig. (4.3a). . . . . . . . . . . . . . . . . . . . . . . . . . . . . . 74
4.7 Measured cantilever frequency jitter $J_\perp$ for a gate voltage of $V_G$ = −40 V in organic transistor shown as solid dots. The data for gate voltages $V_G$ = −20 V, and $V_G$ = 0 are indistinguishable from the solid dots, and are shown in Fig. (3.10), but not included here. The solid and the dashed lines are calculated from model II for a carrier density $\rho = 5.2 \times 10^{24}$ m$^{-3}$, corresponding to a gate voltage of $V_G$ = −40 V. A relative dielectric function of $\epsilon_s = \epsilon_d = 3.4 - i\epsilon''_s$ with $\epsilon''_s$ as indictaed, is used in the calculation of these lines. The $J_\perp$ result from a different carrier density $\rho = 1.6 \times 10^{24}$ m$^{-3}$ corresponding to $V_G$ = −20 V, is indistinguishable from these lines. The parameters used are relevant to the transistor measurements in Sec. 3.3: the dielectric overlayer has thickness $h_d$ = 69 nm, the carrier mobility is $2.7 \times 10^{-10}$ m$^2$V$^{-1}$s$^{-1}$, and all the other parameters have the same values as in Fig. (4.3). 76
4.8 Noncontact friction for the parallel motion of the cantilever calculated from Eq. (4.15) for a semi-infinite seniconductor. (a) $\gamma_\parallel$ vs. carrier density for different values of dispersion $\epsilon''_s$ in the relative dielectric function of the semiconductor $\epsilon_{rel} = 11.9 - i\,\epsilon''_s$. The carrier mobility is $\mu = 10^{-5}$ m$^2$V$^{-1}$s$^{-1}$ . (b) $\gamma_\parallel$ vs. carrier density for various mobility values are shown. The relative dielectric function $\epsilon_s = 3.4 - i\,0.05$. In (a) and (b), the experimental constants are tip-sample radius $R$ = 80 nm, cantilever frequency $f_c$ = 81 kHz, and tip-sample voltage $V_{ts}$ = 3 V. . . . . . . . . . . . . . . . . . . 78

4.9 Noncontact friction of doped Si vs. doping density at a tip-sample height $d$ = 300 nm. Measured friction values for electrons(squares), and holes(circles) are obtained from Refs.[57, 56]. The curves are calculated from Eq. (4.15), with $\epsilon_s''$ as indicated. The carrier density used in the calculations is equal to the dopant density. The tip-sample voltage is $V_{ts}$ = 2 V. The rest of the parameters are the same as Fig. (4.8), and the experiment. . . . . . . 82
4.10 Noncontact friction vs. tip-sample height $d$. Dots are the measured friction data from Ref.[57], and the solid line is the friction calculated from Eq. (4.15) for a carrier density of $\rho = 1.4\times10^{23}\mathrm{m}^{-3}$. The hole mobility in Si, $\mu = 0.045\,\mathrm{m}^2\mathrm{V}^{-1}\mathrm{s}^{-1}$, $\epsilon''_{\mathrm{rel}} = 5$, and $V_{ts} = -2$ V are used in the calculation. . . . . . . . . . . . . . . . . . . . . . . . 84
4.11 Noncontact friction for the perpendicular motion of the cantilever calculated from model II in Sec. 4.2, for an organic transistor. (a) $\gamma_\perp$ vs. carrier density for different carrier mobilities as indicated, with relative dielectric function of the semiconductor and the dielectric overlayer $\epsilon_d = \epsilon_s = 3.4 - i\ 0.05$. Red vertical lines on the $x$-axis correspond to the carrier densities estimated from gate voltages $V_G = -20, -40$ V, explained in the text. (b) $\gamma_\perp$ for various dispersion values $\epsilon_s''$ in the relative dielectric function $\epsilon_d = \epsilon_s = 3.4 - i\ \epsilon_s''$, and $\mu = 2.7\times10^{-10}\ \mathrm{m}^2\mathrm{V}^{-1}\mathrm{s}^{-1}$. The rest of the parameters are in the text. . . . . . . . . . . . . . . . . . . . . . . . . 86

CHAPTER 1

# INTRODUCTION

## 1.1 Electric force microscopy

Electric Force Microscopy (EFM)[33, 34, 37] employs of a charged cantilever tip oscillating above the surface of a sample. In this work, we show that the cantilever tip is capable of measuring the dynamical fluctuations from molecular motions and carrier dynamics in the sample. This capability is illustrated in Chapters 2, 3 and 4. Noncontact friction and cantilever frequency fluctuations are the two experimentally measured observables. Noncontact friction is measured by driving the cantilever at its resonance frequency $\omega_c$, turning off the drive, and recording the following decay of the amplitude.[30, 31]. This noncontact friction is related to the time-varying random forces from the sample by fluctuation-dissipation theorem, and is further discussed in Sec. 1.2.1. In EFM, the cantilever frequency vs. time is measured, fluctuations of the cantilever frequency about the mean value are calculated, and a power spectrum of frequency fluctuations is computed. Frequency jitter is calculated from the power spectrum of frequency fluctuations by integrating over the frequency range of corresponding to the measurement bandwidth of the experiment. The frequency jitter measurements are shown to be related to fluctuations in the potential, electric field, and its derivatives produced by the sample in Sec. 1.2.2.

In Chapter 2, a theoretical basis for measurements on organic polymers is provided, and the source of dynamical fluctuations is shown to be thermal dielectric fluctuations in the polymer film. In Chapter 3, the theoretical treatment to calculate the cantilever frequency fluctuations for an organic transistor is de-

veloped that is applicable when both dielectric and charge density fluctuations are present. In Chapter 4, a quantitative comparison is made to both measured noncontact friction data on doped Si and frequency jitter data on organic transistor. Noncontact friction calculations for organic transistor are also presented in Chapter 4.

Two geometries of measurement are possible with EFM: the tip oscillation may be either parallel [26, 30, 31, 58, 67, 68, 69] or perpendicular [20, 21] to the plane of vacuum-sample interface. Parallel motion measurements use ultrasensitive cantilevers and are only available to few groups, while the perpendicular motion uses widely available commercial cantilevers. Secs. 1.1.1 and 1.1.2 show the basic assumptions involved in determining noncontact friction and frequency jitter for these two geometries. In each geometry the cantilever is maintained above the sample in a noncontact mode. Fig. (1.1) shows the choice of coordinate system and the cantilever tip and sample alignment for the parallel-motion case. The vacuum-sample interface is parallel to the $xy$ plane (located at $z = 0$) and $z < 0$ corresponds to the sample. The equilibrium position of the cantilever is maintained at $x = 0$, $y = 0$, and $z = d$. A tip-sample voltage $V_{\mathrm{ts}}$ is applied between the cantilever tip and the metal layer below the sample. In the parallel-motion experiment, the tip motion is taken to be one-dimensional along $x$, referred to as parallel motion. The tip-sample height $d$ remains approximately constant during the motion and the cantilever can be thought of as oscillating in a plane parallel to the vacuum-sample interface at a tip-sample height of $d$. Since the tip-sample height remains constant, the tip-sample capacitance in this geometry is constant for a fixed tip-voltage $V_{\mathrm{ts}}$, and so the charge on the tip is constant. In the perpendicular motion experiment, the tip motion is one-dimensional along $z$. The tip-sample height varies during the perpendic-

ular motion while the cantilever tip is oscillating along a normal ($z$-axis) to the vacuum-sample interface ($xy$-plane). In this geometry, the tip-sample capacitance varies as a function of tip-sample height, and consequently the tip charge varies during the cantilever oscillation.

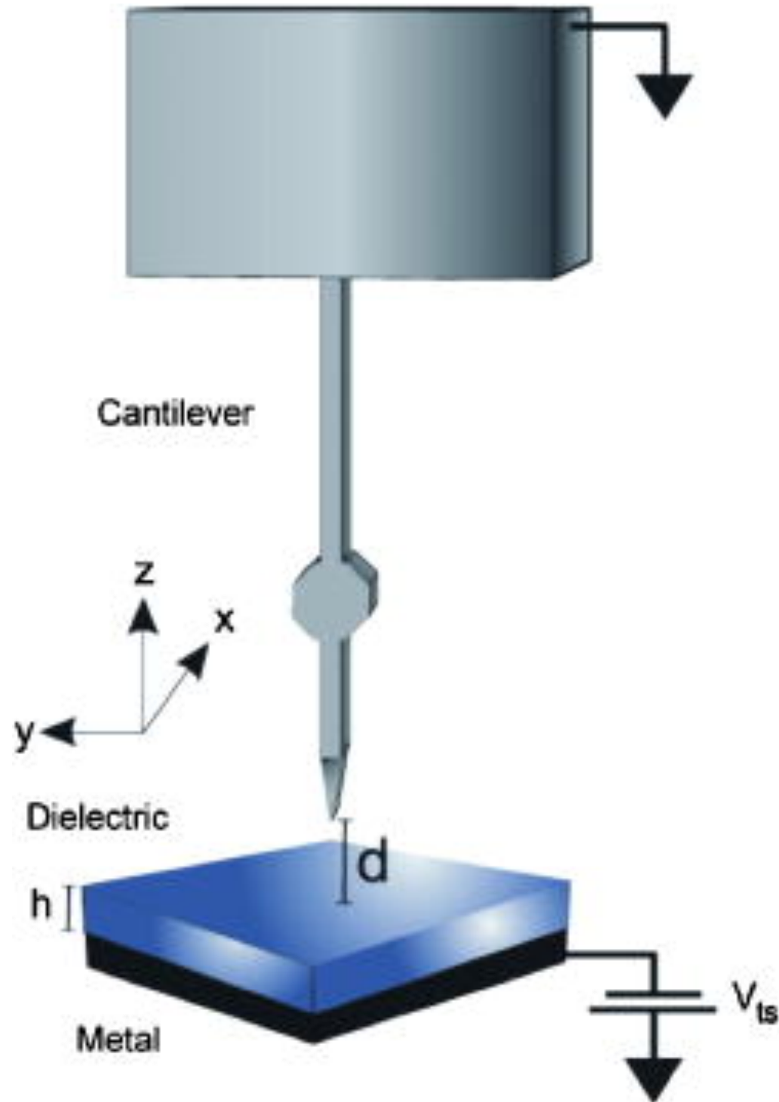


Figure 1.1: A schematic sketch of an electric force microscopy measurement. Cantilever tip is shown near a sample of dielectric layer of thickness $h$ on metal. The tip-sample height is $d$ and a voltage $V_{\rm ts}$ is applied between the cantilever tip and metal. The choice of coordinate system is as shown. Figure reproduced from Ref.[69], with permission.

### 1.1.1 Parallel Motion

In this geometry of EFM, the cantilever oscillation is approximated to be along the $x$-axis. The cantilever tip is modelled as a point charge, oscillating with cantilever resonance frequency $f_c \equiv \omega_c/2\pi$, experiencing noncontact friction $\gamma$ and a time-varying capacitive force $F_x$ from the sample. The equation of motion of this point charge oscillating along the $x$-direction is given by the Langevin equation [30, 31, 67, 68, 69],

$$m\ddot{x} = -m\omega_c^2 x - \gamma x + F_x, \tag{1.1}$$

$$F_x = -\frac{\partial W(x,t)}{\partial x}, \tag{1.2}$$

$$W(x,t) = \frac{1}{2}c(z)(V_{\text{ts}} + \varphi(x,t))^2, \tag{1.3}$$

where $m$ is the effective mass related to the cantilever force constant by $m \equiv k_c/\omega_c^2$, $W(x,t)$ is the capacitor energy of the tip-sample arrangement, the tip-sample voltage $V_{\text{ts}} = V_{\text{app}} - \phi_c$ is the applied voltage adjusted for the measured surface contact potential $\phi_c$, $c(z)$ is the capacitance of the cantilever tip and sample separated by a distance $z$, and $\varphi(x,t)$ is the time-varying fluctuating potential due to the sample at the tip location $(x,y,z) \equiv (x,0,d)$. The angular resonance frequency in Eq. (1.1) is $\omega_c = 2\pi f_c$. In the experiment, the applied tip-sample voltage is much greater than the fluctuating sample-induced potential, $V_{\text{ts}} >> \varphi$ and so Eq. (1.3) is written as [21, 69, 67],

$$W \approx \frac{1}{2}c(z)V_{\text{ts}}^2 + q_c\varphi(x,t), \tag{1.4}$$

and the capacitive force at the cantilever tip from Eq. (1.2) is,

$$F_x = -q_c\frac{\partial\varphi(x,t)}{\partial x}, \tag{1.5}$$

where $q_c \equiv c(d)V_{\text{ts}}$. The fluctuating sample-induced potential in Eq. (1.4) is written as a sum of an average electrostatic potential $\phi(x)$ and a quantity fluctuating

in time $\delta\varphi(x,t)$.

$$\begin{aligned}\varphi(x,t) &= \phi(x) + \delta\varphi(x,t),\\ \phi(x) &= \langle\varphi(x,t)\rangle.\end{aligned} \tag{1.6}$$

The average electrostatic potential $\phi(x)$ and fluctuating quantity $\delta\varphi(x,t)$ are Taylor expanded about $x = 0$.

$$\begin{aligned}\phi(x) &\approx \phi(0) - \frac{x^2}{2}E_{xx},\\ \delta\phi(x,t) &\approx \delta\phi(t) - x\,\delta\mathcal{E}_x(t) - \frac{x^2}{2}\,\delta\mathcal{E}_{xx}(t),\end{aligned} \tag{1.7}$$

where the average electric field $E_x$ from the sample at cantilever equilibrium position (0,0,$d$) is 0 due to the assumed lateral symmetry of the sample. The $x$-gradient of the average electric field in the $x$-direction is $E_{xx} \equiv \partial^2\phi(x)/\partial x^2|_{x=0}$. The fluctuating potential in time is $\delta\phi(t) \equiv \delta\phi(x,t)|_{x=0}$, the fluctuating electric field in $x$-direction is $\delta\mathcal{E}_x(t) \equiv \partial\delta\phi(x,t)/\partial x|_{x=0,y=0,z=d}$, and the fluctuating $x$-gradient of the $x$ component of the electric field is $\delta\mathcal{E}_{xx}(t) \equiv \partial^2\delta\phi(x,t)/\partial x^2|_{x=0,y=0,z=d}$. Using Eqs. (1.6) and (1.7), the capacitive force in Eq. (1.5) is linearized in $x$ and written in terms of a static shift in resonance frequency $\Delta f_c$, a time-varying fluctuating resonant frequency $\delta f_c(t)$, and a random time-varying force $\delta F(t)$ as follows [30, 31, 67, 68, 69],

$$F_x = \delta F(t) - \left(\frac{2k_c x}{f_c}\right)(\Delta f_c + \delta f_c(t)), \tag{1.8}$$

$$\Delta f_c = -\frac{f_c q_c E_{xx}}{2k_c}, \tag{1.9}$$

$$\delta f_c(t) = \frac{f_c q_c\,\delta\mathcal{E}_{xx}(t)}{2k_c}, \tag{1.10}$$

$$\delta F(t) = q_c\,\delta\mathcal{E}_x(t). \tag{1.11}$$

Section 1.2 shows how the experimental observables, non-contact friction and frequency jitter, may be determined for parallel motion from Eqs. (1.10) and (1.11).

### 1.1.2 Perpendicular Motion

Similar equations as in Sec. 1.1.1 can be written for a cantilever tip modelled as a point charge oscillating along the $z$-axis, normal to the vacuum-sample interface. The equation of motion of this point charge is [21, 20, 32]

$$\begin{aligned} m\ddot{z} &= -m\omega_c^2(z-d) - \gamma\dot{z} - \frac{\partial W(z,t)}{\partial z}, &(1.12)\\ W(z,t) &= -\frac{1}{2}c(z)(V_{\rm ts} - \delta\varphi(z,t))^2, &(1.13)\\ &\approx -\frac{1}{2}c(z)V_{\rm ts}^2 + c(z)V_{\rm ts}\,\delta\varphi(z,t). &(1.14)\end{aligned}$$

Here the time-varying fluctuating potential from the sample $\delta\varphi(z,t)$ is at $(x,y,z) \equiv (0,0,z)$, and the electrostatic interaction with the sample is modelled by a stochastic potential energy $W(z,t)$ [27]. The term with squared potential fluctuations obtained from expansion of Eq. (1.13) is neglected in Eq. (1.14) because the squared of the fluctuating potential is negligible in comparison to the other terms. This $W(z,t)$ differs from $W(x,t)$ in its dependence on tip-sample height. Here the tip-sample voltage $V_{\rm ts} = V_{\rm app} - \phi_c$ is the applied voltage adjusted for the surface contact potential $\phi_c$ from measurements. Since the tip-sample distance $z$ varies during perpendicular motion, the capacitance is also Taylor expanded about the equilibrium tip-sample distance at $z = d$,

$$\begin{aligned} \delta\varphi(z,t) &\approx \delta\phi(t) - (z-d)\delta\mathcal{E}_z(t) - \frac{(z-d)^2}{2}\delta\mathcal{E}_{zz}(t),\\ c(z) &\approx c(d) + (z-d)c^{(1)}(d) + \frac{(z-d)^2}{2}c^{(2)}(d), &(1.15)\end{aligned}$$

where the fluctuating potential in time is $\delta\phi(t) \equiv \delta\phi(z,t)|_{z=d}$, the fluctuating average electric field in $z$-direction is $\delta\mathcal{E}_z(t) \equiv \partial\delta\phi(z,t)/\partial z|_{z=d}$, and the fluctuating $z$-gradient of the $z$ component of the electric field is $\delta\mathcal{E}_{zz}(t) \equiv \partial^2\delta\phi(z,t)/\partial z^2|_{z=d}$. The capacitance at a tip-sample height $z = d$ is $c(d)$, and the first and second

derivatives of capacitance at $d$ are $c^{(1)}(d)$ and $c^{(2)}(d)$, respectively. The force $F_z \equiv -\partial W(z,t)/\partial z$ is then linearized and written in the following form

$$F_z = F_c + \delta F(t) - \frac{2k_c(z-d)}{f_c}(\Delta f_c + \delta f_c(t)), \tag{1.16}$$

in terms of a static shift in resonant frequency $\Delta f_c$ and a dynamic fluctuating shift in resonant frequency $\delta f_c(t)$.

$$\Delta f_c = -\frac{f_c}{4k_c} V_{\text{ts}}^2 \, c^{(2)}(d), \tag{1.17}$$

$$\delta f_c(t) = -\frac{f_c}{2k_c}(-V_{\text{ts}} \, c^{(2)}(d) \, \delta\phi(t) + 2V_{\text{ts}} \, c^{(1)}(d) \, \delta\mathcal{E}_z(t) + V_{\text{ts}} \, c(d) \, \delta\mathcal{E}_{zz}(t)). \tag{1.18}$$

$$F_c = \frac{1}{2} c^{(1)}(d) V_{\text{ts}}^2, \tag{1.19}$$

$$\delta F(t) = -V_{\text{ts}} \, c^{(1)}(d) \, \delta\phi(t) + V_{\text{ts}} \, c(d) \, \delta\mathcal{E}_z. \tag{1.20}$$

$F_c$ in Eq. (1.19), which is independent of both time and coordinate, is a term that introduces a sample-induced shift in the equilibrium height of the cantilever tip. In the parallel motion case, the terms responsible for such a shift vanish. $\delta F(t)$ in Eq. (1.20) fluctuates in time, and represents the random force in the Langevin equation that is related to friction by the fluctuation-dissipation theorem. Sec. 1.2 shows how the experimental observables, noncontact friction and frequency jitter, may be determined for perpendicular motion from Eqs. (1.18) and (1.20).

## 1.2 Experimental observables

### 1.2.1 Noncontact friction

Using the point-charge models for parallel and perpendicular motions of the cantilever described in Secs. 1.1.1 and 1.1.2 respectively, the experimental observables, noncontact friction and frequency jitter, are calculated in this section

under the linear response assumption. In the past decade, noncontact friction on various samples has been measured experimentally using AFM cantilevers [40, 57], and also studied theoretically [30, 31, 43, 52, 55, 69]. The cantilever tip is modelled as a harmonic oscillator experiencing time-varying random forces from the sample as in Eqs. (1.1) and (1.12). The spectral density of random force fluctuations at the cantilever tip $C_{\delta F \delta F}(f_c)$ is related to noncontact friction by the fluctuation-dissipation theorem [15, 16, 22, 30, 31, 40, 45, 55, 57, 69],

$$\gamma = \frac{C_{\delta F\, \delta F}(f_c)}{k_B T}, \tag{1.21}$$

$$C_{\delta F\, \delta F}(f_c) = \int_0^\infty \cos(2\pi f_c t)\, \langle \delta F(t)\, \delta F(0) \rangle dt, \tag{1.22}$$

where the random force $\delta F(t)$ at the cantilever tip in parallel and perpendicular motion are given in Eqs. (1.11) and (1.20), respectively. For parallel motion, $\delta F(t)$ is given by Eq. (1.11), and consequently the noncontact friction in Eq. (1.21) is written in terms of the auto-correlation function of electric field fluctuations in the $x$ direction at the equilibrium position of the tip.

$$\gamma_{\|} = \frac{q_c^2}{k_B T} C_{\delta E_x\, \delta E_x}(f_c). \tag{1.23}$$

The cosine transform of the auto-correlation function of the electric field fluctuations at frequency $f = f_c$ is denoted by $C_{\delta E_x\, \delta E_x}(f_c)$ and is given by

$$C_{\delta E_x\, \delta E_x}(f_c) \equiv \left( \frac{\partial^2}{\partial x_1 \partial x_2} C_{\delta\phi\, \delta\phi}(\mathbf{r_2}, d, \mathbf{r_1}, d; f_c) \right)_{\mathbf{r_1}=\mathbf{r_2}=\mathbf{0}}, \tag{1.24}$$

where

$$C_{\delta\phi\, \delta\phi}(\mathbf{r_2}, z_2, \mathbf{r_1}, z_1; f) \equiv \int_0^\infty \cos(2\pi f t)\, \langle \delta\phi(\mathbf{r}_2, z_2, t)\, \delta\phi(\mathbf{r}_1, z_1 0) \rangle dt. \tag{1.25}$$

Here, $C_{\delta\phi\, \delta\phi}(\mathbf{r_2}, z_2, \mathbf{r_1}, z_1; f)$ is the cosine transform of the auto-correlation function of potential fluctuations at two different locations $(\mathbf{r}_2, z_1)$ and $(\mathbf{r}_2, z_2)$, and $\mathbf{r}_\mathrm{i}$ ($\equiv (x_\mathrm{i}, y_\mathrm{i})$) is the vector parallel to the interface and $z_\mathrm{i}$ is the height above the sample surface.

Similarly, for perpendicular motion $\delta F(t)$ is given by Eq. (1.20), and noncontact friction from Eq. (1.21) is written in terms of the auto-correlation, cross-correlation functions of potential and electric field fluctuations at the tip as

$$\gamma_\perp \equiv \frac{V_{ts}^2}{k_B T}\left[c^2(d)\, C_{\delta E_z\,\delta E_z}(d,d,\omega_c) + \left(c^{(1)}(d)\right)^2 C_{\delta\phi\,\delta\phi}(d,d,\omega_c) - 2c(d)\, c^{(1)}(d)\, C_{\delta\phi\,\delta E_z}(d,d,\omega_c)\right], \tag{1.26}$$

where $C_{\delta E_z\,\delta E_z}$ is the cosine transform of the auto-correlation function of electric field fluctuations in $z$-direction, $C_{\delta\phi\,\delta\phi}$ is the cosine transform of the potential auto-correlation and $C_{\delta\phi\,\delta E_z}$ is the cosine transform of the cross-correlation of the potential and the $z$ component of the electric field fluctuations. These correlation functions are obtained from the potential auto-correlation by taking the appropriate number of derivatives using

$$C_{nm}(z_1, z_2, f) \quad = \quad \frac{\partial^{n+m}}{\partial z_1^m \partial z_2^n} C_{\delta\phi\,\delta\phi}(\mathbf{r}_1 = 0, z_1, \mathbf{r}_2 = 0, z_2, f). \tag{1.27}$$

From Eq. (1.27) all the correlation functions in Eq. (1.26) are determined; $C_{\delta E_z\,\delta E_z}(d,d,f_c) \equiv C_{11}(z_1,z_2,f)|_{z_1=d,z_2=d,f=f_c}$, $C_{\delta\phi\,\delta E_z}(d,d,f_c) \equiv C_{01}(z_1,z_2,f)|_{z_1=d,z_2=d,f=f_c}$ and $C_{\delta\phi\,\delta\phi}(d,d,f_c) \equiv C_{00}(z_1,z_2,f)|_{z_1=d,z_2=d,f=f_c}$. Eqs. (1.24) and (1.27) show that all the correlation functions in Eqs. (1.23) and (1.26) of the noncontact friction follow from the two-point (at $(\mathbf{r}_1, z_1)$ and $(\mathbf{r}_2, z_2)$) correlation function of potential fluctuations. The model for the calculation of this potential correlation function is shown in Sec. 1.3. Chapter 4 shows friction calculations from Eqs. (1.23) and (1.26), for doped Si and organic semiconductors.

### 1.2.2 Frequency jitter

The second experimental observable of interest is fluctuations in the cantilever frequency. This is calculated for both parallel and perpendicular motions from

Eqs. (1.10) and (1.18), respectively. In this work, the calculations and measurements of cantilever frequency fluctuations for perpendicular motion of the cantilever are shown. Previous theoretical and experimental efforts for parallel motion measurements have shown that EFM is capable of sensing dielectric fluctuations from organic thin-film polymers [67, 68, 69]. In EFM, the fluctuations in cantilever resonance frequency are measured in time. A record of cantilever frequency versus time is converted into the power spectrum of frequency fluctuations as discussed in Ref. [20]. Frequency jitter is the area under this power spectrum in the experimental frequency range $f_{\min}$ to $f_{\max}$.

$$\text{Jitter} = \int_{f_{\min}}^{f_{\max}} df P_{\delta f_c}(f). \tag{1.28}$$

where $P_{\delta f_c}(f)$ is the power spectrum of cantilever frequency fluctuations,

$$P_{\delta f_c}(f) \equiv 4 \int_0^{\infty} dt \cos(2\pi f t) \, \langle \delta f_c(t) \, \delta f_c(0) \rangle. \tag{1.29}$$

The factor of 4 in Eq. (1.29) insures the normalization $\int_0^{\infty} df P_{\delta f_c}(f) = \langle (\delta f_c)^2 \rangle$. Within a harmonic approximation, the cantilever in perpendicular motion is modelled in Sec. 1.1.2. The expression for cantilever resonance frequency fluctuations thus obtained in Eq. (1.18) is used to write $P_{\delta f_c}(f)$ in terms of autocorrelation and cross-correlation functions of the potential, the electric field, and electric field derivatives [21, 32],

$$\begin{aligned} P_{\delta f_c}(f) = \left(\frac{f_c V_{\text{ts}}}{k_c}\right)^2 \Big[ & (c^{(2)}(d))^2 C_{\delta\phi\,\delta\phi}(d,d,f) + 4c^{(1)}(d)c^{(2)}(d) C_{\delta E_z\,\delta\phi}(d,d,f) \\ & +2c^{(0)}(d)c^{(2)}(d) C_{\delta E_{zz}\,\delta\phi}(d,d,f) + 4\left(c^{(1)}(d)\right)^2 C_{\delta E_z\,\delta E_z}(d,d,f) - 4c(d)c^{(1)}(d) C_{\delta E_z\,\delta E_{zz}}(d,d,f) \\ & +c^{(2)}(d) C_{\delta E_{zz}\,\delta E_{zz}}(d,d,f) \Big]. \end{aligned} \tag{1.30}$$

The correlation functions of fluctuations in potential and potential gradients are determined from Eq. (1.27). For example, $C_{\delta E_{zz}\,\delta E_{zz}}(d,d,f) \equiv C_{22}(z_1,z_2,f)|_{z_1=d,z_2=d,f}$, $C_{\delta E_{zz}\,\delta E_z}(d,d,f) \equiv C_{21}(z_1,z_2,f)|_{z_1=d,z_2=d,f}$, and so on. The experimental observables, noncontact friction in Eqs. (1.23) and (1.26) and frequency jitter in Eqs.

(1.28) and (1.30), only require calculating the cosine transform of the potential auto-correlation function in Eq. (1.25). The rest of the auto- and cross-correlation functions are calculated from the potential auto-correlation by taking derivatives using Eq. (1.27). In Sec. 1.3, the calculation of this potential auto-correlation in Eq. (1.25) is the main focus.

### 1.2.3 Anharmonic corrections

The anharmonic correction to the fluctuating frequency shift in Eq. (1.18) from the higher order terms in the expansion of stochastic potential energy $W(z,t)$ is shown in this section. The stochastic potential energy $W(z,t)$ in Eq. (1.14) is written as the sum of a static and a fluctuating term,

$$\begin{aligned} W(z,t) &\approx \overline{W}(z) + \delta W(z,t), &(1.31)\\ \overline{W}(z) &\equiv -\frac{1}{2}c(z)V_{\mathrm{ts}}^2, &(1.32)\\ \delta W(z,t) &\equiv c(z)V_{\mathrm{ts}}\,\delta\varphi(z,t). &(1.33)\end{aligned}$$

Expansion of $\overline{W}(z)$ about the equlibrium coordinate $z = d$ is written in terms of derivatives denoted as $\overline{W}_{\mathrm{n}}(d) \equiv d^n\overline{W}(z)/dz^n|_{z=d}$, and similarly $\delta W(z,t)$ has been expanded in terms of the derivatives $\delta W_{\mathrm{n}}(z,t) \equiv d^n\delta W(z)/dz^n|_{z=d}$. The anharmonic corrections are introduced to the time-varying shift in frequency in Eq. (1.18) as follows,

$$\begin{aligned}\delta f_c(d,t) = \frac{f_{\mathrm{c}}}{2k_{\mathrm{c}}}\Big[&\delta W_2(d,t) + k_c^{-1}(\overline{W}_3(d)\delta W_1(d,t) + \overline{W}_1(d)\delta W_3(d,t))\\ &-\frac{5z_{\mathrm{rms}}^2}{6}\overline{W}_3(d)\delta W_3(d,t) + \frac{z_{\mathrm{rms}}^2}{4}\delta W_4(d,t)\Big]. \qquad (1.34)\end{aligned}$$

Here, $\delta W_2(d,t)$ is the time-varying shift introduced by $W(z,t)$ in the harmonic approximation. Terms two and three involving the product of $W_1$ and $W_3$ are terms

obtained when the shift in the equilibrium height induced by the $W_1(d,t)$ term is introduced to $z-d$, and the cubic anharmonic term from $W_3(d,t)$ is rearranged for this shift. The fourth term, the product of $\overline{W}_3$ and $\delta W_3(d,t)$, is the second order perturbation correction of the cubic anharmonicity in the adiabatic approximation where potential energy fluctuations of $\delta W_3(d,t)$ are considered slow compared to the time period of oscillation. The adiabatic approximation is valid here because the majority of sample-induced cantilever frequency fluctuations occur on time scales four order of magnitude smaller than the cantilever period. This term is calculated using time-independent perturbation theory for the $W_3$ term [19], and extending this result to a slow time-varying term, $W_3(d,t)$. The fifth term in Eq. (1.34) is the first order perturbation correction from the quartic term to the time-varying shift in frequency [42], calculated under the same adiabatic approximation. The last two perturbation corrections are proportional to $z_{\mathrm{rms}}^2$, the mean-squared displacement of the cantilever from its equilibrium position, and it is equivalent to half of the squared amplitude.

The measured frequency jitter on all the samples in this work [21, 32] is observed to be proportional to $V_{\mathrm{ts}}^2$, and hence arises from terms that are linear in $V_{\mathrm{ts}}$ in Eq. (1.34). The terms containing $W_3$ are proportional to $V_{\mathrm{ts}}^3$, and so do not contribute to the measured jitter. The harmonic term $\delta W_2(d,t)$, and the quartic term $\propto \delta W_4(d,t)$, are linear in $V_{\mathrm{ts}}$. The quartic term is $\propto z_{\mathrm{rms}}^2$. While this term is not necessarily negligible, it was measured to be small at even the smallest tip-sample separations (Supporting Information of Ref. [21]). The amplitude dependence, and the magnitude of the anharmonic correction, are further discussed in Chapter 2 (Fig. (2.6)), for the case of thin-film organic polymers.

## 1.3 Calculation of the potential auto-correlation function

Classical mechanical linear-response theory has been shown to be valid for cantilever measurements in parallel motion over thin-film organic polymers [68, 69]. The validity of the linear response assumption will be tested for a thin-film organic polymer, an organic transistor, and for doped Si in subsequent Chapters. The frequency jitter must have a quadratic dependence on $V_{\mathrm{ts}}$ if the linear-response assumption is valid. Under the linear-response assumption, the equilibrium potential autocorrelation is calculated by introducing a fictitious time-varying charge $q(t)$, at position $(\mathbf{r}_1, z_1)$ above the sample surface. The interaction of the fictitious charge and the sample generates a reaction potential above the sample at location $(\mathbf{r}_2, z_2)$ denoted by $\phi(\mathbf{r}_2, z_2, t)$. The classical perturbation Hamiltonian of this interaction at the location of the charge $q(t)$ at $(\mathbf{r}_1, z_1)$ is given by

$$H_{\mathrm{int}} = q(\mathbf{r}_1, z_1; t)\ \phi(\mathbf{r}_1, z_1; t). \tag{1.35}$$

Classical mechanical linear response theory relates the reaction potential to the equilibrium potential auto-correlation function via the response function $\hat{\Phi}_q(\omega)$[46, 67, 69]

$$\hat{\phi}(\mathbf{r}_2, z_2, f) = \hat{q}(\mathbf{r}_1, z_1, f)\hat{\Phi}_q(f), \tag{1.36}$$

$$\hat{\Phi}_q(f) \equiv [2\pi i f C_{\delta\phi\,\delta\phi}(\mathbf{r}_1, z_1, \mathbf{r}_2, z_2, f) - C_{\delta\phi\,\delta\phi}(0)]/(k_B T), \tag{1.37}$$

where

$$\hat{\Phi}_q(f) \equiv \int_0^\infty dt\, e^{-i2\pi f t}\Phi_q(t) \tag{1.38}$$

From Eqs. (1.36) and (1.37), the equlibrium potential auto-correlation can be written in terms of a reaction potential from the sample as

$$C_{\delta\phi\,\delta\phi}(\mathbf{r}_1, z_1, \mathbf{r}_2, z_2; f) \quad = \quad \frac{k_B T}{2\pi f}\mathrm{Im}\left(\frac{\hat{\phi}(\mathbf{r}_2, z_2, f)}{\hat{q}(\mathbf{r}_1, z_1, f)}\right). \tag{1.39}$$

The macroscopic potential $\phi(t)$ obeys the conventional form of the Maxwell's equations and is related to the microscopic fluctuating potential $\varphi$ in Eq. (1.15) by $\phi = \langle \varphi(z,t) \rangle$. The reaction potential $\phi(\mathbf{r}_2, z_2, f)$, is determined from macrosopic electrodynamics by solving the boundary-value problem of a charge at a distance $d$ above the sample. The solution of this boundary-value problem, and the frequency jitter and noncontact friction calculations are shown for organic thin-film polymers, organic transistors and doped Si samples in Chapters 2, 3 and 4, respectively.

# CHAPTER 2
## MOLECULAR MOTIONS PROBED BY ELECTRIC FORCE MICROSCOPY

Fluctuations in organic thin-film polymers have been measured using Electric Force Microscopy by Professor John Marohn and his group [20, 21, 30, 31, 67, 68, 69]. This chapter analyzes the measurements [20, 21] of the dielectric fluctuations over poly(vinyl acetate) (PVAc) for frequencies around 1Hz at room temperature. A commercial AFM cantilever was employed to measure the power spectrum of cantilever frequency fluctuations as a function of frequency, tip-sample distance, and tip voltage. Analogous to the previous experimental and theoretical efforts on frequency noise measurements on thin-film organic polymers for the parallel motion of the cantilever tip on the sample surface [67, 68, 69], here the theory for the perpendicular motion of the cantilever tip is developed, and a quantitative comparison to the frequency noise measurements on PVAc is provided. The theory developed quantitatively explains the dependence of the power spectrum of cantilever frequency fluctuations on frequency, tip-sample distance and tip-voltage. The inputs to theory for these calculations of cantilever frequency noise are the sample thickness, sample dielectric spectrum, tip radius, tip-sample distance, tip voltage, cantilever resonance frequency, and force constant. The cantilever frequency fluctuations are shown to originate from the equilibrium fluctuations of the electrostatic potential (and its derivatives at the cantilever tip) arising from thermal dielectric fluctuations in the sample. This work thus provides a basis for dielectric-loss imaging of organic thin-film polymers. It also provides a theoretical basis for interpreting perpendicular-geometry cantilever measurements on new samples [21].

## 2.1 Experiment

The EFM experiments are performed on a polyvinylacetate (PVAc) sample [21]. A PVAc layer of thickness $h = 63$ nm was spin cast onto a gold-covered silicon substrate. The scanning probe measurements on PVAc were performed at a pressure of $0.5 \times 10^{-6}$ mbar and at a temperature of 20.7 °C. The cantilever was driven by a custom bulit positive feedback circuit at its resonance frequency of $f_c \approx 46.0$ kHz. The position of the cantilever was extracted, and fed to a software frequency demodulator to convert the cantilever position into a frequency vs. time signal. The Fourier transform of autocorrelation function of frequency fluctuations was used to obtain the frequency noise spectra. A ring-down measurement was performed to determine the cantilever's quality factor, $Q \approx 2500$. The force constant $k_{\mathrm{c}} = 0.85$ N/m was determined from the equipartition principle $k_{\mathrm{c}} = k_B T / \left\langle x_{\mathrm{th}}^2 \right\rangle$, where the root-mean-squared amplitude $\left\langle x_{\mathrm{th}}^2 \right\rangle$ of the thermomechanical fluctuations was obtained from observations of cantilever position fluctuations. Experiments were carried out as detailed in Sec. experimental methods of Ref. [21] and Chapter 3 of Nikolas Hoepker's thesis [20]. Further details of experiment may be found in Refs. [20, 21, 30, 31, 67, 68, 69].

## 2.2 Theoretical modelling

With the cantilever perpendicular motion modelled as in Secs. 1.1.2, 1.2.2, and 1.3, it is only necessary to calculate the potential auto-correlation at the cantilever tip in order to calculate the cantilever frequency noise for perpendicular motion using Eq. (1.30). As laid out in Sec. 1.3, the equilbrium potential autocorrelation is related to the reaction potential $\phi(\mathbf{r}_2, z_2, f)$ by Eq. (1.39), in the lin-

ear response approximation. In this section, we calculate the reaction potential at $(\mathbf{r}_2, z_2)$ by solving the boundary-value problem of a charge $q(\mathbf{r}_1, z_1, t)$ located at $(\mathbf{r}_1, z_1)$ above an organic thin-film polymer of thickness $h$, backed by a conductor. Here, $z = 0$ is the plane of the vacuum-sample interface, $z > 0$ is vacuum where the fictitious charge is located at a distance $z_1$ above the interface, and $z < 0$ corresponds to the sample. We model the PVAc sample used in measurements as a dielectric layer of thickness $h$ over a conductor. Figure. (2.1) shows the experimental sketch of cantilever and the PVAc sample, and the inset in the experimental sketch shows the scanning electron microscope image of the cantilever tip taken by Nikolas Hoepker [20, 21]. The tip-radius is read as 40 nm from the inset of the Figure. (2.1). Without loss of generality for a perpendic-

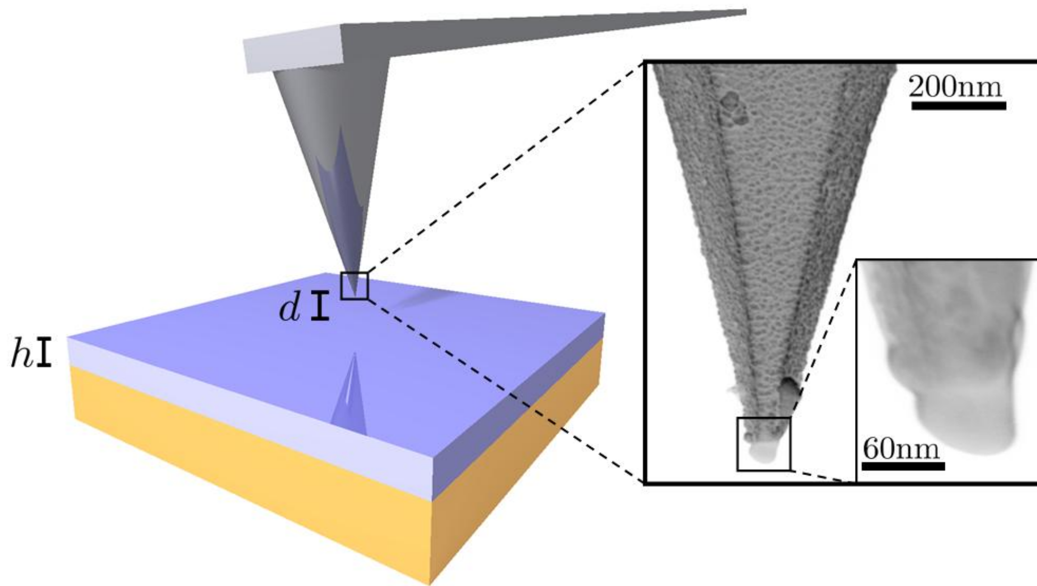


Figure 2.1: Electric force microscopy measurements on a thin layer of organic film of thickness $h$ over a conductor. The cantilever tip is positioned at a distance $d$ above the sample surface. The inset shows scanning electron microscope (SEM) image of the cantilever tip. The tip-radius is read as 40 nm from this image. Figure reproduced from Ref.[21], with permission.

ular motion of the cantilever, the motion is taken along $z$-axis, and so we only need to calculate the autocorrelation of potential fluctuations between locations $(\mathbf{r}_1 = \mathbf{0}, z_1) \equiv z_1$ and $(\mathbf{r}_2 = \mathbf{0}, z_2) \equiv z_2$. The Maxwell's equations for a point charge located at $z_1$ in vacuum are

$$\nabla \times \mathbf{E} = -i\omega\mu_0\mathbf{H}, \tag{2.1}$$

$$\nabla \times \mathbf{H} = i\omega\epsilon_0\mathbf{E}, \tag{2.2}$$

$$\nabla \cdot \mathbf{E} = \frac{q(z_1, \omega)}{\epsilon_0}\delta(z - z_1). \tag{2.3}$$

Eqs. (2.1)-(2.3) can be combined to give a second-order equation for the electric fields in vacuum:

$$\nabla^2\mathbf{E} + \frac{\omega^2}{c^2}\mathbf{E} = \frac{q(z_1, \omega)}{\epsilon_0}\nabla(\delta(z - z_1)), \tag{2.4}$$

where $c \equiv 1/\sqrt{\mu_0\epsilon_0}$ is the speed of light. The spatial Fourier transform in the plane of the interface involves an intergral over $\mathbf{r} = (x, y)$ as follows

$$\hat{\mathbf{E}}(\mathbf{k}, z, \omega) = \int d\mathbf{r}\, e^{i\mathbf{k}\cdot\mathbf{r}}\, \mathbf{E}(\mathbf{r}, z, \omega). \tag{2.5}$$

The second-order differential equation for the electric field vector in Eq. (2.4) is written in terms of its components, in Fourier space $(\mathbf{k}, z)$ as

$$\frac{\partial^2 \hat{E}_x}{\partial z^2} - \tilde{k}^2\hat{E}_x = -ik\frac{q(z_1, \omega)}{\epsilon_0}\delta(z - z_1), \tag{2.6}$$

$$\frac{\partial^2 \hat{E}_z}{\partial z^2} - \tilde{k}^2\hat{E}_z = \frac{q(z_1, \omega)}{\epsilon_0}\frac{\partial}{\partial z}\delta(z - z_1), \tag{2.7}$$

$$\tilde{k} \equiv \sqrt{k^2 - (\omega/c)^2}. \tag{2.8}$$

The solution to these equations is

$$\hat{E}_x = \frac{i\tilde{k}}{k}\left(\frac{q(z_1, \omega)}{2\epsilon_0}\right)e^{-\tilde{k}|z-z_1|} + \frac{i\tilde{k}}{k}A_{\mathrm{rxn}}e^{-\tilde{k}z}, \tag{2.9}$$

$$\hat{E}_z = \frac{q(z_1, \omega)}{2\epsilon_0}e^{-\tilde{k}|z-z_1|}(2\Theta(z - z_1) - 1) + A_{\mathrm{rxn}}e^{-\tilde{k}z}, \tag{2.10}$$

with $k$ aligned along $x$-axis. The magnetic field in vacuum is calculated from $\nabla \times \mathbf{E} = -i\omega\mu_0\mathbf{H}$ with $\hat{E}_x$ and $\hat{E}_z$ given by Eqs. (2.9) and (2.10), respectively. The magnetic field in vacuum may be written in a compact form as,

$$\hat{H}_y = -\frac{\omega}{\mu_0 k c^2}\hat{E}_z. \tag{2.11}$$

The absence of charge carriers in the dielectric gives $\nabla \cdot \mathbf{E} = 0$ as an additional Maxwell equation inside the dielectric. These equations can be solved in a similar fashion to obtain the following general solution for the electric fields in the dielectric in $0 < z < -h$,

$$\hat{E}_x = C_1 e^{\tilde{\eta}z} + C_2 e^{-\tilde{\eta}z}, \tag{2.12}$$

$$\hat{E}_z = \frac{ik}{\tilde{\eta}}(C1 e^{\tilde{\eta}z} - C_2 e^{-\tilde{\eta}z}), \tag{2.13}$$

$$\hat{H}_y = \frac{-i\omega\epsilon_{rel}(\omega)}{\tilde{\eta}\mu_0 c^2}(C_1 e^{\tilde{\eta}z} - C_2 e^{-\tilde{\eta}z}), \tag{2.14}$$

$$\tilde{\eta} = \sqrt{k^2 - (\omega/c)^2\epsilon_{rel}(\omega)}. \tag{2.15}$$

These field equations, Eqs. (2.9)-(2.11) and (2.12)-(2.14), are solved using the continuity conditions for $E_x$, $\epsilon(\omega)E_z$ and $H_y$ at dielectric-conductor interface located at $z = -h$ and at vacuum-dielectric interface located at $z = 0$. The following 3 conditions are obtained when these continuity conditions are written at both the interfaces,

$$C_1 e^{-\tilde{\eta}h} + C_2 e^{\tilde{\eta}h} = 0, \tag{2.16}$$

$$\frac{ik\epsilon_{rel}(\omega)}{\tilde{\eta}}(C_1 - C_2) = -\frac{q(z_1,\omega)}{2\epsilon_0}e^{-\tilde{k}z_1} + A_{\mathrm{rxn}}, \tag{2.17}$$

$$C_1 + C_2 = \frac{i\tilde{k}}{k}\left(\frac{q(z_1,\omega)}{2\epsilon_0}\right)e^{-\tilde{k}z_1} + \frac{i\tilde{k}}{k}A_{\mathrm{rxn}}. \tag{2.18}$$

Using these conditions, the reaction field amplitude $A_{\mathrm{rxn}}$ is obtained.

$$A_{\mathrm{rxn}} = -\frac{q(z_1,\omega)}{2\epsilon_0}e^{-\tilde{k}z_1}\left(\frac{\epsilon_{\mathrm{rel}}(\omega) - \theta_d}{\epsilon_{\mathrm{rel}}(\omega) + \theta_d}\right), \tag{2.19}$$

$$\theta_d \equiv \frac{\tilde{\eta}}{\tilde{k}}\tanh\tilde{\eta}h. \tag{2.20}$$

The sample reaction field at $(\mathbf{k}, z)$ due to a point charge at $z_1$ is $\hat{E}_{\text{z,rxn}}(\mathbf{k}, z, \omega) = A_{\text{rxn}} e^{-\tilde{k}z}$ from Eq. (2.10). The reaction potential is related to this reaction field by $E_{\text{z,rxn}} = -\partial\phi(z, \omega)/\partial z$. Thus, the reaction potential in $\mathbf{k}$-space is $\phi(z, \omega) = E_{\text{z,rxn}}/\tilde{k}$. The reaction field at $z = z_2$ in $\mathbf{r}$-space for $\mathbf{r} \equiv (x, y) = (0, 0)$ is obtained by taking the inverse of the spatial Fourier transform as

$$\phi(z_2, \omega) = -\frac{q(z_1, \omega)}{4\pi\epsilon_0} \int_0^\infty dk \frac{k}{\tilde{k}} e^{-\tilde{k}(z_1+z_2)} \left( \frac{\epsilon_{\text{rel}}(\omega) - \theta_d}{\epsilon_{\text{rel}}(\omega) + \theta_d} \right). \tag{2.21}$$

The reaction potential in Eq. (2.21) is inserted into Eq. (1.39) to obtain the potential autocorrelation function in the linear response assumption for $\mathbf{r}_1 = \mathbf{0}$ and $\mathbf{r}_2 = \mathbf{0}$. Further, the quasistatic limit $c \to \infty$ is applied to obtain an expression for the potential autocorrelation that is valid for the low frequencies probed by the measurement.

$$C_{\delta\phi\,\delta\phi}(\mathbf{r}_1 = \mathbf{0}, z_1, \mathbf{r}_2 = \mathbf{0}, z_2; f) = -\frac{k_B T}{4\pi\epsilon_0 \omega h} \text{Im} \int_0^\infty \text{dy} e^{-\text{y}(\text{z}_1+\text{z}_2)/\text{h}} \left( \frac{\epsilon_{\text{rel}}(\omega) - \theta_{\text{d}}}{\epsilon_{\text{rel}}(\omega) + \theta_{\text{d}}} \right),$$
$$\theta_{\text{d}} = \tanh y. \tag{2.22}$$

With Eq. (2.22) as the potential autocorrelation in Eq. (1.27), the rest of the correlation functions in Eq. (1.30) are calculated by taking derivatives as explained in Sec. 1.2.2. These correlation functions are substituted into Eq. (1.30) to obtain the power spectrum of cantilever resonance frequency fluctuations at the equilibirum position of cantilever $(0, 0, d)$ over thin-film organic polymers:

$$P_{\delta f_c}(f) = \left( \frac{f_c V_{\text{ts}}}{k_c} \right)^2 \frac{k_B T \epsilon''_{rel}(\omega)}{2\pi\epsilon_0 \omega h} \Big[ (c^{(2)}(d))^2 J_0(d, d, \omega) + 4c^{(1)}(d)c^{(2)}(d) J_1(d, d, \omega)$$
$$+2c^{(0)}(d)c^{(2)}(d) J_2(d, d, \omega) + 4\left(c^{(1)}(d)\right)^2 J_2(d, d, \omega) - 4c(d)c^{(1)}(d) J_3(d, d, \omega)$$
$$+c^{(2)}(d) J_4(d, d, \omega) \Big], \tag{2.23}$$

where

$$J_n(z_1, z_2, \omega) \equiv \int_0^\infty dy (-y/h)^n e^{-y(z_1+z_2)/h} \left( \frac{\tanh y}{|\epsilon_{\text{rel}}(\omega) + \tanh y|^2} \right). \tag{2.24}$$

## 2.3 Results and discussion

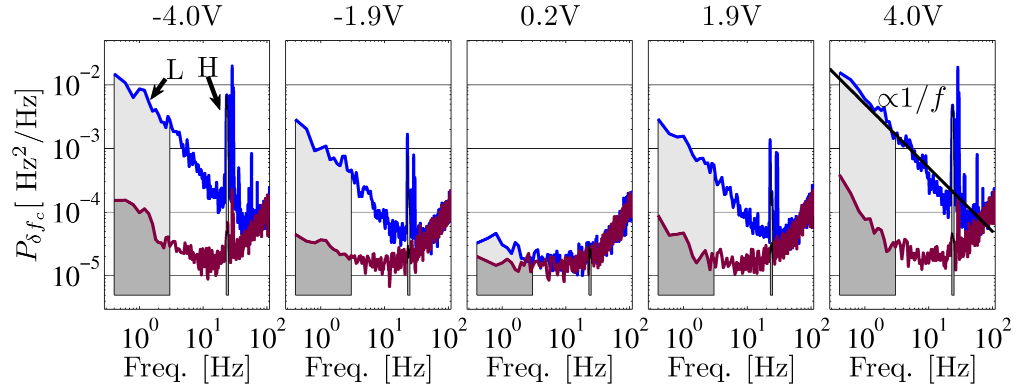


Figure 2.2: Spectral density of cantilever frequency fluctuations at heights $d$ = 90 nm (blue, upper line) and 240 nm (red, lower line), for tip voltages ranging from −4 V to +4 V, measured on PVAc. A 1/f guideline is shown. Figure reproduced from Ref.[21], with permission.

Figure (2.2) shows measured power spectra of cantilever resonance frequency fluctuations on PVAc for two tip-sample distances, $d$ = 90 nm and $d$ = 240 nm, and a range of voltages from −4 V to 4 V. Two grey regions are marked as L and H. Region L is a low-frequency region where the frequency noise spectra are $\propto 1/f$ while region H is a high frequency region around 25 Hz where there are spikes in the spectrum. The region beyond the spikes is observed to increase $\propto f^2$. This $f^2$-dependence of the power spectrum is independent of tip voltage and tip-sample distance, and so is attributed to the noise in the interferometer displacement sensor [1, 21, 39, 69]. This instrumentation noise does not interfere with measurements below 10 Hz, the focus of the analysis presented here. On the other hand, the $1/f$ region and the spikes around 25 Hz of the spectra depend on tip voltage and tip-sample distance. More noise (blue line) is observed when the tip is closer to the sample, and so these features are attributed to electrostatic tip-sample interactions. These low-

frequency features are further analyzed by studying the voltage dependence of the power spectrum integrated over a well defined frequency range. This inte-

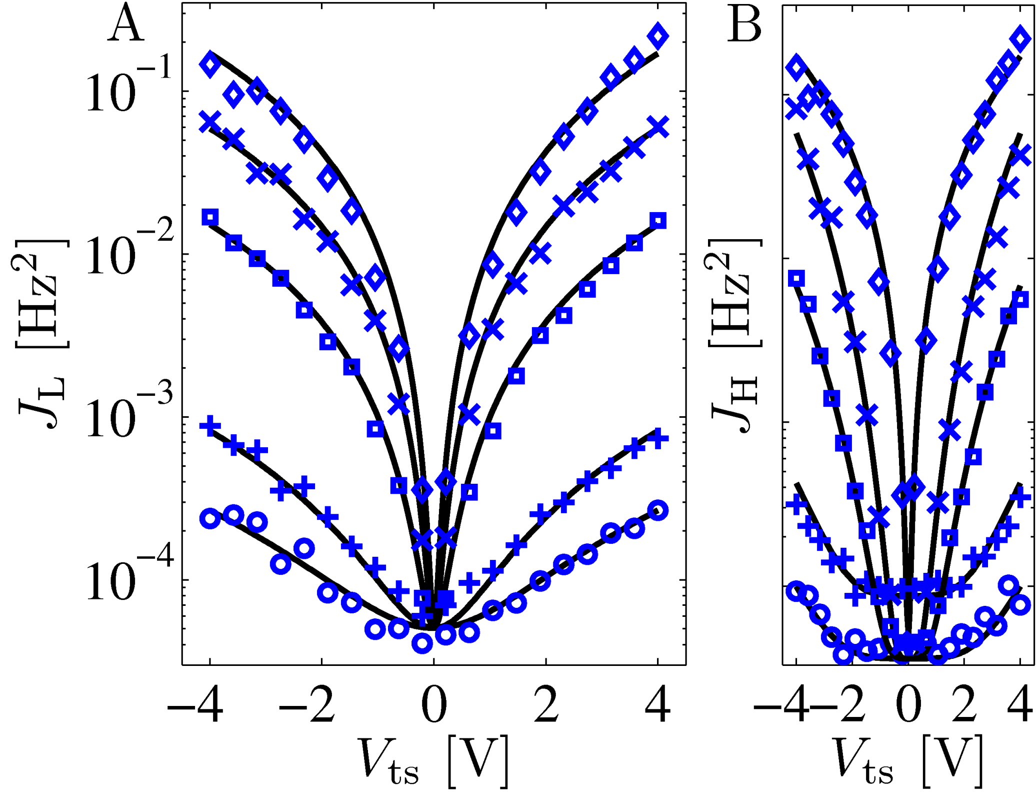


Figure 2.3: Cantilever frequency jitter as a function of tip voltage at various tip-sample separations (50 nm - ◇, 62 nm - ×, 90 nm - □, 180 nm - +, 240 nm - ∘). $J_L$ in A is integration from 0.4 to 3 Hz of L-region in Fig. (2.2) and $J_H$ in B is integration from 23 to 25 Hz of H-region in Fig. (2.2). Solid lines are fits to experimentally measured data: $J_L$ is $\propto V_{\mathrm{ts}}^2$ and $J_H$ is $\propto V_{\mathrm{ts}}^4$. Figure reproduced from Ref.[21], with permission.

grated power spectrum as defined in Eq. (1.28), called frequency jitter, is shown in Fig. (2.3) at various tip-sample distances. In Fig. (2.3A), the power spectrum is integrated from 0.4 to 3 Hz over the L-region, and shows $J_{\mathrm{L}} \propto V_{\mathrm{ts}}^2$. In Figure. (2.3B), the power spectrum is integrated from 23 to 25 Hz over the H-region in Fig. (2.2), and shows $J_{\mathrm{H}} \propto V_{\mathrm{ts}}^4$. Hoepker [20, 21] measured the stage vibration spectrum using laser interferometry and showed that the jitter in Fig. (2.3B) is

a consequence of external mechanical vibrations [20, 21]. Turning our attention to low frequency noise originating in tip-sample electrostatic interactions [23, 50, 51, 64, 65, 68, 69], the L-region in Fig. (2.2), the frequency spectra shows a $1/f$-dependence as predicted by Eq. (2.23) of the model when the dielectric function $\epsilon_{\rm rel}(\omega) = \epsilon'_{\rm rel}(\omega) - i\epsilon''_{\rm rel}(\omega)$ is independent of frequency. The independence of $\epsilon_{\rm rel}(\omega)$ on frequency is seen from the dielectric measurements at low frequencies in Fig. (2.5). The quadratic dependence in tip voltage of frequency jitter $J_L$ in Fig. (2.3A) is also obtained from our model by the integrating power spectrum in Eq. (2.23) from 0.4 to 3 Hz. This finding validates our use of linear response assumption in Sec. 1.3 in the calculation of the equilibrium correlation functions in Eq. (1.30). Any non-linear behaviour of the frequency jitter would have given higher orders of dependence on voltage. With the expression for the power spectrum as in Eq. (2.23), a model for the tip-sample capacitance $c(z)$ as a function of tip-sample height $z$ is needed, in order to quantitatively fit our theory to measured data. Fig. (2.4) shows the measured capacitance second-derivative ($\circ$) inferred from Eq. (1.17) for known values of $f_c$ and $k_c$, and the measured static shift in resonance frequency $\Delta f_c$. The figure also shows a calculated capacitance second-derivative from sphere and cone models versus tip-sample distance. Following Cherniavskaya et al.[10], the irregular pyramid of cantilever tip is modelled as cone with a sphere at its tip. The sphere model for tip-sample capacitance consists of a sphere charge of radius $R$ representing the probe tip with centre located at a height $d + R$ above the vacuum-sample interface. The sample is represented by a dielectric layer with relative permittivity $\epsilon_r$ and thickness $h$ over a conductor. The capacitance from this model was used to quantitatively fit the data from parallel motion measurements on organic thin-

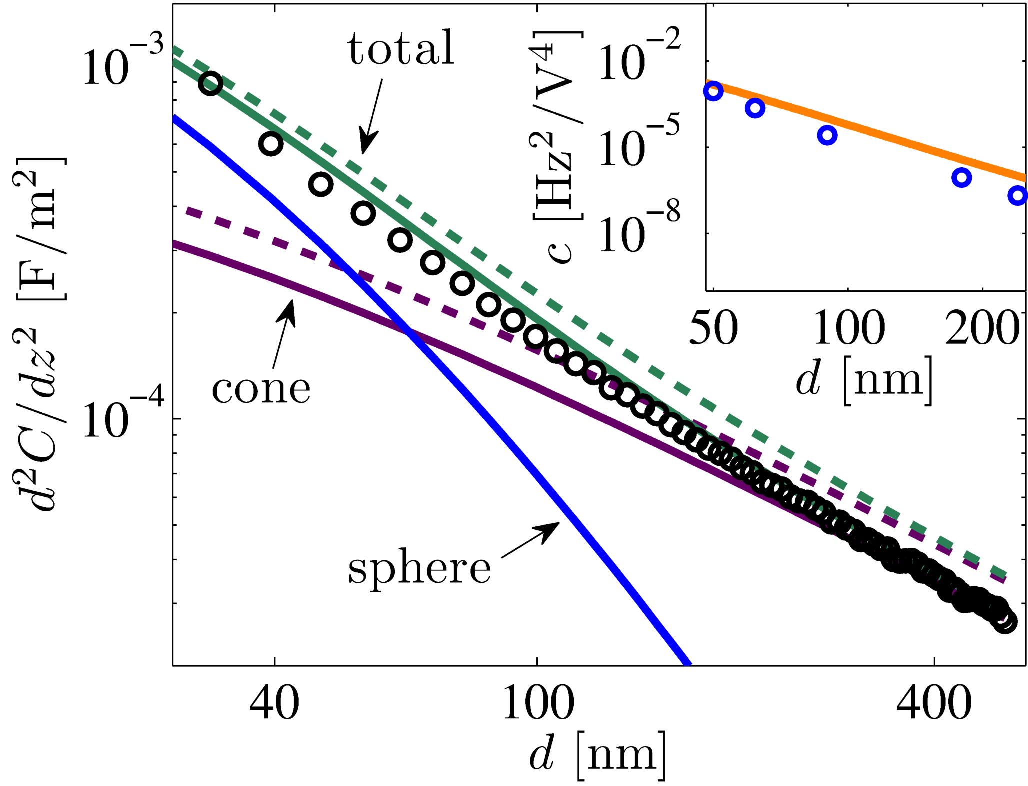


Figure 2.4: Measured capacitance second derivative, $C_2$, versus tip height (∘). The solid lines are the predicted contributions from a 40 nm sphere, a cone with a half angle of 16 deg, and both sphere plus cone. The dashed lines show predictions for a cone angle of 20 deg. Inset: Fit coefficient $c$ in $J_{\mathrm{H}} = c\, V_{\mathrm{ts}}^4$ from Fig. (2.3B) (circles) and prediction (line) from vibration noise determined by interferometry. Figure reproduced from Ref.[21], with permission.

film polymers in the earlier work [67, 68, 69], with good agreement.

$$
\begin{aligned}
c(z) &= 4\pi\epsilon_0 R \sum_{n=1}^{\infty} \left( \frac{\sinh \alpha}{\sinh n\alpha} \right), \\
\alpha &= \cosh^{-1}\left[ 1 + \frac{z}{R} + \frac{h}{\epsilon_r R} \right].
\end{aligned}
\tag{2.25}
$$

The formula for the second derivative of capacitance in the cone model is obtained using a uniform line charge approximation [10]. For a small cone half angle $\theta$ and a tip-sample height much less than the length of the line charge (L),

$z << L$, and the second derivative of the cone capacitance is [10]

$$
\begin{aligned}
c^{(2)}(z) &= \frac{8\pi\epsilon_0}{\beta^2 z}, \\
\beta &= \ln\left(\frac{1+\cos\theta}{1-\cos\theta}\right). \qquad (2.26)
\end{aligned}
$$

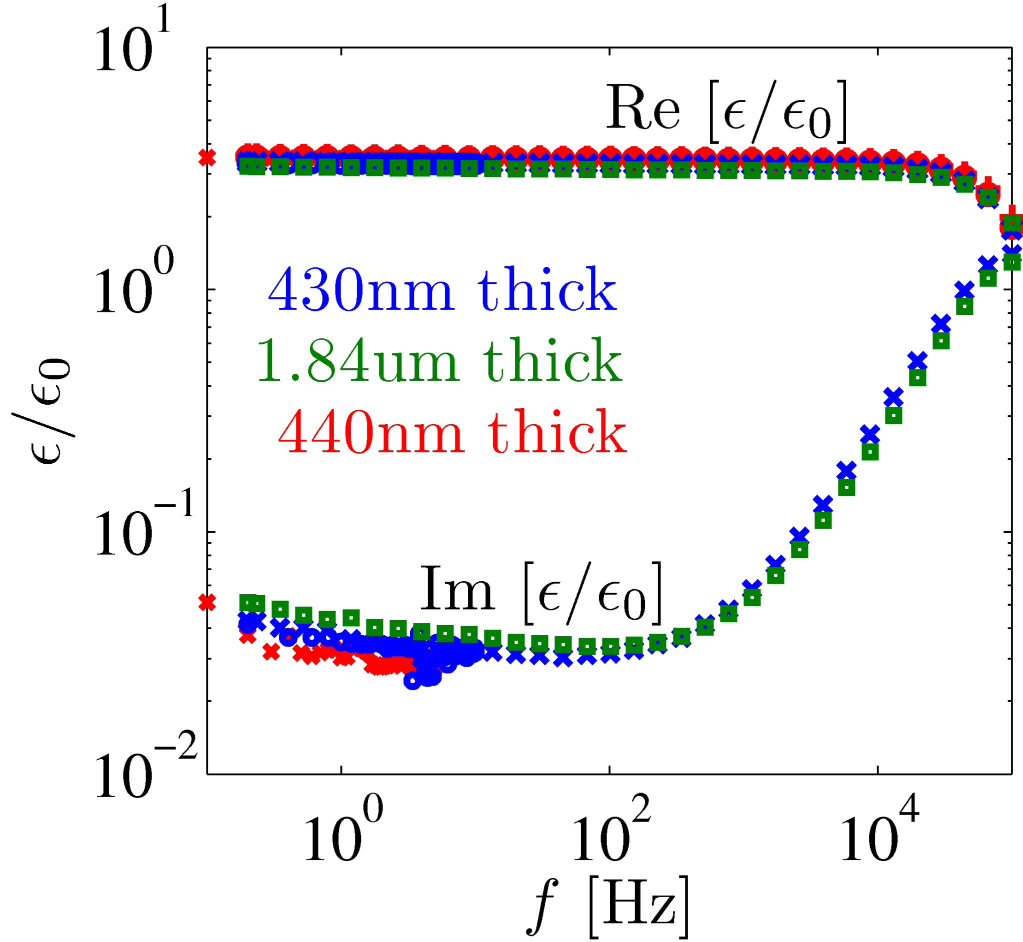


Figure 2.5: Measured dielectric spectrum of PVAc. Figure reproduced from Ref.[21], with permission.

In Fig. (2.4), the second derivative of capacitance from sphere model in Eq. (2.25) (with $R = 40$ nm (from Fig. (2.1)) and $\epsilon_r$ from Fig. (2.5)) better predicts the tip-sample capacitance at small tip-sample distances, while the cone model (Eq. (2.26)) works better at large tip-sample distances. A cone with a half angle

of $\theta = 16$ deg was used in the calculation of the solid lines (green, magenta), while the dashed lines (green, magenta) use a cone angle of 20 deg. The sum of the sphere and cone contributions ($\theta = 16$ deg), indicated as total in Fig. (2.4), is in close agreement with the second derivative of capacitance inferred from measurements of static shift in resonance frequency [20]. This agreement validates the use of the cone-sphere model in calculations for further quantitative comparison to frequency jitter. Fig. (2.5) is the measured dielectric spectrum of PVAc, and it is seen that $\epsilon''(f)$ is a constant in the frequency range 0.4 to 3 Hz. This measured dielectric spectrum is used in the calculations of frequency jitter. Eq. (2.23) predicts a $1/f$ dependence for a constant $\epsilon''(f)$, and thus the $1/f$ dependence observed in the low frequency region of frequency spectra measurements in Fig. (2.2), is in agreement with the model. The tip-sample distance dependence and the magnitude of the noise are studied by calculating the frequency jitter from Eqs. (1.28) and (2.23), with $f_{\mathrm{min}} = 0.4$ Hz and $f_{\mathrm{max}} = 3$ Hz. In spite of the better fit to the second derivative of capacitance seen with the cone plus sphere model of capacitance in Fig. (2.4), only the sphere model is used in the jitter calculations. This is justified because the cone contribution to jitter was shown to be negligible [20, 21] compared to the sphere contribution to jitter. Hence, Figs. (2.6) and (2.7) only show the sphere contribution to jitter.

Fig. (2.6) shows the comparison of experimentally obtained jitter values ($\circ$) for different tip-sample distances. The figure also shows the jitter calculated from Eqs. (1.28) and (2.23) plus a thermal noise floor of thermomechanical position fluctuations (solid lines) for two effective tip-sample distances –$d$ (top) and $d + R$ (bottom)– versus the tip-sample height. The spectrum of frequency noise due to thermomechanical position fluctuations is independent of frequency and

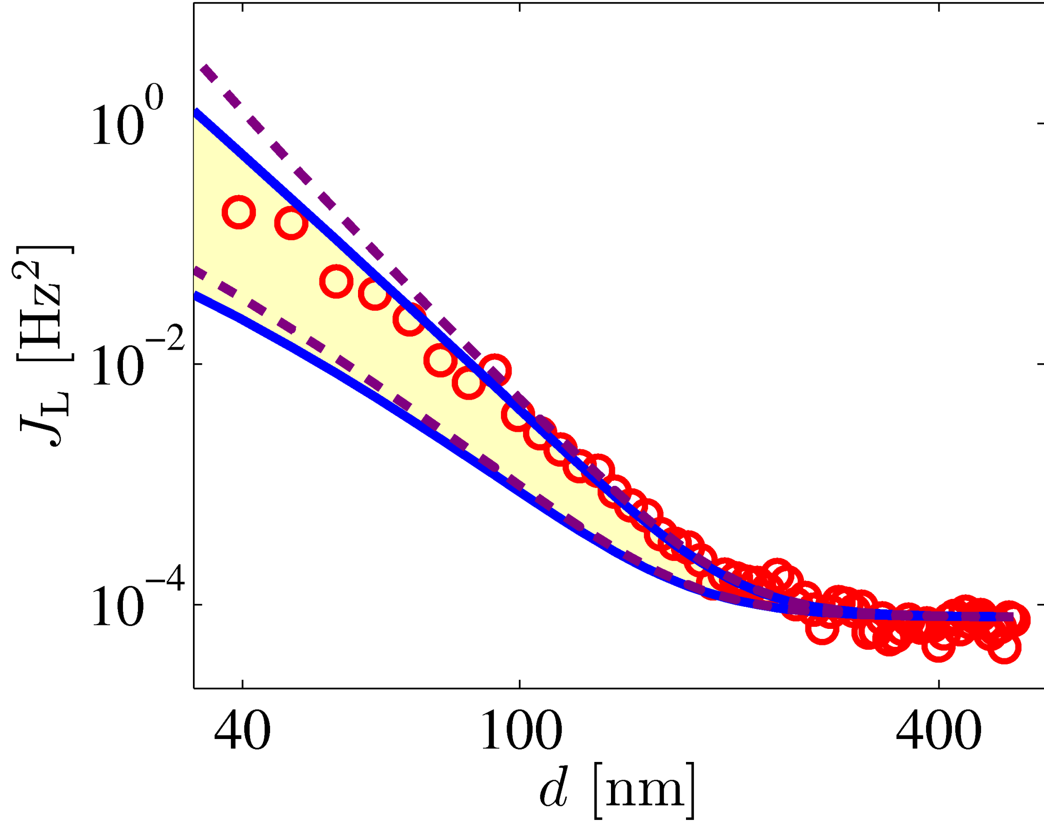


Figure 2.6: Jitter measured (∘) on PVAc versus tip-sample height. Solid lines are jitter calculated from the sphere model of capacitance by integrating Eq. (2.23) from 0.4 to 3 Hz. The solid line (bottom) is calculated for an effective tip-sample height of $d + R$, with the total charge located at the centre of the sphere. The solid line (top) is for an effective tip-sample height of $d$ when the charge is located at the bottom of the sphere. The jitter is predicted to lie within the shaded grey region, in excellent agreement with experiment. The dashed lines add contributions from anharmonic tip-sample interactions to the solid lines. Figure reproduced from Ref.[21], with permission.

given by[1, 21, 39, 68, 69]

$$P_{\delta f_c}^{\text{therm}}(f) = \frac{k_B T f_c}{2\pi x_{\text{rms}}^2 k_c Q}, \tag{2.27}$$

where $x_{\text{rms}} = 32$ nm is the root-mean-squared cantilever amplitude in the experiment and $Q$ is the cantilever quality factor determined experimentally and given in Sec. 2.1 as 2500 [21, 68]. A shaded grey area is shown between the lower and upper bound (solid lines) from the theoretical calculation to mark the region in which the experimental data may lie. The upper and lower bounds for jitter are obatined by using two different effective heights for the equilibrium position of the charge. The jitter calculation needs merging of two different models: One is the point charge located above the sample to calculate potential autocorrelation function in Sec. 1.3, and the other is the model for tip-sample capacitance in Eq. (2.25) where the spherical tip of radius $R$ is located at a height $z$ above the sample. The lower bound for jitter is obtained by having the point charge in the calculation of potential autocorrelation at $d+R$, at the centre of the spherical charge of radius $R$ in the capacitance formula. The upper bound of jitter is obtained when the point charge is located at a height $d$ above the sample, which is the bottom of the spherical tip of radius $R$. Excellent agreement is observed between measured jitter and jitter calculation with an effective tip-sample height of $d$, with the charge is located at the bottom of the sphere. The dashed lines in Fig. (2.6) are the anharmonic corrections from the quartic term in Eq. (1.34) for the effective tip-sample heights $d$ and $d + R$. It is seen from the figure that anharmonicity only enhances jitter at the smallest values of tip-sample heights, and overall does not contribute much to total jitter. Further, from Eq. (1.34) the anharmonic correction from the quartic term is $\propto z_{\text{rms}}^2 \equiv A^2/2$ where $A$ is the amplitude. Hoepker [20] studied the frequency jitter dependence on amplitude, and recorded the same order of dependence as predicted by Eq. (1.34) for jitter.

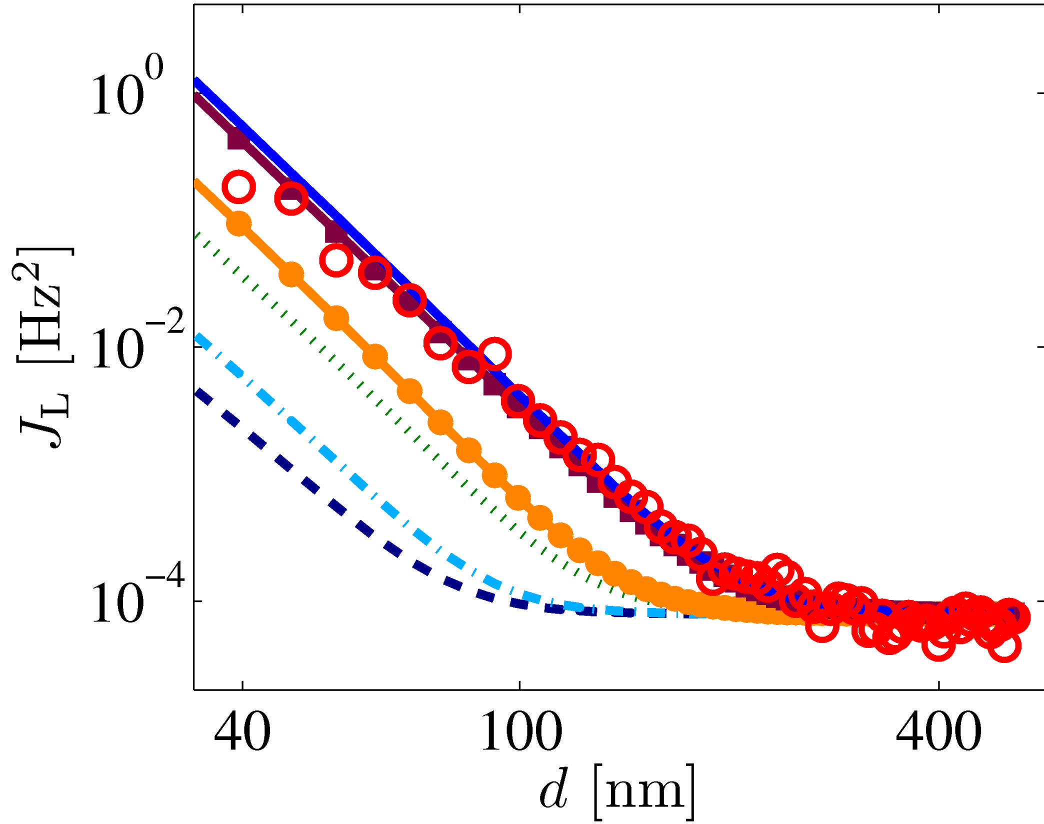


Figure 2.7: Total jitter calculated (topmost solid line) with an effective tip-sample height of $d$ and jitter data (∘) versus tip-sample height, drawn from Fig. (2.6). The rest of the lines are contributions to the total jitter (top most solid line) from individual terms in the power spectrum Eq. (2.23) integrated from 0.4 to 3 Hz. In increasing order of magnitude of contribution, these are: $J_0$ (dashed line), arising from the autocorrelation of voltage fluctuations, $J_1$ (dot-dashed line), from a cross-correlation of electric field and voltage fluctuations, $J_2$ (dotted line), arising from both the autocorrelation in electric field and cross-correlation of electric field gradient and voltage, $J_3$ (solid line with ∘), arising from a crosscorrelation of electric field and electric field gradient, and $J_4$ (solid line with □), arising from autocorrelation of field gradient fluctuations. Figure reproduced from Ref.[21], with permission.

Fig. (2.7) shows the various contributions to total jitter from different terms in the power spectrum. Terms plotted include auto- and cross-correlation terms of fluctuations in the potential, the $z$ component of the electric field and z-gradient of electric field in $z$-direction, integrated from 0.4 to 3 Hz. The total jitter (solid line) is practically the same as the jitter calculated in Fig. (2.6) for an effective tip-sample height of $d$ and measured jitter is shown as $\circ$. The jitter contributions obtained when the terms in Eq. (2.23) are integrated separately from 0.4 to 3 Hz are also indicated in the Figure. The dominant term in these contributions arising from $J_4$, which is the autocorrelation term of electric field gradient fluctuations, while the least contributing term is $J_0$ corresponding to the autocorrelation of potential fluctuations. Unlike Israeloff and co-workers [12, 13, 50, 51, 64, 65], who interpreted their measurements of cantilever frequency fluctuations over polymer films to be resulting solely from voltage fluctuations at tip driven by polarization fluctuations in the sample, our analysis shows that the electric field gradient fluctuations and other contributions (Fig. (2.7)) at the tip need to be included in the calculation of total jitter. We find that their magnitude is greater than the jitter contribution from voltage fluctuations.

## 2.4 Summary

The frequency noise measured by EFM on the surface of a thin polymer film is shown to be arise from the dielectric fluctuations of the polymer. The assumption of linear response is validated by the observed quadratic voltage dependence of the integrated frequency noise. Solving the boundary-value problem to calculate the reaction potential from the sample due to the introduction of a fictitious charge connects the equilibrium correlation functions in the linear

response limit to the microscopic dielectric fluctuations of the polymer. Inputting the measured dielectric spectrum and the physical parameters of the experimental set up into the theory reproduces the observed dependencies on frequency, voltage and tip-sample separation. It is shown that any external mechanical vibrations can be distinguished from the frequency noise induced by molecular motions unambiguously due to their appearance at slightly high frequencies and their quartic voltage dependence [20, 21]. The theory shows that the measurements around 1 Hz are from the dynamics in the dielectric spectrum of PVAc in the 0.4 to 3 Hz frequency range. This frequency range for PVAc at room temperature is associated with orientational dynamics of polar polymer segments and $\alpha$-relaxation associated with the glass transition [12, 13, 47, 50, 51, 64, 65]. Thus, it is established that the EFM measurements in perpendicular motion are related to the molecular motions of the sample using the theoretical framework presented in this chapter.

CHAPTER 3

# CHARGE CARRIER DYNAMICS AND INTERACTIONS IN ELECTRIC FORCE MICROSCOPY

Electric force microscopy measures surface electrostatic potential maps in electronic devices as a function of temperature, charge density, and applied bias [7, 28, 36, 63]. In this chapter, motivated by the electric force microscopy fluctuation measurements on organic transistors in the Marohn group, a theory for frequency jitter measurements is developed that is applicable to samples in which there are fluctuations from charge carrier dynamics present in addition to dielectric fluctuations. Chapter 2 showed theoretical calculations and experimental measurements for organic polymer thin-films, and established that the frequency noise measured on these films is due to the thermal dielectric fluctuations in the polymer. Here, we use the same linear response theory assumptions as in Chapters 1 and 2 to calculate the experimental observables. A different boundary-value problem is solved to calculate the reaction potential from a sample that has charge carrier dynamics in the organic polymer. Several works have studied the effect of charge carriers in semiconductors on the calculation of the Casimir-Lifshitz force [14, 44, 60]. Similar to these studies, Maxwell's equations coupled to a transport equation for the free charges is used to calculate the cantilever frequency noise in EFM. Current fluctuation behaviour of organic semiconductors has been studied using trapping-detrapping and charge percolation models in the films [8, 9]. It also has been shown recently that inter-carrier interactions in organic field-effect transistors enhance the performance of electronic ratchet circuits [48]. The model shown in this chapter describes the frequency noise generated by a molecular material with mobile charges. A main focus in organic electronics has been to develop atomic-scale models of charge

transport [3, 6, 17, 18, 35, 38, 41, 66]. The input to these models is electron-transfer equations and a description of the energetic disorder in the sample's ensemble of molecules. The models thus developed are used to predict device current versus temperature and electric field. These models generally neglect the long-range inter-carrier Coulomb interactions. In the few cases where long-range inter-carrier interactions have been considered, the effect of inter-carrier interactions was apparent only in a sophisticated electronic ratchet device [48] or in a simpler transistor device but at extremely high charge concentrations [18]. In contrast, the model developed in this chapter is a macroscopic model of charge fluctuations in an organic transistor that accounts for long-range inter-carrier interactions. The inter-carrier Coulomb interactions are predicted to suppress voltage fluctuations (and hence cantilever frequency noise) over the transistor by orders of magnitude, even at very low concentrations. The work presented here thus provides a new approach for calculating and observing the effects of inter-carrier Coulomb interactions in organic semiconductors.

## 3.1 Theoretical modelling

### 3.1.1 Maxwell's equations coupled to charge transport

The cantilever frequency noise spectrum for perpendicular motion is given by Eq. (1.30), and in the linear response assumption, the equilibrium potential autocorrelation function is related to the reaction potential by Eq. (1.39). Similar to the boundary-value problem in Sec 2.1, $z = 0$ is the vacuum-sample interface, $z < 0$ is the sample, and $z > 0$ is vacuum. The cantilever motion is taken

along the $z$-axis, the position of the time-varying charge $q(\mathbf{r}_1, z_1, t)$ is taken as $(\mathbf{r}_1 = \mathbf{0}, z_1) \equiv z_1$, and the reaction potential from the sample $\phi(\mathbf{r}_2, z_2, f)$ in Eq. (1.39) is calculated at $(\mathbf{r}_2 = \mathbf{0}, z_2) \equiv z_2$. The field equations in vacuum are given by Eqs. (2.9)-(2.11). Maxwell's equations in the semiconductor sample are

$$\nabla \times \mathbf{E} = -i\omega\mu_0 \mathbf{H}, \tag{3.1}$$

$$\nabla \times \mathbf{H} = i\omega\epsilon(\omega)\mathbf{E} + \mathbf{J}, \tag{3.2}$$

$$\epsilon(\omega)\nabla \cdot \mathbf{E} = n \equiv e\left(\rho_+ - \rho_-\right), \tag{3.3}$$

where $\epsilon(\omega)$ is the dielectric function of the medium, $n$ is the total charge density of positively and negatively charged carriers in the medium, and $\rho_{+/-}$ is the number density of positive/negative charge carriers. The current in the medium $\mathbf{J}$ is the sum of an Ohmic term and a diffusive term as follows

$$\mathbf{J} = \sigma_0 \mathbf{E} - D\nabla n. \tag{3.4}$$

This current includes Coulomb interactions and carrier density fluctuations in the medium. Two simplifying assumptions are made here. One is the charge carrier density of both positive and negative charge carriers is $\bar{\rho}$, and so total charge carrier density is $2\bar{\rho}$. The other is the use of Einstein relation between diffusion and mobility ($\mu$) $D = \mu k_B T/e$, and the macroscopic conductivity-mobility relation $\sigma_0 = 2e\mu\bar{\rho}$. Assuming for simplicity that both positive and negative carriers have the same diffusion constant, the conductivity $\sigma_0$ and diffusion coefficient $D$ are related by

$$\sigma_0 = \frac{2\bar{\rho}e^2 D}{k_B T}. \tag{3.5}$$

Using Eqs. (3.1)-(3.4), a second-order differential equation for the electric field vector is obtained

$$\nabla^2 \mathbf{E} + \frac{\omega^2 \epsilon_{\text{eff}}(\omega)}{c^2}\mathbf{E} = \nabla(\nabla \cdot E)\left(1 - i\frac{\omega\epsilon_{\text{rel}}(\omega)}{c^2}D\right), \tag{3.6}$$

$$\epsilon_{\text{eff}}(\omega) \equiv \epsilon_{\text{rel}}(\omega) - i(\Omega/\omega), \tag{3.7}$$

$$\Omega \equiv \sigma_0/\epsilon_0. \tag{3.8}$$

Here, $\epsilon_{\text{eff}}(\omega)$ is the effective dielectric function, and $\epsilon_{\text{rel}}(\omega) = \epsilon(\omega)/\epsilon_0$ is the relative dielectric function of the medium. The effective dielectric function for a medium is obtained when the current in a dielectric medium is given by the Ohm's law [24, 44]. The electric field vector in Eq. (3.6) is written in terms of its components $E_x$ and $E_z$ for the transverse ($E_y = 0$) magnetic mode [14, 59] as

$$\frac{\partial^2 \hat{E}_x}{\partial z^2} + \left(\tilde{s}^2 - ik^2\frac{Ds^2}{\omega}\right)\hat{E}_x = -ik\left(1 - \frac{is^2D}{\omega}\right)\frac{\partial \hat{E}_z}{\partial z},$$

$$\frac{iDs^2}{\omega}\frac{\partial^2 \hat{E}_z}{\partial z^2} + \left(\tilde{s}^2 - k^2\right)\hat{E}_z = -ik\left(1 - \frac{is^2D}{\omega}\right)\frac{\partial \hat{E}_x}{\partial z}, \tag{3.9}$$

$$s^2 = \frac{\omega^2\epsilon_{\text{rel}}(\omega)}{c^2}, \quad \tilde{s}^2 = \frac{\omega^2\epsilon_{\text{eff}}(\omega)}{c^2}. \tag{3.10}$$

Equations in (3.9) are second-order coupled differential equations for the electric field components $E_x$ and $E_z$. These equations are decoupled by going to fourth-order differential equations in both the components [14, 59]

$$\left(\frac{\partial^2}{\partial z^2} - \eta_+^2\right)\left(\frac{\partial^2}{\partial z^2} - \eta_-^2\right)\hat{E}_{x,z} = 0, \tag{3.11}$$

$$\eta_+^2 = k^2 + \frac{\kappa^2}{\epsilon_{\text{rel}}(\omega)} + \frac{i\omega}{D}, \tag{3.12}$$

$$\eta_-^2 = k^2 - \tilde{s}^2, \tag{3.13}$$

$$\kappa^2 \equiv \frac{\sigma_0}{D\epsilon_0}. \tag{3.14}$$

The conductivity and diffusion relation in Eq. (3.5) when used in Eq. (3.14) gives the squared inverse Debye screening length in the medium with unit relative dielectric constant $\kappa^2 = 2\bar{\rho}e^2/\epsilon_0 k_B T$. The variable $\Omega$ in Eq. (3.8) is a frequency associated with the time scale of carriers diffusing one Debye screening length in vacuum. The solutions of the electric field components to these fourth order differential equations are of the form

$$\hat{E}_x = A_+e^{\eta_+ z} + A_-e^{\eta_- z}, \tag{3.15}$$

$$\hat{E}_z = \frac{i\eta_+ A_+}{k} e^{\eta_+ z} + \frac{ikA_-}{\eta_-} e^{\eta_- z}, \tag{3.16}$$

$$\hat{H}_y = \frac{-i\omega\tilde{s}}{\mu_0 \eta_-} A_- e^{\eta_- z}, \tag{3.17}$$

where $A_-$ and $A_+$ are two unknown constants. The continuity conditions of $E_x$, $H_y$, and $\epsilon(\omega)E_z$ at the vacuum-sample interface (at $z = 0$) are used to determine the unknown quantities. Solving these three boundary conditions at $z = 0$ using field equations in vacuum (Eqs. (2.9)-(2.11)), and the field equations in semiconductor (Eqs. (3.15)-(3.17)) gives $A_{\text{rxn}}$, the reaction generated from the semi-infinite semiconductor in the presence of a point charge,

$$A_{\text{rxn}} = -\frac{q(z_1, \omega)}{2\epsilon_0} e^{-\tilde{k}d} \left( \frac{\epsilon_{\text{rel}}(\omega) - \theta_s}{\epsilon_{\text{rel}}(\omega) + \theta_s} \right), \tag{3.18}$$

$$\theta_{\text{s}} \equiv \frac{1}{\eta_+ \tilde{k}} \left( k^2 + \left( \frac{\eta_+ \eta_- - k^2}{1 - i\Omega/\omega\epsilon_{\text{rel}}(\omega)} \right) \right). \tag{3.19}$$

This $A_{\text{rxn}}$ has the same form as that for the thin-film organic polymer in Eq. (2.19) with a new $\theta_{\text{s}}$ as in Eq. (3.19). Similar to Eq. (2.21), the reaction potential from the semiconductor is obtained by replacing $\theta_d$ by $\theta_s$ in Eq. (2.21). The sample reaction potential thus obtained is then inserted into Eq. (1.39) to obtain the equilibrium potential auto-correlation function in the linear response assumption. Applying the quasistatic limit $c \to \infty$, gives an expression for the potential autocorrelation that is valid at the low frequencies pertinent to the measurements:

$$C_{\delta\phi\,\delta\phi}(\mathbf{r}_1 = \mathbf{0}, z_1, \mathbf{r}_2 = \mathbf{0}, z_2; f) = -\frac{k_B T}{4\pi\epsilon_0 \omega d} \text{Im} \int_0^\infty \mathrm{dy} \mathrm{e}^{-\mathrm{y}(\mathrm{z}_1+\mathrm{z}_2)/\mathrm{d}} \left( \frac{\epsilon_{\text{rel}}(\omega) - \theta_{\text{s}}}{\epsilon_{\text{rel}}(\omega) + \theta_{\text{s}}} \right),$$

$$\theta_s = \left( \frac{1}{1-\beta} \right) \left( 1 - \beta \left( \frac{y}{\sqrt{y^2 + i\omega(1-\beta)/\Omega_d}} \right) \right), \tag{3.20}$$

$$\beta \equiv \frac{i\Omega}{\omega\epsilon_{\text{rel}}(\omega)}, \tag{3.21}$$

$$\Omega_d \equiv D/d^2. \tag{3.22}$$

The voltage noise in Eq. (3.20) is generated in vacuum above the sample when interacting charge carriers and dielectric fluctuations are (nonlinearly) coupled

in a semiconductor sample. This expression involves the conductivity $\sigma_0$, the carrier diffusion $D$, and the dielectric spectrum $\epsilon_{\mathrm{rel}}(\omega)$ of the sample as inputs. Although deviations from the Einstein relation $D = \mu k_B T/e$ is observed in organic semiconductors [63], we nevertheless employ the Einstein relation here as a simplifying assumption for our calculations. The calculation of conductivity $\sigma_0$, diffusion constant $D$ and dielectric function $\epsilon_{\mathrm{rel}}(\omega)$ from microscopic properties is outside the scope of this work.

The autocorrelation of potential fluctuations in Eq. (1.39) can be shown to be related to the Casimir-Polder free energy of interaction between an atom and body calculated in Ref.[44]. The interaction free energy $F(d)$ of an atom with a static polarizability $\alpha$ located in vacuum at distance $d$ from the body is

$$F(d) = \frac{\alpha}{2} \frac{\partial^2}{\partial z_1 \partial z_2} \langle \delta\phi(z_1)\ \delta\phi(z_2) \rangle|_{z_1 = z_2 = d}, \tag{3.23}$$

which can be written in terms of the integrated spectrum of electric field fluctuations as

$$F(d) = \frac{\alpha}{\pi} \int_0^\infty d\omega C_{\delta E_z\ \delta E_z}(d, d, \omega). \tag{3.24}$$

The $C_{\delta E_z\ \delta E_z}(d, d, \omega)$ in Eq. (3.24) is the same as $C_{11}(d, d, \omega)$ from Eq. (1.27).

The voltage noise arising exclusively from dielectric fluctuations is obtained by setting the charge carrier density to 0 ($\bar{\rho} = 0$) in Eq. (3.20). In this limit, the sample physically represents a dielectric continuum, and the voltage noise is from a semi-infinite dielectric slab,

$$C_{\delta\phi\ \delta\phi}(\mathbf{r}_1 = \mathbf{0}, z_1, \mathbf{r}_2 = \mathbf{0}, z_2; f) = \frac{k_B T}{2\pi\epsilon_0 \omega (z_1 + z_2)} \frac{\epsilon''_{\mathrm{rel}}(\omega)}{|\epsilon_{\mathrm{rel}}(\omega) + 1|^2}, \tag{3.25}$$

where

$$\epsilon_{\mathrm{rel}}(\omega) = \epsilon'_{\mathrm{rel}}(\omega) - i\epsilon''_{\mathrm{rel}}(\omega). \tag{3.26}$$

The semi-infinite dielectric limit in Eq. (3.25) is also obtained in Chapter 2, when the thickness of the thin film organic polymer goes to infinity, i.e., $h \to \infty$ in Eq. (2.20), and the voltage noise is calculated in the quasistatic limit. Another limit of interest is when $\epsilon_{\text{rel}}(\omega) = 1$ and the charge carrier density becomes vanishingly small, $\bar{\rho} \to 0$. In this limit, the voltage noise above the sample arises entirely from the dynamics of dilute charge carriers, and a linear dependence in $\bar{\rho}$ is obtained,

$$C_{\delta\phi\,\delta\phi}(\mathbf{r}_1 = \mathbf{0}, z_1, \mathbf{r}_2 = \mathbf{0}, z_2; f) = \left(\frac{\bar{\rho} e^2 D}{4\pi\epsilon_0^2 \omega^2 d}\right) \mathrm{Re} \int_0^\infty \mathrm{dy}\; \mathrm{e}^{-\mathrm{y}(\mathrm{z}_1+\mathrm{z}_2)/\mathrm{d}} \left(\frac{\sqrt{y^2 + i\omega d^2/D} - \mathrm{y}}{\sqrt{y^2 + i\omega d^2/D}}\right). \tag{3.27}$$

The same expression for voltage noise is obtained from non-interacting charges diffusing in space for $z < 0$, when these charges are confined below the interface at $z = 0$ by a reflecting boundary condition as follows,

$$C_{\delta\phi\,\delta\phi}(\mathbf{r}_1 = \mathbf{0}, z_1, \mathbf{r}_2 = \mathbf{0}, z_2; f) = 2\bar{\rho} \int d\mathbf{r}_i \int_0^\infty dz_i \int d\mathbf{r}_f \int_0^\infty dz_f \phi(\mathbf{r}_i, z_i + z_1)\phi(\mathbf{r}_f, z_f + z_2)$$

$$\times \int_0^\infty dt \cos(\omega t) K_{\parallel}(\mathbf{r}_f, \mathbf{r}_i, t) K_{\perp}(z_f, z_i, t), \tag{3.28}$$

$$\phi(\mathbf{r}, z) = \frac{e}{4\pi\epsilon_0 \sqrt{r^2 + z^2}}, \tag{3.29}$$

$$K_{\parallel}(\mathbf{r}_f, \mathbf{r}_i, t) \equiv \frac{1}{4\pi D t} e^{-(\mathbf{r}_f - \mathbf{r}_i)^2/4Dt}, \tag{3.30}$$

$$K_{\perp}(z_f, z_i, t) = \frac{1}{\sqrt{4\pi D t}} \left(e^{-(z_f - z_i)^2/4Dt} + e^{-(z_f + z_i)^2/4Dt}\right). \tag{3.31}$$

Here, $K_{\parallel}$ is the diffusion propagator in the $xy$ plane, and $K_{\perp}$ is the diffusion propagator in $z$-direction for charge motion confined to $z < 0$. The diffusion constant is taken to be the same in all 3 dimensions. Eq. (3.28) when evaluated gives the same expression as in Eq. (3.27). Hence, the voltage noise of our model starting from the Maxwell's equations coupled to diffusive charge transport, recovers the non-interacting charge diffusion result from Eq. (3.28) in the dilute carrier density limit ($\bar{\rho} \to 0$) in vacuum. Having established that this model correctly

predicts voltage noise in the limiting cases when noise is due to 1) dielectric fluctuations, and 2) non-interacting charge carrier diffusion alone, we are now in a position to study the effects of introducing coupling between dielectric fluctuations, carrier dynamics, and Coulomb interactions between the charge carriers. The numerical calculations in Sec. 3.2 explore these properties.

## 3.2 Results and Discussion

The numerical calculations of the voltage noise, and the spectral density of frequency fluctuations, are plotted against $f = \omega/2\pi$ for a wide range of frequencies, and show experimentally accessible frequencies ranging from tenths of Hz to hundred Hz. Carrier mobilities in organic semiconductors range over several orders of magnitude between $10^{-14}$ $m^2V^{-1}s^{-1}$ to $10^{-6}$ $m^2V^{-1}s^{-1}$ [2, 11, 70]. For these calculations, an intermediate value of mobility in these materials $\mu = 10^{-10}$ $m^2V^{-1}s^{-1}$ is used. The diffusion constant corresponding to this mobility is obtained from the Einstein relation at T = 300 K, $D = 2.6 \times 10^{-12}$ $m^2s^{-1}$. Two frequencies are connected to transport: $\Omega \equiv \kappa^2 D$ is associated with carrier diffusion over a Debye length in vacuum, and $\Omega_d \equiv D/d^2$ is associated with carrier diffusion over a distance comparable to the tip-sample distance.

Figure (3.1) shows the spectral density of voltage fluctuations at a tip-sample height of $d = 100$ nm due to Coulomb interactions and carrier dynamics in the absence of dielectric fluctuations, that is in vacuum ($\epsilon_{\text{rel}} = 1$). In the limit of $\omega >> \Omega$ and $\omega >> \Omega_d$ for $\epsilon_{\text{rel}} = 1$, the voltage noise in Eqs. (3.20) and (3.28) goes to the same expression,

$$C_{\delta\phi\,\delta\phi}(\mathbf{r}_1 = \mathbf{0}, z_1, \mathbf{r}_2 = \mathbf{0}, z_2; f) = \frac{k_B T \Omega}{4\pi\epsilon_0 (z_1 + z_2)\omega^2}. \tag{3.32}$$

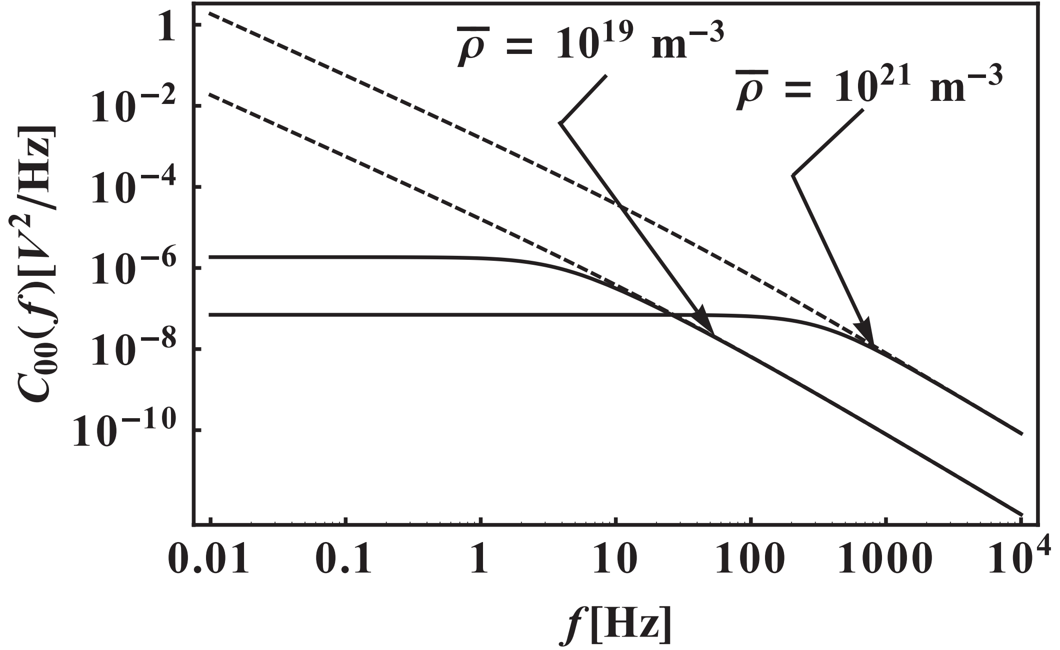


Figure 3.1: Autocorrelation function of fluctuations in potential, denoted as $C_{00}(f)$ on the y-axis, vs. frequency, at a tip-sample height $d = 100$ nm for charge carriers diffusing in vacuum. Solid curves for interacting carriers are calculated from Eq. (3.20) with $\epsilon_{\text{rel}} = 1$, while dashed curves for non-interacting carriers are calculated using Eq. (3.28). The charge carrier densities are as indicated. Figure reproduced from Ref.[32], with permission.

Eq. (3.32) is proportional to the charge carrier density, and inversely proportional to $\omega^2$. In the opposite limit of $\omega << \Omega$, and $\omega << \Omega_d$, the voltage noise is independent of frequency, and depends on carrier density to all orders. For a high carrier density limit in addition to the low frequency limit, the voltage noise in Eq. (3.20) is inversely proportional to $\bar{\rho}$ since $\Omega \propto \bar{\rho}$,

$$C_{\delta\phi\,\delta\phi}(\mathbf{r}_1 = \mathbf{0}, z_1, \mathbf{r}_2 = \mathbf{0}, z_2; f) = \frac{k_B T}{2\pi\epsilon_0\Omega(z_1 + z_2)}. \tag{3.33}$$

The solid lines in Fig. (3.1) show these two limits from Eqs. (3.32) and (3.33). The voltage noise in the high frequency limit is proportional to carrier density and to $f^{-2}$, while the low frequency limit is inversely proportional to carrier

density, and $\propto f^0$. The dashed lines correspond to the calculations of voltage noise of non-interacting charge carrier diffusion from Eq. (3.28). These dashed lines, in the high frequency limit, are proportional to $f^{-2}$ and carrier density, and are indistinguishable from the solid lines. Thus, in the high frequency limit the carrier interactions are not important in Eq. (3.20). In the low frequency limit, the dashed lines are $\propto f^{1.5}$ and $\propto \bar{\rho}$, and do not show the suppression of noise with increase in carrier density due to Coulomb interactions as observed in the solid-line calculations.

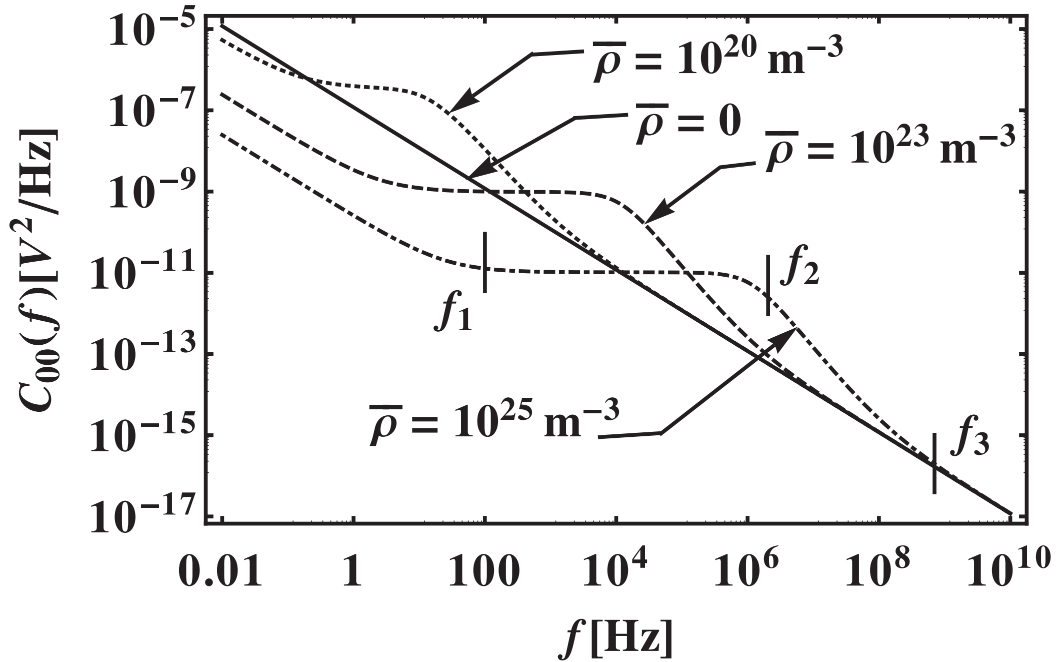


Figure 3.2: Autocorrelation function of fluctuations in potential, denoted as $C_{00}(f)$ on the y-axis, vs. frequency, at a tip-sample height $d$ = 100nm for charge carriers diffusing in a dielectric medium. Various charge densities are indicated and the characteristic frequencies are marked $f_1$,$f_2$ and $f_3$. Details in text. Figure reproduced from Ref.[32], with permission.

Figure (3.2) shows the spectral density of voltage fluctuations for various charge carrier densities from Eq. (3.20). Fig. (3.2) differs from the solid lines in

Fig. (3.1) in having a complex-valued dielectric function of the material rather than vacuum ($\epsilon_{\rm rel} = 1$). The dielectric function of the material is taken to be a frequency independent quantity, with $\epsilon'_{\rm rel} = 4$ and $\epsilon''_{\rm rel} = 0.05$. Thus, Fig. (3.2) allows us to study the effects of carrier interactions and dynamics in the absence of frequency dependence of the dielectric function. The solid line is voltage noise spectrum for $\bar{\rho} = 0$ in Eq. (3.20), and is $\propto f^{-1}$. In the high frequency limit, all of the broken curves representing non-zero charge densities converge to the $\bar{\rho} = 0$ result. In this limit, charge carrier dynamics and interactions are not seen and all the broken curves converge to the pure dielectric ($\bar{\rho} = 0$) result.

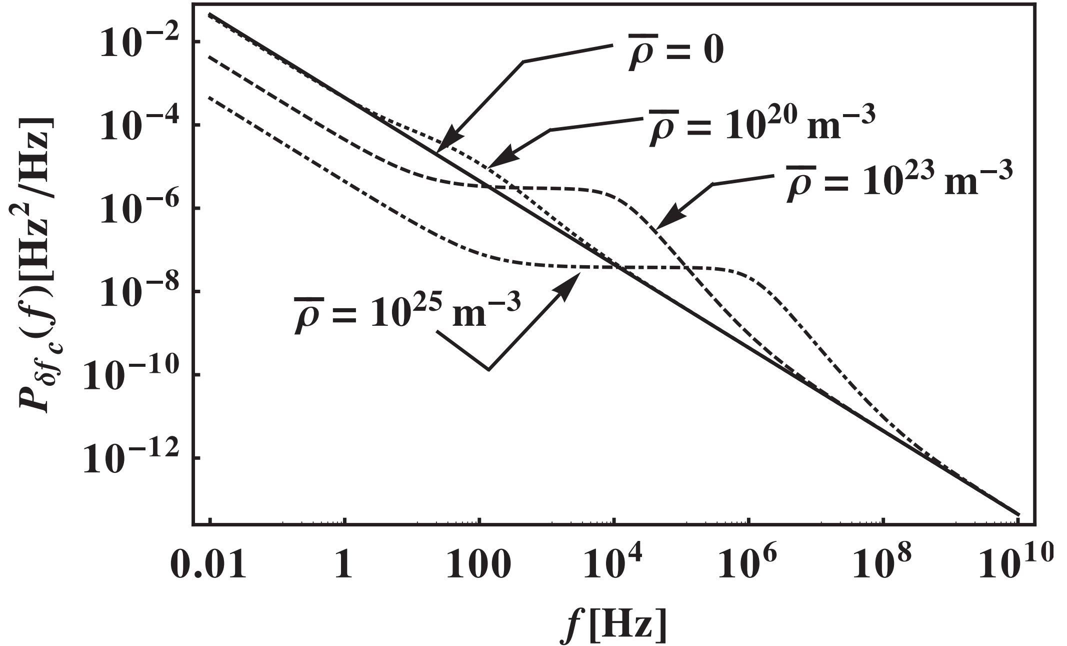


Figure 3.3: Power spectrum of cantilever resonance frequency fluctuations denoted $P_{\delta f_c}(f)$ as a function of frequency, at a tip-sample height $d = 100$ nm above the vacuum-sample interface for the same parameters as in Fig. (3.2). Figure reproduced from Ref.[32], with permission.

In the low frequency limit, the voltage noise spectrum for the broken curves is $\propto f^{-1}$, but depends only on $\kappa^2 = 2\bar{\rho}e^2/\epsilon_0 k_B T$ and is independent of the car-

rier mobility and diffusion constant. In this limit, Eq. (3.20) depends on $\bar{\rho}$ to all orders and carrier interactions are responsible for the suppression in noise with increasing charge carrier density evident in Fig. (3.2). The broken curves corresponding to non-zero $\bar{\rho}$ in Fig. (3.2) show three characteristic frequencies, $f_1 < f_2 < f_3$. For $\epsilon'' << \epsilon'$, these frequencies are numerically determined to be approximately

$$\begin{aligned} f_1 &\approx \sqrt{\frac{\Omega_d}{\Omega}}\left(\frac{\Omega''}{2\pi}\right), &(3.34)\\ f_2 &\approx \frac{\Omega'}{2\pi}, &(3.35)\\ f_3 &\approx \frac{\Omega^2}{2\pi\Omega''}. &(3.36)\end{aligned}$$

Here,

$$\Omega'(\omega) \equiv \frac{\Omega\epsilon'_{\text{rel}}(\omega)}{|\epsilon_{\text{rel}}(\omega)|^2},\ \Omega''(\omega) \equiv \frac{\Omega\epsilon''_{\text{rel}}(\omega)}{|\epsilon_{\text{rel}}(\omega)|^2}, \tag{3.37}$$

are two additional frequency scales obtained from $\Omega$ (modified by the relative dielectric function of the material). The frequency regimes when partitioned with respect to $f_1$, $f_2$ and $f_3$ can be interpreted physically for $\bar{\rho} = 10^{25}\text{m}^{-3}$ in Fig. (3.2). In the low frequency regime ($f < f_1$) corresponding to the longest time scales, the voltage noise spectrum attains its low frequency asymptotic static behaviour from the inter-carrier interactions in the dielectric material. In the plateau region ($f_1 < f < f_2$) in Fig. (3.1), voltage fluctuations are independent of frequency, and the voltage noise spectrum arises primarily from interacting carriers in vacuum. In the intermediate regime ($f_2 < f < f_3$) regime, the voltage noise is $\propto f^{-2}$ and the voltage noise spectrum arises from non-interacting charge carriers diffusing in vacuum in the presence of the charge density indicated in Fig. (3.1). In the high frequency asymptotic limit ($f > f_3$) reflecting the shortest timescales, no effects from carrier transport and interactions are seen, and a pure dielectric ($\bar{\rho} = 0$) result is observed for all charge densities.

Fig. (3.3) is the spectral density of frequency fluctuations calculated from the voltage noise spectrum in Eq. (3.20) using Eqs. (1.27) and (1.30). The parameters used are the same as those for the voltage noise spectrum in Fig. (3.2). The calculation of the power spectrum of frequency fluctuations requires a model for the tip-sample capacitance. In Chapter 2, an approximate expression for the capacitance Eq. (2.25) is used– a charged sphere of radius $R$ over a dielectric slab of thickness $h$ on a conductor. Here an exactly correct expression for a charged sphere of radius R with centre at a height d + R above the semi-infinite dielectric slab with a relative dielectric function $\epsilon'_{\rm rel}(0)$ is used,

$$c(d) = 4\pi\epsilon_0 R \sum_{n=1}^{\infty} \left( \frac{\epsilon'_{\rm rel}(0) - 1}{\epsilon'_{\rm rel}(0) + 1} \right)^{n-1} \frac{\sinh\alpha}{\sinh n\alpha}, \tag{3.38}$$

$$\alpha = \cosh^{-1}(1 + d/R). \tag{3.39}$$

In this Chapter, Eq. (3.38) is used to compute the tip-sample capacitance with $R = 40$ nm and $V_{\rm ts} = 5$ V, $f_c = 65$ kHz, and $k_c = 3.5$ Nm$^{-1}$ are used to compute the power spectrum of frequency fluctuations $P_{\delta f_c}(f)$ via Eq. (1.30). Fig. (3.3) shows similar frequency regimes, carrier density, and mobility dependencies for the spectral density of frequency fluctuations as that observed for voltage noise spectrum in Fig. (3.2). This agreement does not imply that voltage noise is the dominant term in Eq. (1.30). The contributions from all the noise spectrums of potential and its derivatives to the total noise spectra are discussed below in Fig. (3.6).

Figs. (3.2) and (3.3) show the effects of carrier dynamics, with inter-carrier interactions in the medium for a frequency-independent relative dielectric function $\epsilon_{\rm rel} = 4 - i0.05$. In Figs. (3.4) and (3.5), the power spectrum of frequency fluctuations is shown when a frequency dependent dielectric function is added to the carrier dynamics, and interactions. A Debye form for the relative dielec-

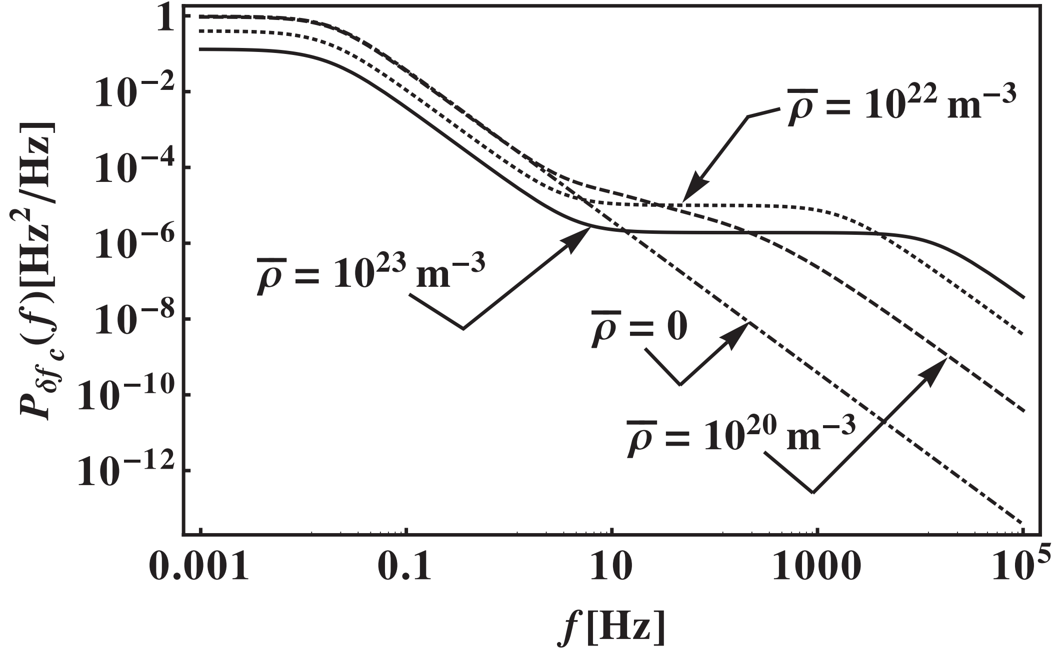


Figure 3.4: Power spectrum of cantilever resonance frequency fluctuations denoted $P_{\delta f_c}(f)$ as a function of frequency, at a tip-sample height $d$ = 100 nm above the vacuum-sample interface for various charge densities. The relative dielectric function has the Debye form with a relatively long relaxation time, $\tau$ = 20 s. Figure reproduced from Ref.[32], with permission.

tric function, $\epsilon_{\text{rel}}(\omega) = \epsilon_\infty + (\epsilon_s - \epsilon_\infty)/(1 + i\omega\tau)$ with $\epsilon_s = 10.4$ and $\epsilon_\infty = 3.6$, is used in these figures. Fig. (3.4) uses a relatively long timescale of dielectric fluctuations, $\tau$ = 20 s, while Fig. (3.5) uses a fast timescale, $\tau = 10^{-5}$ s. $\epsilon_s$ and $\epsilon_\infty$ are chosen such that the Debye form of the dielectric function for $\tau$ = 20 s reduces to the static complex number dielectric function $\epsilon_{\text{rel}} = 4 - i0.05$ at $f$ = 1 Hz. Figure. (3.4) shows the power spectrum of frequency fluctuations at $d$ = 100 nm for various charge carrier densities. The carrier density $\bar{\rho} = 0$ only shows the power spectrum from dielectric fluctuations. For $f << \tau^{-1}$ the power spectrum is constant in frequency, while for $f >> \tau^{-1}$ the power spectrum is $\propto f^{-2}$. Two additional timescales are introduced with increasing carrier density as seen in Figure. (3.4). A noise suppression is observed with increasing charge density for asymptotic

low frequencies while noise enhancement is seen for aymptotic high frequencies. The high frequency limit of Eq. (3.20) when a Debye form of the relative dielectric functions is used is

$$C_{\delta\phi\,\delta\phi}(\mathbf{r}_1 = \mathbf{0}, z_1, \mathbf{r}_2 = \mathbf{0}, z_2; f) = \frac{k_B T}{2\pi\epsilon_0(1+\epsilon_\infty)^2(z_1+z_2)\omega^2}\left(\Omega + \frac{\epsilon_s - \epsilon_\infty}{\tau}\right). \quad (3.40)$$

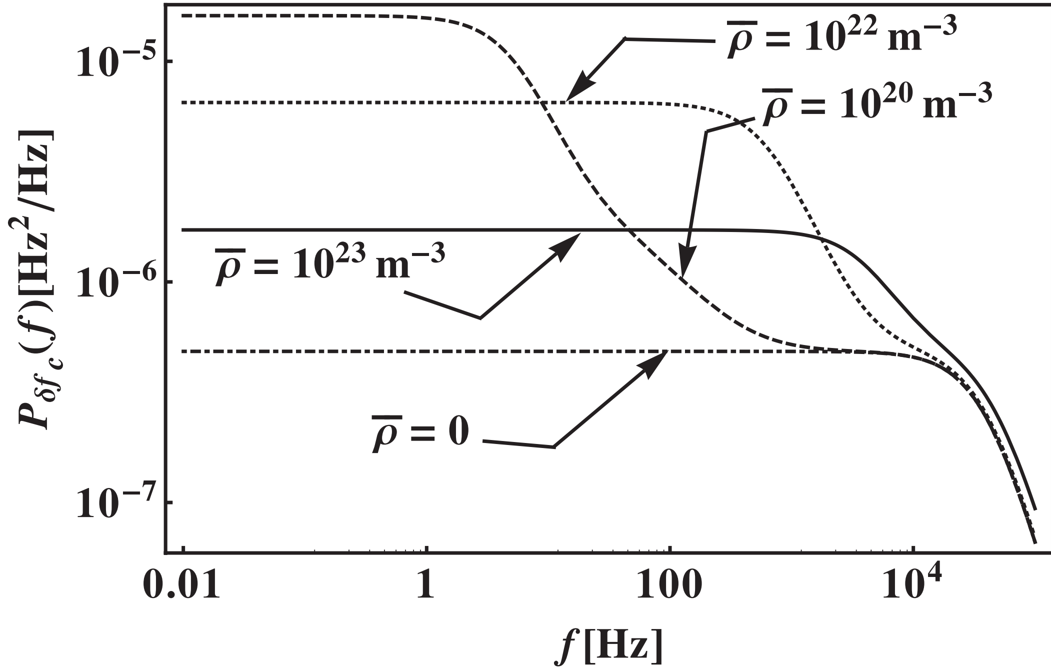


Figure 3.5: Power spectrum of cantilever resonance frequency fluctuations denoted $P_{\delta f_c}(f)$ as a function of frequency, at a tip-sample height $d$ = 100 nm above the vacuum-sample interface for various charge densities. The relative dielectric function has the Debye form with a relatively short relaxation time, $\tau = 10^{-5}$ s. Figure reproduced from Ref.[32], with permission.

In contrast to Fig. (3.4), Fig. (3.5) does not show the asymptotic high frequency limit of the pure dielectric result ($\bar{\rho} = 0$) for all carrier densities. For the parameters used in Fig. (3.4), $\Omega >> \epsilon_s - \epsilon_\infty$ and the high frequency asymptotic limit is proportional to carrier density as predicted in Eq. (3.40). Fig. (3.5) shows

a similar power spectrum calculation as Fig. (3.4) but a different relaxation time, $\tau = 10^{-5}$ s. For the charge densities as high as $10^{22}$ m$^{-3}$, $\Omega << (\epsilon_s - \epsilon_\infty)/\tau$ and the high frequency asymptotic limit is the same as the dielectric result without charge carriers. Unlike the result in Fig. (3.4) where the frequency scales of carrier transport are seen for higher frequencies than $\tau^{-1}$, when the relaxation times is smaller, the dielectric fluctuations dominate and the frequency scales of carrier transport are not seen in Fig. (3.5) for high frequencies. The low frequency behaviour in Fig. (3.5) shows an increase in noise when charge density goes from 0 to $10^{20}$m$^{-3}$, while a decrease in noise is seen for the charge density going from $10^{22}$m$^{-3}$ to $10^{23}$m$^{-3}$. Also, the dot-dashed curve for $\bar{\rho} = 0$ in Fig. (3.5) shows the same asymptotic limits– $\propto f^0$ for low frequency and $\propto f^{-2}$ for high frequency– as that in Fig. (3.4), except that the frequency scale corresponding to $\tau^{-1}$ shifts to high frequencies for smaller relaxation times, as expected.

The tip-sample height $d$ was maintained constant at 100 nm in Figs. (3.1)-(3.5). The $d$-dependence of the noise is explored by calculating the frequency jitter from the power spectrum of frequency fluctuations using Eq. (1.28). The frequency jitter is shown in Figs. (3.6) and (3.7) as a function of the tip-sample height $d$. The values $f_{\min} = 0.2$ Hz, and $f_{\max} = 3$ Hz are taken in Eq. (1.28), since the EFM measurements on organic transistor with a commercial cantilever were made in this frequency range [20, 32]. Fig. (3.6) shows the contributions from individual auto- and cross-correlation functions of potential, field and field derivatives in Eq. (1.30), when integrated from $f_{\min}$ to $f_{\max}$. The parameters used in the calculation are $\bar{\rho} = 10^{21}$m$^{-3}$, $D = 2.6 \times 10^{-12}$m$^2$s$^{-1}$, $\epsilon'_{\text{rel}} = 4$, and $\epsilon''_{\text{rel}} = 0.05$. Frequency jitter calculated from Eq. (1.28) is indicated as Total in Fig. (3.6). The label $z, \phi$ refers to integrated jitter contribution from crosscorrelation function of fluctuations in electric field in z-direction(z) and potential($\phi$),

$z, \phi \propto 4c^{(1)}(d)c^{(2)}(d) \int_{f_{\min}}^{f_{\max}} C_{\delta E_z \delta\phi}(f)$. Similarly, the label $\phi, \phi \propto (c^{(2)}(d))^2 \int_{f_{\min}}^{f_{\max}} C_{\delta\phi\delta\phi}(f)$, and so on. As seen in previous jitter calculations done for a dielectric with no charge carriers [20, 21], Fig. (3.6) for tip-sample heights ranging from $d = 50$ nm to $d = 600$ nm, shows that the dominant contribution to jitter arises from the term containing an autocorrelation function of fluctuations in $z$-gradient of $z$ component of the electric field, while the least contribution arises from a term involving the autocorrelation function of potential fluctuations.

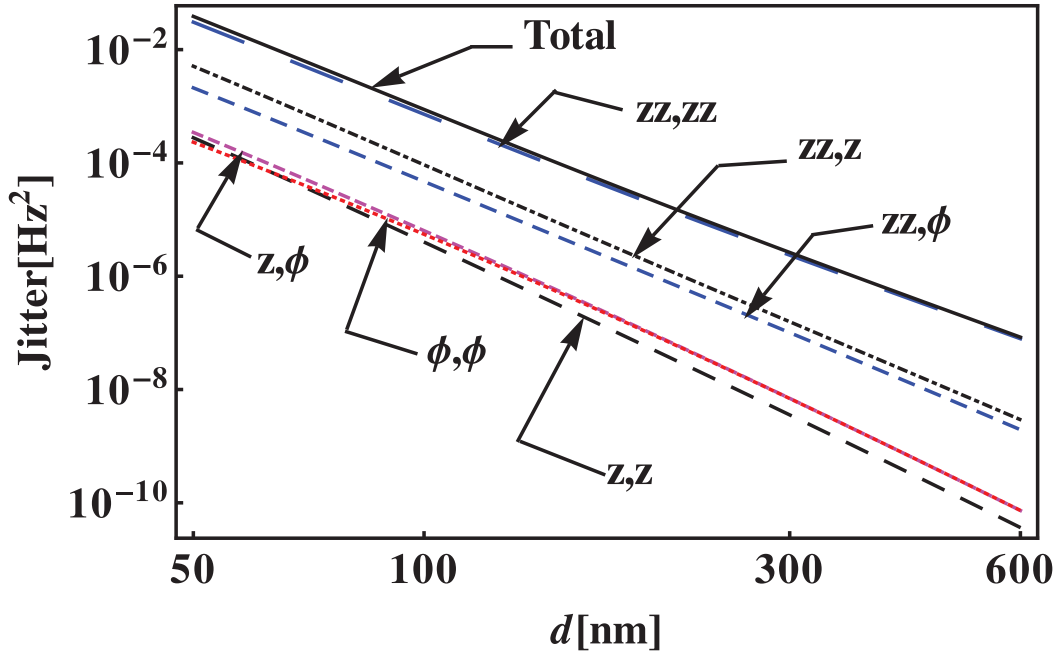


Figure 3.6: The solid line shows cantilever frequency jitter as a function of tip-sample height for carrier density $\bar{\rho} = 10^{21}$ m$^{-3}$. Other lines indicate contributions to jitter from auto- and cross-correlation of fluctuations in potential, electric field, and electric field gradient (Eq. 1.30). Label $z$,$\phi$ is the crosscorrelation function of fluctuations in the $z$ component of the electric field and potential and, $zz$,$z$ is that of $z$-gradient of the $z$ component of the electric field and the $z$ component of the electric field. Details in text. Figure reproduced from Ref.[32], with permission.

Depending on the tip-sample height in the EFM measurement, the jitter ob-

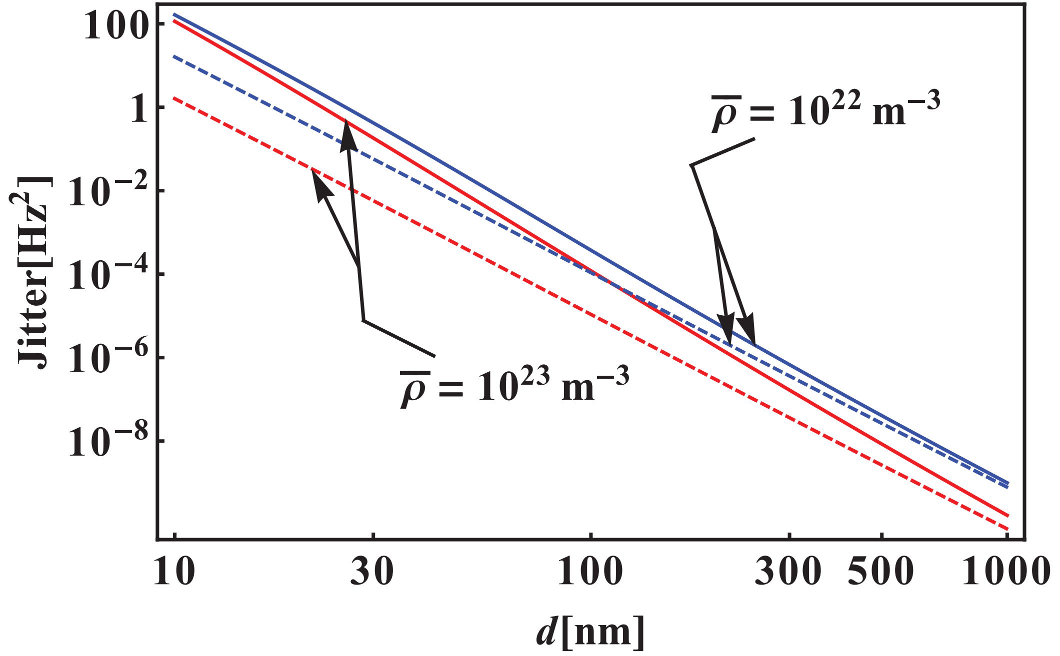


Figure 3.7: Cantilever frequency jitter is shown as a function of tip-sample separation. The charge carrier densities are as indicated. Jitter calculated from potential autocorrelation in Eq. (3.20) are the solid curves and jitter calculated from potential autocorrelation in Eq. (3.25) with an effective relative dielectric function that includes conductivity are the dashed curves. Both the calculations are in good agreement in the limit of large *d*. Figure reproduced from Ref.[32], with permission.

servable of the experiment is shown to probe different characteristics of the carrier dynamics from the model calculations. Fig. (3.7) shows frequency jitter calculated for two carrier densities: $\bar{\rho} = 10^{22}\text{m}^{-3}$, and $\bar{\rho} = 10^{23}\text{m}^{-3}$. In the limit of $d \to 0$ in Eq. (3.20), potential autocorrelation reduces to a pure dielectric result with no charge carriers, as in Eq. (3.25). In the opposite limit of large tip-sample separation, the potential autocorrelation takes the form of Eq. (3.25) with an effective relative dielectric function that includes a contribution to the dielectric spectrum from the conductivity from the charge carriers $\epsilon_{\text{eff}}(\omega) = \epsilon_{\text{rel}}(\omega) - i\sigma_0/\epsilon_0\omega$ (Eq. (3.7)). This effective relative dielectric function for the medium is obtained by substituting Ohm's law, $\mathbf{J} = \sigma_0\mathbf{E}$, in Eq. (3.2) (with the contribution from ther-

mal fluctuations in carrier density neglected [24]. In Fig. (3.7), the solid lines represent the full calculation of frequency jitter from Eqs. (3.20), (1.30), and (1.28), while the dashed lines are from Eqs. (3.25), (1.30), and (1.28), for $\epsilon_{\rm rel} \rightarrow \epsilon_{\rm eff}$ in Eq. (3.25). The diffusion constant used in the calculation is $D = 2.7 \times 10^{-12}$ m$^2$s$^{-1}$. Within the assumptions of the model, Fig. (3.7) shows that a cantilever very close to the sample only probes dielectric continuum fluctuations while the cantilever far way probes a continuum result but with $\epsilon_{\rm rel} \rightarrow \epsilon_{\rm eff}$. Figure (2) of Ref.[14] shows the calculation of the Casimir-Lifshitz free energy for two semi-infinite dielectric slabs with free charges as a function of separation between them. This figure shows a similar limiting behaviour for the free energy as that observed in the Fig. (3.7) for the large tip-sample separation– that is, the full calculation approaches the $\epsilon_{\rm eff}(\omega)$ result. This finding shows that an accurate picture may not be modelled by the use of effective relative dielectric function because thermal fluctuations from carrier dynamics are not negligible at finite tip-sample separations.

## 3.3 EFM measurements on an organic field effect transistor

The experiments were done by Nikolas Hoepker in Professor Marohn's group at Cornell University [20, 32]. The major part of this section is from Refs. [20, 32]. Details of the experiment are provided here since they are relevant for the comparison to the theoretical calculations. A molecularly doped polymer transistor was fabricated with TPD (N,N′-Bis-(3-methylphenyl)-N,N′-bis-(phenyl)-benzidine) as the charge-transporting molecule [5, 36, 53, 54], and high molecular weight polystyrene as the host polymer. Charge hopping models [3, 6, 17, 38, 41] describe well the dependence of charge transport on molecule

concentration, electric field, and temperature in these molecularly doped polymer systems. The transistor substrates were fabricated by growing 315 nm of $SiO_2$ on $n^+$-Si, followed by a patterned deposition of 5 nm of Cr and 30 nm of Au to produce interdigitated source and grain electrodes. The channel length was 5 $\mu$m. From the oxide thickness and the dielectric constant of $SiO_2$ of $4.65\epsilon_0$ [25], the capacitance per area across the dielectric is estimated to be $C_i = 4.65\epsilon_0/315\text{nm} = 1.3 \times 10^{-4}$ $\text{Fm}^{-2}$. The thickness of the TPD film was determined to be 70 nm by profilometry. The device is sketched in Fig. 3.8. The electrical characteristics of the device were determined, and a current-voltage plot is shown in the Supplementary Material of Ref. [32]. From these mea-

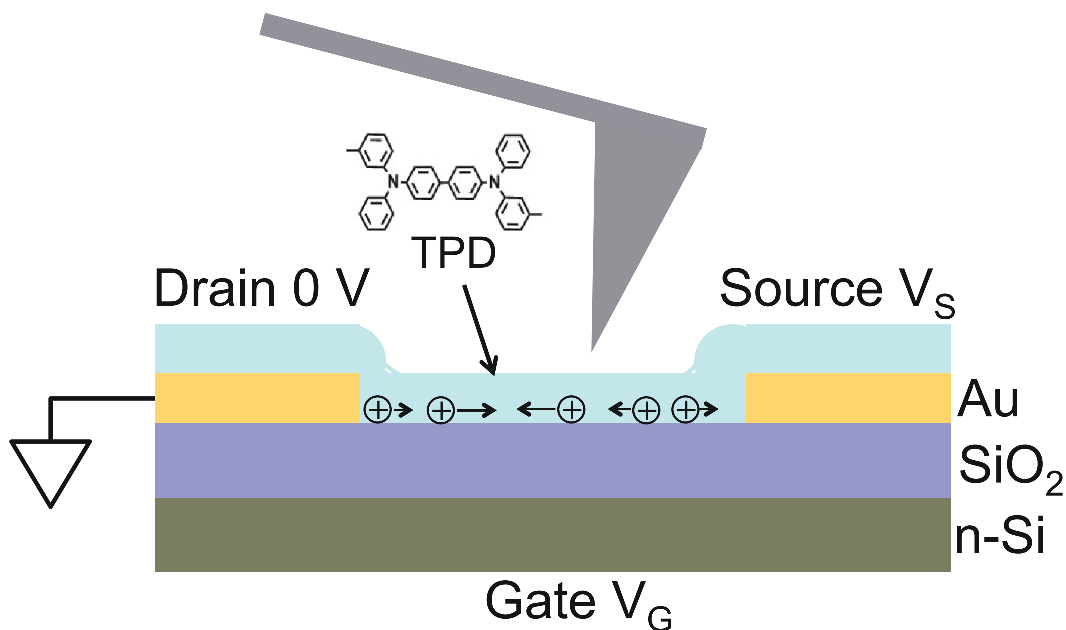


Figure 3.8: Charged cantilever tip is positioned above an organic field-effect transistor. Figure reproduced from Ref.[32], with permission.

surements a (saturation) mobility of $\mu = 2.7 \times 10^{-10}$ $\text{m}^2\text{V}^{-1}\text{s}^{-1}$ and a threshold voltage of $V_t = -2.9$ V was extracted. The cantilever ($f_c = 64,058$ Hz, $k_c = 3.5$ N/m) was driven into self-oscillation using a custom-built feedback

circuit. A temperature-tuned fiber-optic interferometer ($\lambda$ = 1310 nm) was used to track the position of the cantilever. The cantilever position was converted into a frequency versus time signal using a software frequency demodulator. Frequency noise spectra were obtained from the Fourier transform of the autocorrelation function of the frequency fluctuations as in Eq. (1.29). More detail on the electric force microscope measurements and the frequency demodulator can be found in Refs. [68] and [21] and their Supporting Information.

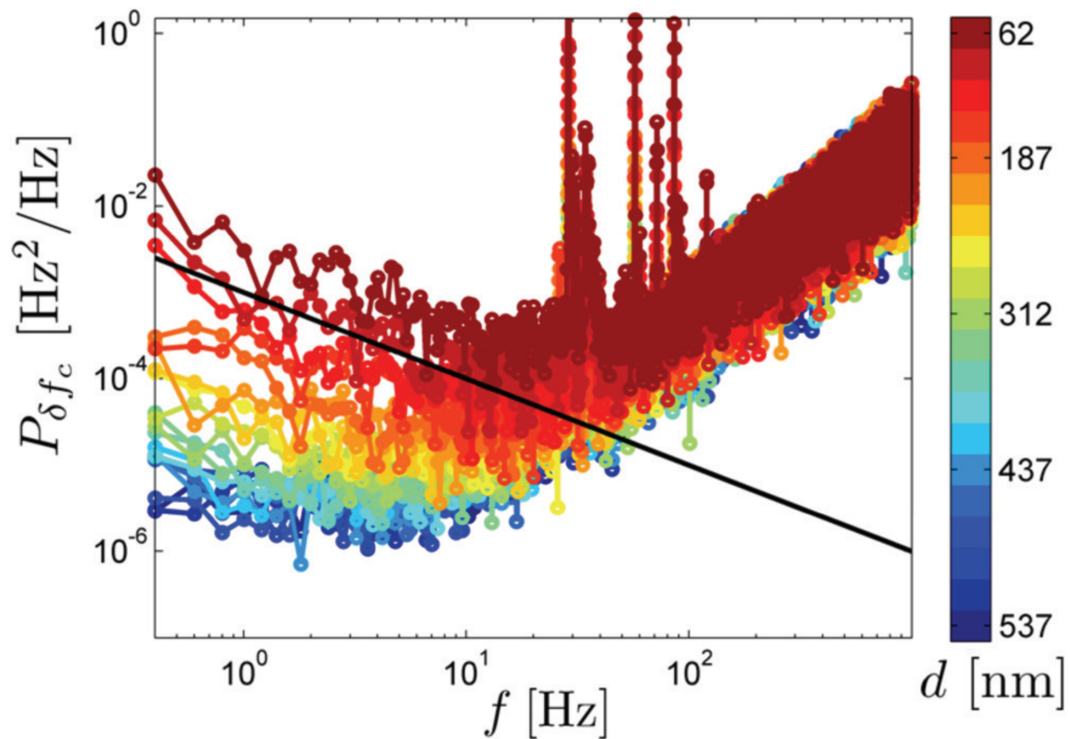


Figure 3.9: Measured power spectra of cantilever frequency fluctuations above an organic field effect transistor are shown for various tip-sample separations. The tip-sample and gate voltages are respectively $V_{\text{ts}} = -3$ V and $V_G = -40$ V. The frequency dependence $f^{-1}$ is shown. Figure reproduced from Ref.[32], with permission.

Fig. (3.9) shows power spectra of cantilever frequency fluctuations for various tip-sample heights for a gate voltage of $V_G = -40$ V. The source and drain

electrodes was grounded in this experiment. Two frequency regimes are observed for all spectra: 1) a low-frequency regime where $P_{\delta f_c} \propto f^{-1}$ and the magnitude of the frequency noise increases with decreasing $d$, and 2) a regime for $f > 20$ Hz where $P_{\delta f_c} \propto f^2$ with superposed frequency spikes. For $f > 20$ Hz, the $f^2$ regime is attributed to the photodetector noise, and the spikes are from mechanical vibrations similar to the power spectra meaurements on PVAc shown in Fig. (2.2) of Chapter 2 [20, 21].

The dependence of the power spectrum on the tip-sample separation implies that the low frequency noise is due to dynamical fluctuations in the organic semiconductor samples. The $d$-dependence of cantilever frequency noise was further examined by integrating the measured power spectra in Fig. (3.9) using Eq. (1.28), from $f_{\mathrm{min}} = 0.2$ Hz to $f_{\mathrm{max}} = 3$ Hz. Cantilever frequency jitter from three gate voltages– $V_G = 0$ (circles), $-20$ V (squares), and $-40$ V (crosses)– are shown as a function of tip-sample separation $d$ in Figure. (3.10). The data marked (x) were measured with cantilever over the source electrode in Fig. (3.8) as a control experiment, and are seen to be not significantly different from the other data (Fig. (3.8)). These data are expected to agree with data measured for $V_G = 0$ V, and to show the effect of dielectric fluctuations from TPD as well as any residual free charge. An increase in gate voltage increases the charge carrier density in the channel of transistor. The measurements in Fig. (3.10) show however that the cantilever frequency noise is nearly independent of carrier density. The solid blue line in Fig. (3.10) is calculated from Eq. (3.28), corresponding to a model of non-interacting diffusing charge carriers in a two-dimensional plane with an areal charge carrier density of $\rho_A$. To model two-dimensional charge diffusion $K_\perp \to \delta(z_i - z_f)$, and $2\bar{\rho} \to \rho_A \delta(z_i)$ in Eq. (3.28). The areal charge density used in Fig. (3.10) is calculated from the capacitance per area of the $SiO_2$ gate

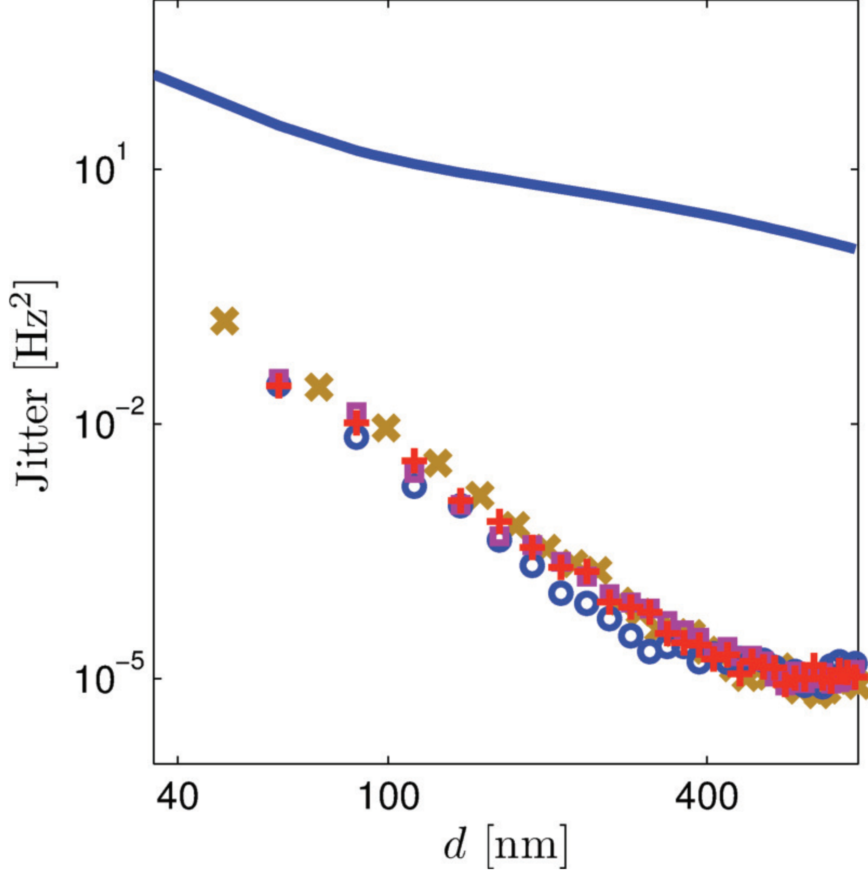


Figure 3.10: Observed cantilever frequency noise (jitter) integrated from 0.2 Hz to 3.0 Hz as a function of tip sample distance $d$ above a TPD transistor. The frequency noise was measured at applied gate voltages of $V_G = 0$ (circles), $V_G = -20$ V (squares), $V_G = -40$ V (crosses), and, as a control experiment, over the source electrode (x). The jitter for $V_G = -40$ V is obtained from frequency integration of the spectra in Fig. 3.9. Also shown is a prediction from freely diffusing carriers in the absence of a dielectric (solid blue line). Figure reproduced from Ref.[32], with permission.

dielectric as follows: $\rho_A = C_i(V_{\text{ts}} - V_G)/e = 3.0 \times 10^{16}\ \text{m}^{-2}$ with $C_i = 1.3 \times 10^{-4}\ \text{Fm}^{-2}$, $\text{V}_\text{G} = -40$ V, and $\text{V}_{\text{ts}} = -2.9$ V. The diffusion coefficient is estimated from the Einstein relation $D = k_B T \mu / e$, using the measured saturation mobility in the polymer as stated above in Sec. 3.3. As can be seen in Fig. (3.10), the calculated jitter (the solid blue line) overestimates the measured frequency noise by atleast two

orders of magnitude. The use of the Einstein relation has been shown in some organic semiconductors [62] to underestimate D by more than one order of magnitude. Correction of the diffusion constant by this factor only contributes to increase in solid blue line, however, and hence increases the discrepancy between the measured jitter and that calculated from the non-interacting carrier diffusion model. In summary, 1) the cantilever frequency noise spectrum is $\propto f^{-1}$, 2) the spectrum is insensitive to the presence of carriers over the range of gate voltages studied, and 3) a model of non-interacting diffusing carriers on a two-dimensional surface overestimates the frequency noise even after introducing corrections to Einstein relation for organic semiconductors.

Figure (3.11) shows voltage noise calculated from Eq. (3.20) for three charge densities; $\bar{\rho} = 0$(dot-dashed), $\bar{\rho} = 10^{18}$ m$^{-3}$(red dotted), and $\bar{\rho} = 2.6 \times 10^{24}$ m$^{-3}$(solid). The parameters used in the calculation are: $D = 2.6 \times 10^{-12}$ m$^2$s$^{-1}$, and $\epsilon'_{\mathrm{rel}} = 4$ and $\epsilon''_{\mathrm{rel}} = 0.05$. This value of $D$ corresponds to mobility $\mu = 10^{-10}$ m$^2$V$^{-1}$s$^{-1}$ in the Einstein relation at T = 300 K, which is comparable to the measured saturation value for the transistor. The red dashed line in Fig. (3.11) corresponds to the voltage noise calculated with the same diffusion constant and charge density $\bar{\rho} = 10^{18}$ m$^{-3}$ for non-interacting diffusing carriers from Eq. (3.28). The red dotted curve shows the three characteristic frequencies, $f_1, f_2$, and $f_3$ in Eqs. (3.34)-(3.36), similar to voltage noise in Fig. (3.2). For $f >> f_3 \approx 190$ Hz, the electrodynamic calculation with charges aymptotically approaches the dielectric result. In $f_2 < f < f_3$ with $f_2 \approx 0.15$ Hz, the noise exceeds the dielectric result due to the inclusion of the effects from non-interacting diffusing carriers. For $f < f_2$, inter-carrier interactions set in, and for $f < f_1 \approx 0.015$ Hz, an asymptotic low-frequency limit is attained. In Fig. (3.11), in the low-$f$ limit, the suppression in noise for $\bar{\rho} = 10^{18}$ m$^{-3}$ from inter-carrier

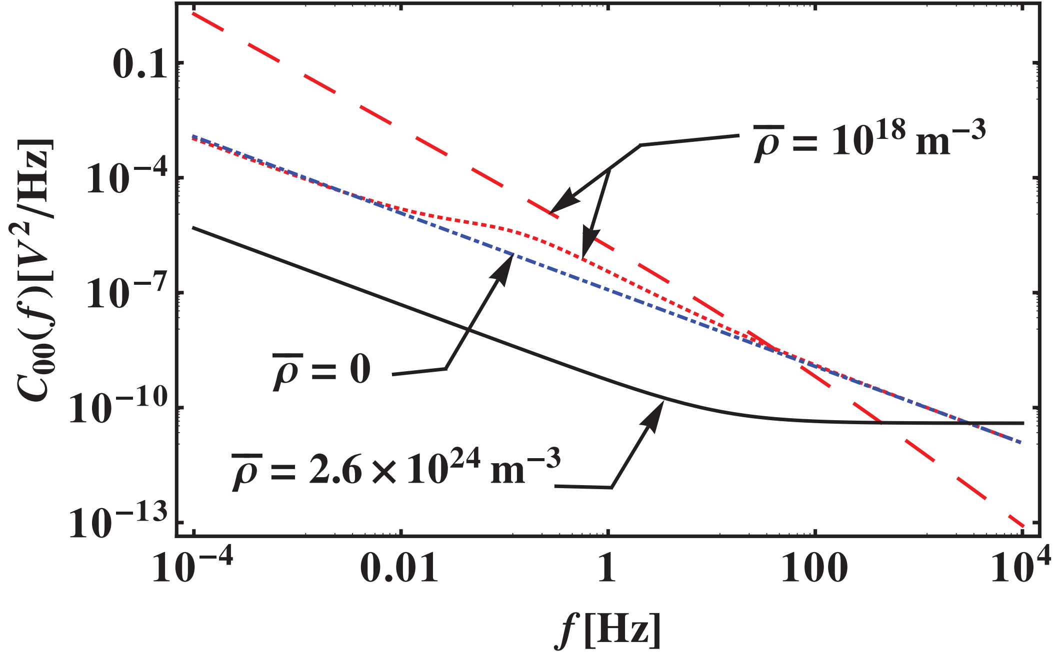


Figure 3.11: Voltage noise for a dielectric with mobile charges at $\bar{\rho} = 10^{18}$ $\mathrm{m}^{-3}$ (dots) is similar at both low and high frequencies to the noise produced by dielectric relaxation alone at $\bar{\rho} = 0$ (dot-dash). Noise at $\bar{\rho} = 10^{18}\ \mathrm{m}^{-3}$ is overestimated at low frequency by a calculation based on diffusion of noninteracting carriers at the same density in vacuum (dashes). At a higher density $\bar{\rho} = 2.6 \times 10^{24}\ \mathrm{m}^{-3}$, the solid curve shows suppression of noise at low frequency. Figure reproduced from Ref.[32], with permission.

interactions is absent, in contrast to that observed for higher carrier densities in Fig. (3.2). In the low-$f$ limit, the noise from the diffusion of non-interacting carriers in vacuum (red dashed curve) is significantly higher than the voltage noise at the same carrier density from interacting carriers in a dielectric medium. The dotted curve for $\bar{\rho} = 10^{18}\ \mathrm{m}^{-3}$ shows a case for which the charge density is high enough to show noise from noninteracting carriers in vacuum; there is not a significant difference from the dielectric result with no charge carriers. An increase in charge density leads to an increase in the characteristic frequency $f_1$ and the low-$f$ regime moves into the measurement window around 1 Hz. Additionally,

the magnitude of the noise is also suppressed as seen for $\bar{\rho} = 2.6 \times 10^{24}$ m$^{-3}$ (solid black curve) in Fig. (3.11). The three dimensional density used in this calculation is obtained from the estimated areal charge density for the organic transistor at $V_G = -40$ V using $2\bar{\rho} = \rho_A^{3/2}$. This areal charge density corresponds to a charge density in three dimensions that has a comparable mean inter-carrier separation to that estimated from the assumption that the carriers in a transistor are rigorously confined to a two-dimensional region. Although a $1/f$ dependence is observed in the low-$f$ regime that is similar to the experimental data, the magnitude of the noise is strongly suppressed by intercarrier interactions. Also, the voltage noise calculated from a semi-infinite slab at this density need not be quantitatively equal to that generated by a two-dimensional sheet with comparable mean inter-carrier separation.

The qualitative agreement of the low-$f$ region of $\bar{\rho} = 10^{18}$ m$^{-3}$ (the dotted curve in Fig. (3.11)) with experimental data is summarized as, 1) $f^{-1}$ frequency dependence, 2) more or less similar to dielectric with no charge carriers result, and 3) the noise observed is significantly low compared to the non-interacting carriers diffusing in vacuum. A simple criterion for guiding the experimental measurements to detect the noise from carrier dynamics cannot be given. Multiple scenarios are possible as shown in Figs. (3.4), and (3.5) based on the interplay between charge carrier dynmaics, and dielectric relaxation. In the case of slow dielectric relaxation in Fig. (3.4), the charge carrier effects are seen at all frequencies, while in Fig. (3.5) the voltage noise spectrum from non-zero charge carrier densities resembles that from dielectric with no charge carrier at high frequencies. Moreover, the parameters used also change the characteristic frequencies $f_1, f_2$ and$f_3$; as each one of these frequencies crosses the measurement window at 1 Hz, the predicted results change. The electrodynamic treatment in Sec. 3.2.1

for a semi-infinite dielectric slab with charge transport and interactions is not applicable directly to the transistor geometry in its current form. The calculations from the electrodynamic model only provide a qualitative understanding of the effects of the dielectric fluctuations, carrier dynamics, and carrier transport on the measurement, either when present individually or when coupled nonlinearly together as in the semi-infinite slab calculation. In Chapter 4, efforts are made in two directions: 1) providing a quantitative comparison to the measured data on organic transistors, and 2) guiding the experiment to see the charge carrier effects.

## 3.4 Summary

The measurable power spectrum of cantilever frequency fluctuations in EFM over a semiconductor with mobile charge carriers is calculated from Maxwell's equations. Here, the current in Maxwell's equations has contributions from two terms: Ohm's law term that includes inter-carrier interactions, and a Fick's law term that includes thermal fluctuations of carrier density. Two parameters, diffusion coefficient ($D$), and conductivity ($\sigma_0$), are introduced through these two terms. These parameters may be expressed in terms of carrier density, temperature, and molecular properties; the diffusion constant and the conductivity would need to be expressed as functions of frequency and wavevector in order to incorporate a full microscopic description of charge transport into our macroscopic model.

For the case of no molecular motions, i.e. when the dielectric function is set to unity, the sample is comprised of interacting charge carriers diffusing in vac-

uum. When the dilute charge carrier limit is taken the result is the same as that from noninteracting diffusing carriers. The voltage noise calculated for interacting carriers in vacuum in the high frequency limit, agrees with the voltage noise calculated from noninteracting diffusing carriers, and in the low frequency limit is significantly suppressed due to intercarrier interactions. When the dielectric function is included as a complex-valued function of frequency, the noise is enhanced, suppressed, or unchanged relative to the noise from dielectric with no charge carriers, depending on the form of the dielectric function, and the frequency range of interest. The dominant contribution to frequency jitter is from the autocorrelation function of the gradient of electric field fluctuations yet again, similar to the thin-film organic polymer in Chapter 2 [20, 21]. The frequency jitter, in the large tip-sample separation limit, may be calculated by inserting the effective relative dielectric function of the medium that includes conductivity from Ohm's law term into the relative dielectric function in the frequency jitter result for a dielectric continuum. In this limit, the Ohm's law term in the current dominates the term with thermal fluctuation in carrier density. This large tip-sample separation limit is also observed in the calculation of the thermal Casimir-Lifshitz force between macroscopic bodies [14, 44].

The cantilever frequency noise calculated from a free diffusion model overestimates the measured noise by atleast two orders of magnitude, indicating the importance of including Coulomb interactions in such microscopic charge transport models. A theoretical framework that includes intercarrier interactions in the calculation of electrical noise of molecular materials has been presented. The electrodynamic model shown in this chapter qualitatively explains the effects of dielectric fluctuations, carrier dynamics, and interactions on noise measurements of semiconductors. The observed noise over a TPD transistor

was not quantitatively compared to the calculated noise from the model. This is because the model treats the sample as a semi-infinite semiconductor, while in the organic transistor sample the carriers are only confined to a few nm-thick region at the semiconductor-dielectric interface. In Chapter 4, two models are developed to improve our theoretical description of charge fluctuations in the TPD transistor, and the calculated noise from these models is studied to explore the effect of finite thickness of the semiconductor, and the effect of a dielectric overlayer. Further, quantitative comparison to observed noise on TPD transistor is given and noncontact friction predictions for the transistor are provided. The noncontact friction calculated from the semi-infinite semiconductor model in this chapter is compared to the friction data of doped Si [57].

# CHAPTER 4

# QUANTITATIVE COMPARISON TO MEASURED DATA ON AN ORGANIC FIELD-EFFECT TRANSISTOR AND DOPED SILICON

This chapter presents quantitative comparison of the model calculations to EFM measurements for two sets of data. The two sets of experimental data are the frequency jitter measured on a TPD transistor [20, 32], and the noncontact friction measured on doped Si [56, 57]. The main focus is on developing a model that explains the carrier density independence of frequency jitter measurements on organic transistors in Sec. 3.3. Models I and II, developed in this chapter, are an extension of the semi-infinite semiconductor model in Chapter 3, to include the possible effects of the finite thickness of the semiconductor on a dielectric base, and the confinement of charge carriers to few monolayers at the semiconductor-$SiO_2$ interface where essentially the rest of the semiconductor acts as a dielectric overlayer in the organic transistor in Fig. (3.8). Model I in Fig. (4.1) is developed to study the finite thickness effects of the semiconductor on a $SiO_2$ dielectric base. The effect of the $SiO_2$ dielectric base, and the finite thickness effect for a semiconductor of thickness 70 nm is found to be negligible on the cantilever frequency noise upon extension from the semi-infinite semiconductor model in Chapter 3. The calculations from model I are shown in Sec. 4.3.1. Model I goes to the semi-infinite semiconductor model in Sec. 3.1.1 when the finite thickness of the semiconductor slab on the $SiO_2$ dielectric goes to infinity. Model II is developed to include the confinement of the charge carriers to few monolayers at the semiconductor-$SiO_2$ interface [29, 49]. As a result the picture of model II has a dielectric overlayer of finite thickness over a semi-infinite semiconductor as an approximation to the organic transistor as shown in Fig. (4.2). Model II goes to the semi-infinite semiconductor model in Sec. 3.1.1 when the finite thickness

of the dielectric overlayer on the semi-infinite semiconductor goes to infinity. The calculations from this model are presented in Sec. 4.3.1, and these explain the carrier density independence of frequency jitter on organic transistor. These calculations also show that the carrier dynamics is seen at the frequencies accessible in a noncontact friction measurement. Ryan Dwyer in Professor John Marohn's group is working on measuring the noncontact friction measurements on organic field-effect transistor. The noncontact friction calculations shown in Sec. 4.3.2 are predictions for these organic transistor measurements. The measured noncontact friction data by Stowe, et.al. [57, 56] on doped Si samples for the parallel motion of the cantilever is quatitatively compared to the friction calculations from semi-infinite semiconductor model. The friction calculations show the $\rho^{-1/2}$ dependence observed on doped Si, when all the experimental parameters in Stowe measurement are used. The measured friction is fit with dispersion of Si as the sole adjustable parameter. The distance dependence of the friction from calculations, and measurements are compared, but observed to be not in agreement owing to the simplified tip-sample capacitance used in these calculations. Overall, the semi-infinite semiconductor model presents a reasonable picture for the noncontact friction measured on doped Si, explaining the experimental observation of the suppression of friction with increasing carrier density, as arising from the inter-carrier interactions and the dielectric fluctuations in doped Si.

## 4.1 Model I

The model of a semi-infinite semiconductor in Chapter 3 is extended to a model having a layer of semiconductor on a semi-infinite dielectric base as in Fig. (4.1).

The field equations in vacuum are given by Eqs. (2.9)-(2.11), with $A_{\mathrm{rxn}}$ as the unknown constant to be determined. Here, $z > 0$ is vacuum, and the semiconductor layer of thickness $h_{\mathrm{s}}$ is for $-h_{\mathrm{s}} < z < 0$ with a relative dielectric function $\epsilon_s(\omega)$. The semiconductor layer is backed by a dielectric base for $z < -h_{\mathrm{s}}$ with the relative dielectric function $\epsilon_{\mathrm{d}}(\omega)$. The fields in the semiconductor layer in $-h_{\mathrm{s}} < z < 0$ are given by,

$$\hat{E}_x = A_{++}e^{\eta_+ z} + A_{+-}e^{-\eta_+ z} + A_{-+}e^{\eta_- z} + A_{--}e^{-\eta_- z}, \tag{4.1}$$

$$\hat{E}_z = \frac{i\eta_+}{k}(A_{++}e^{\eta_+ z} - A_{+-}e^{-\eta_+ z}) + \frac{ik}{\eta_-}(A_{-+}e^{\eta_- z} + A_{--}e^{-\eta_- z}), \tag{4.2}$$

$$\hat{H}_y = \frac{-i\tilde{s}^2}{\omega\mu_0\eta_-}(A_{-+}e^{\eta_- z} - A_{--}e^{\eta_- z}), \tag{4.3}$$

with same definitions for the variables, $\tilde{s}$, $\eta_+$, $\eta_-$, $\epsilon_{\mathrm{eff}}$, and $\kappa$ as in Sec. (3.1.1), where $\epsilon_{\mathrm{rel}} \to \epsilon_{\mathrm{s}}$. The fields in the dielectric base for $z < -h_{\mathrm{s}}$ are given by

$$\hat{E}_x = Ce^{\eta z}, \tag{4.4}$$

$$\hat{E}_z = \frac{ik}{\eta}Ce^{\eta z}, \tag{4.5}$$

$$\hat{H}_y = \frac{-i\omega\epsilon_d(\omega)}{\mu_0\eta c^2}Ce^{\eta z}, \tag{4.6}$$

$$\eta = \sqrt{k^2 - \epsilon_d(\omega)(\omega/c)^2}. \tag{4.7}$$

These field equations are solved using the continuity conditions for $E_x$, $H_y$ and $\epsilon(\omega)E_z$ at both interfaces: 1) vacuum-semiconductor interface at $z = 0$, and 2) semiconductor-dielectric base interface at $z = -h_{\mathrm{s}}$ (see B appendix to chapter 4). $A_{\mathrm{rxn}}$ is thus determined to be

$$A_{\mathrm{rxn}} = -\frac{q(z_1,\omega)}{2\epsilon_0}e^{-\tilde{k}z_1}\left(\frac{\epsilon_{\mathrm{s}}(\omega) - \theta_{\mathrm{I}}(k,\omega)}{\epsilon_{\mathrm{s}}(\omega) + \theta_{\mathrm{I}}(k,\omega)}\right), \tag{4.8}$$

$$\theta_{\mathrm{I}} \equiv \frac{\epsilon_{\mathrm{s}}(\omega)}{\epsilon_{\mathrm{eff}}(\omega)}\left[\frac{\sinh kh_{\mathrm{s}}\sinh\eta_+h_{\mathrm{s}} + \alpha\cosh kh_{\mathrm{s}}\sinh\eta_+h_{\mathrm{s}} + \lambda - \lambda\cosh\eta_+h_{\mathrm{s}}\cosh kh_{\mathrm{s}}}{\cosh kh_{\mathrm{s}}\sinh\eta_+h_{\mathrm{s}} + \alpha\sinh kh_{\mathrm{s}}\sinh\eta_+h_{\mathrm{s}} - \lambda\cosh\eta_+h_{\mathrm{s}}\sinh kh_{\mathrm{s}}}\right.$$
$$-\lambda\coth\eta_+h_{\mathrm{s}}$$
$$\left.+\frac{\lambda}{\sinh\eta_+h_{\mathrm{s}}}\left(\frac{\sinh\eta_+h_{\mathrm{s}} - \lambda\sinh kh_{\mathrm{s}}}{\cosh kh_{\mathrm{s}}\sinh\eta_+h_{\mathrm{s}} + \alpha\sinh kh_{\mathrm{s}}\sinh\eta_+h_{\mathrm{s}} - \lambda\cosh\eta_+h_{\mathrm{s}}\sinh kh_{\mathrm{s}}}\right)\right] \tag{4.9}$$

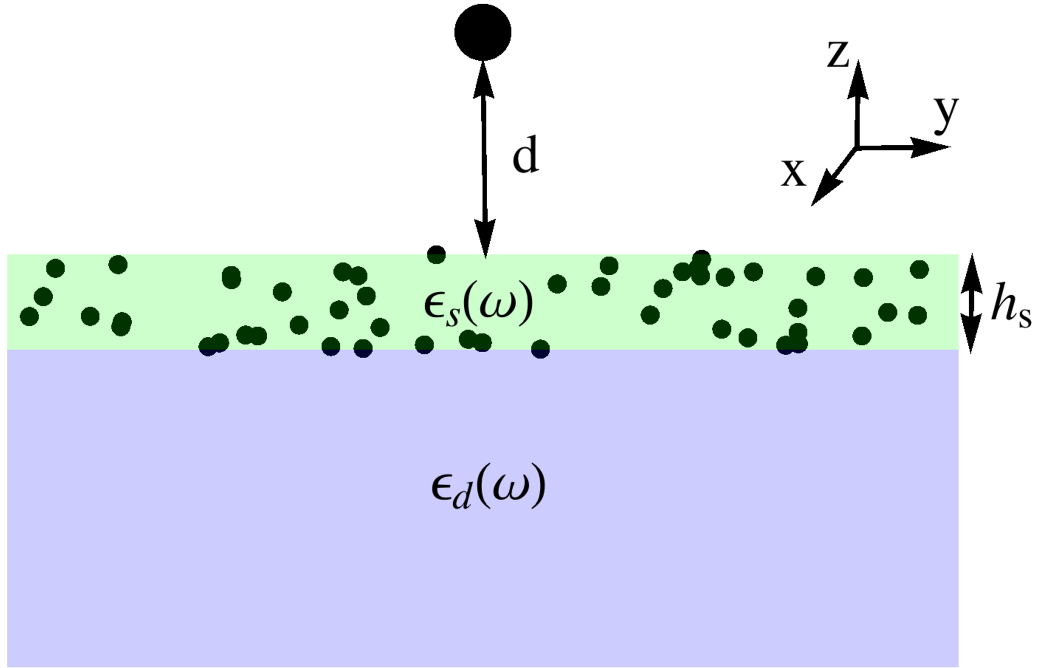


Figure 4.1: A sketch of model I where a point charge is located at a tip-sample separation $d$. The point charge here represents the cantilever tip. The sample is represented by a semiconductor layer of thickness $h_s$ on a semi-infinite dielectric base. The relative dielectric function of the semiconductor is $\epsilon_s(\omega)$, and that of the base is $\epsilon_d(\omega)$.

$$\lambda \equiv \left(1 - \frac{\epsilon_{\text{eff}}(\omega)}{\epsilon_s(\omega)}\right)\frac{k}{\eta_+}, \qquad \alpha \equiv \frac{\epsilon_{\text{eff}}}{\epsilon_d}. \tag{4.10}$$

Using $A_{\text{rxn}}$ in Eq. (4.8), similar steps from Eqs. (2.20)-(2.22) are followed to determine the potential autocorrelation function $C_{\delta\phi\,\delta\phi}(\mathbf{r}_1 = \mathbf{0}, z_1, \mathbf{r}_2 = \mathbf{0}, z_2; f)$ as follows.

$$C_{\delta\phi\,\delta\phi}(\mathbf{r}_1 = \mathbf{0}, z_1, \mathbf{r}_2 = \mathbf{0}, z_2; f) = -\frac{k_B T}{4\pi\epsilon_0\omega}\text{Im}\int_0^\infty \text{dk}e^{-\text{k}(z_1+z_2)}\left(\frac{\epsilon_s(\omega) - \theta_I}{\epsilon_s(\omega) + \theta_I}\right) \tag{4.11}$$

The power spectrum is determined from Eq. (1.30) and the noncontact friction is determined from Eqs. (1.23), and (1.26). This model of finite thickness ($h_s$) for the semiconductor with uniformly distributed charge carriers over a dielectric base as in Fig. (4.1), is an approximation to the transistor geometry in Fig.

(3.8). The organic transistor has the charges confined to few monolayers in the semiconductor close to the semiconductor-dielectric base interface. This physical feature is included in model II in the following section. Sec. (4.3) shows the calculations from this model, and the effect of varying thickness $h_s$ of the semiconductor on the noise is analyzed.

## 4.2 Model II

This model is developed to study the effect of screening the noise from a semiconductor with charge carriers by a dielectric overlayer as in Fig. (4.2). This is an approximation to the transistor geometry where the charge carriers are known to be confined to few monlayers [29, 49] at the semiconductor-$SiO_2$ interface in Fig. (3.8). Here, $z > 0$ is vacuum, a dielectric overlayer with dielectric function $\epsilon_d(\omega)$ is for $-h_d < z < 0$ and, a semiconductor with a dielectric function $\epsilon_s(\omega)$ extends for $z < -h_d$. The field equations in vacuum are given by Eqs. (3.15)-(3.17), and $A_{rxn}$ as the unknown constant to be determined. The field equations in the dielectric overlayer for $-h_d < z < 0$ are given by Eqs. (2.12)-(2.14), and the field equations in the semiconductor for $z < -h_d$ are given by Eqs. (3.15)-(3.17). These equations are solved using the continuity conditions (see B appendix to chapter 4) for $E_x$, $H_y$ and $\epsilon(\omega)E_z$ at both interfaces: 1) vacuum-dielectric overlayer interface at $z = 0$, and 2) dielectric overlayer-semiconductor interface at $z = -h_d$. $A_{rxn}$ is thus determined to be,

$$A_{rxn} = -\frac{q(z_1,\omega)}{2\epsilon_0} e^{-\tilde{k}z_1} \left( \frac{\epsilon_s(\omega) - \theta_{II}(k,\omega)}{\epsilon_s(\omega) + \theta_{II}(k,\omega)} \right), \tag{4.12}$$

$$\theta_{II} \equiv \frac{\epsilon_s(\omega)}{\epsilon_d(\omega)} \left( \frac{\sinh kh_d + (1-\lambda)\frac{\epsilon_d(\omega)}{\epsilon_{eff}(\omega)} \cosh kh_d}{\cosh kh_d + (1-\lambda)\frac{\epsilon_d(\omega)}{\epsilon_{eff}(\omega)} \sinh kh_d} \right). \tag{4.13}$$

The variables $\lambda$, $\epsilon_{eff}$ and $\eta_+$ are as defined in Eqs. (4.10), (3.7) and (3.12) with

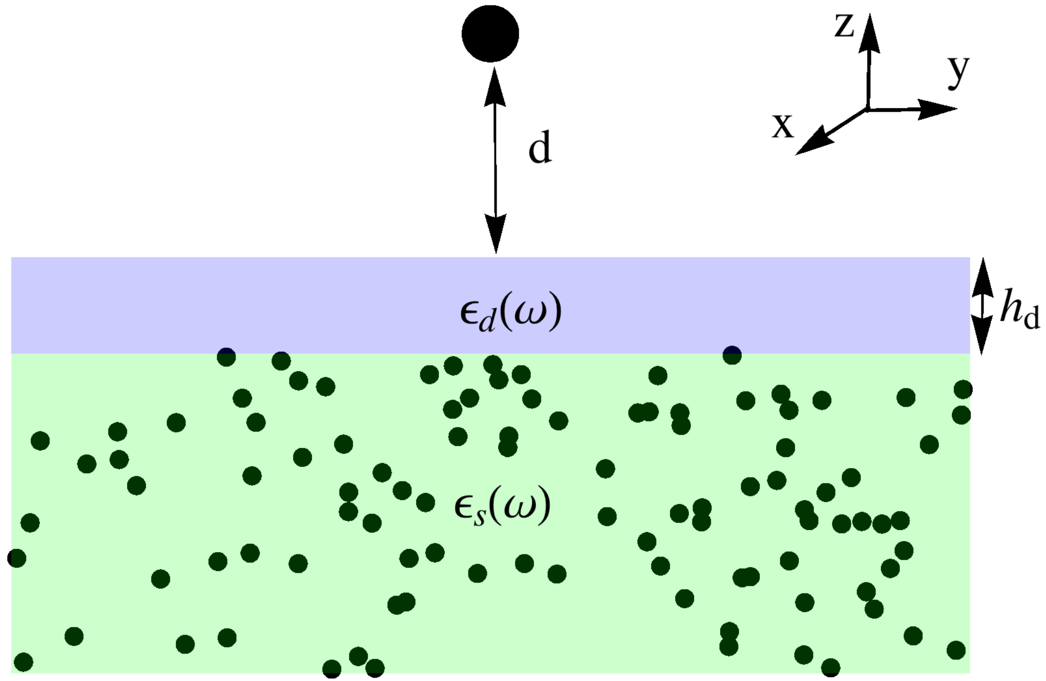


Figure 4.2: A sketch of model II where a point charge is located at a tip-sample separation $d$. The point charge in the model is at the locaton of the cantilvere tip in EFM. The sample is represented by a dielectric overlayer of thickness $h_\mathrm{d}$ on a semi-infinite semiconductor. The relative dielectric function of the semiconductor is $\epsilon_\mathrm{s}(\omega)$, and that of the dielectric overlayer is $\epsilon_\mathrm{d}(\omega)$.

$\epsilon_\mathrm{rel} \rightarrow \epsilon_\mathrm{s}$, respectively. Similar steps from Eqs. (2.20)-(2.22) are followed to determine the potential autocorrelation function from $A_\mathrm{rxn}$ in Eq. (4.12) as

$$C_{\delta\phi\,\delta\phi}(\mathbf{r}_1 = \mathbf{0}, z_1, \mathbf{r}_2 = \mathbf{0}, z_2; f) = -\frac{k_B T}{4\pi\epsilon_0\omega}\mathrm{Im}\int_0^\infty \mathrm{dk}\mathrm{e}^{-\mathrm{k}(\mathrm{z}_1+\mathrm{z}_2)}\left(\frac{\epsilon_\mathrm{s}(\omega) - \theta_\mathrm{II}}{\epsilon_\mathrm{s}(\omega) + \theta_\mathrm{II}}\right) \tag{4.14}$$

The power spectrum of frequency fluctuations is determined from Eq. (1.30), and the noncontact friction is determined from Eqs. (1.23), and (1.26). Sec. 4.3 shows the calculations from this model for different thicknesses $h_\mathrm{d}$ of the dielectric overlayer.

## 4.3 Results and discussion

### 4.3.1 Frequency Jitter

Figure (4.3a) shows the power spectrum of frequency fluctuations $P^{\perp}_{\delta f_c}(f)$ versus frequency from model I in Sec. 4.1 for the perpendicular motion of the cantilever. The potential auto-correlation determined from Sec. 4.1 is used in the calculation of the power spectrum of cantilever frequency fluctuations from Eqs. (1.27), and (1.30). An approximate simplified expression for the tip-sample capacitance Eq. (3.38), of a sphere charge of radius $R$ at a height $z$ above the semi-infinite dielectric is used in Eq. (1.30). The capacitance equation uses $R$ = 40 nm, and dielectric constant $\epsilon'_{\mathrm{rel}}(0) = 4$ in Eq. (3.38), for all the power spectra, and the frequency jitter calculations from models I and II in this chapter. The cantilever resonance frequency, the force constant, and the tip-sample voltage are given values: $f_c$ = 65 kHz and $k_c$ = 3.5 N/m and $V_{\mathrm{ts}}$ = 3 V, respectively. These values are corresponding to the organic transistor meaurements in Ref. [32], and used for all the power spectrum, and jitter calculations in this chapter. The tip-sample distance is $d$ = 100 nm, and the thickness of the semiconductor layer is $h_{\mathrm{s}}$ = 70 nm. A carrier mobility corresponding to that of the organic transistor $\mu = 2.7 \times 10^{-10}\ \mathrm{m^2V^{-1}s^{-1}}$ from Ref. [32] is used, and the diffusion constant is estimated from the Einstein relation, $D = 7.0 \times 10^{-12}\ \mathrm{m^2V^{-1}s^{-1}}$. The dielectric functions in this chapter are taken to be independent of frequency to focus on the effects of charge carrier dynamics in the dielectric in the absence of dielectric relaxation. The effects of molecular motion in the dielectric coupled to the carrier dynamics have been studied for a semi-infinite semiconductor in Chapter 3. The dielectric function of the semiconductor layer is assigned an arbitrary value

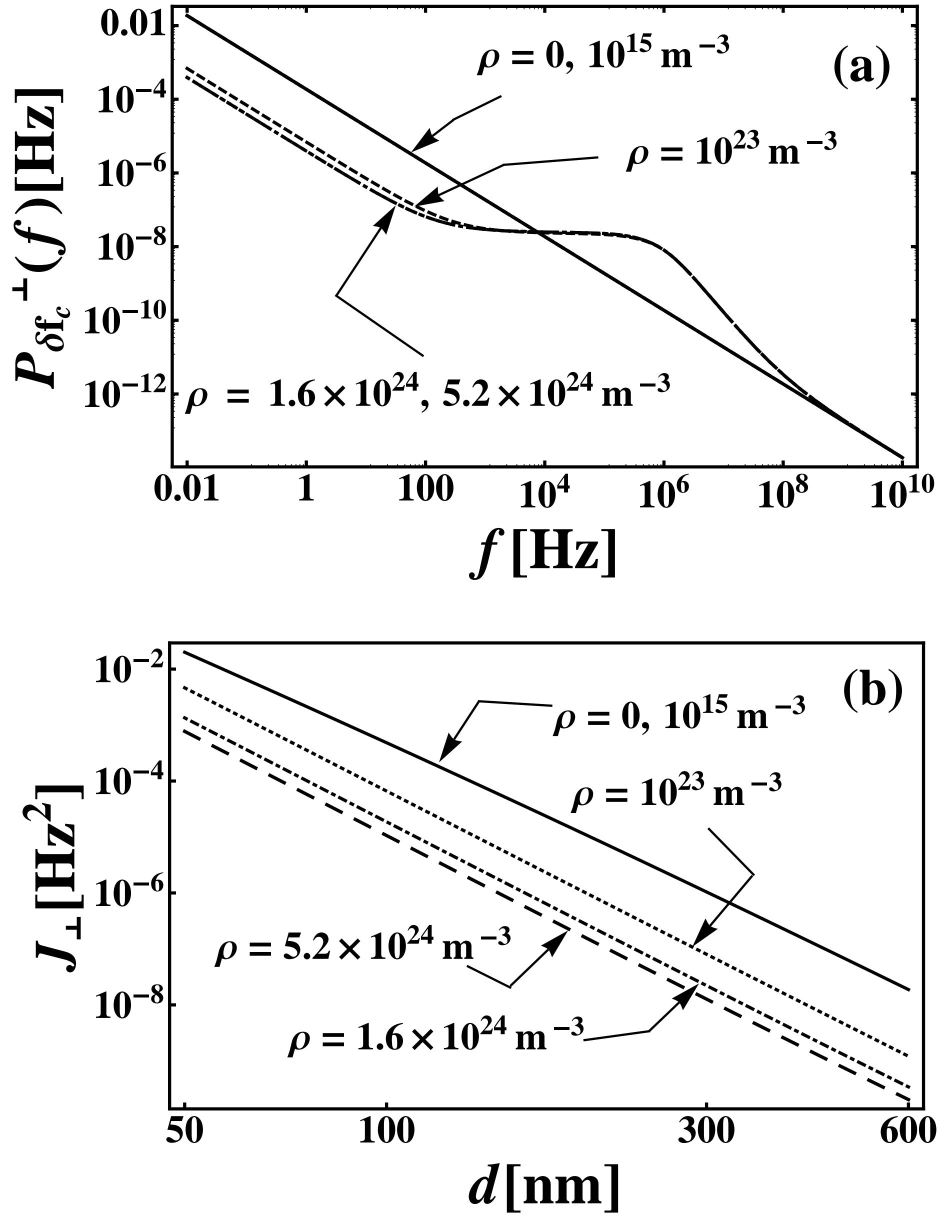


Figure 4.3: (a) Power spectrum of frequency fluctuations vs. frequency at a tip-sample height of $d$ = 100 nm calculated from model I for different carrier densities. (b) Integrated cantilever frequency jitter for different charge densities. Following parameters were used in the calculations from model I in (a) and (b): semiconductor thickness $h_s$ = 70 nm, carrier mobility $\mu$ = $2.7 \times 10^{-10}$ $m^2V^{-1}s^{-1}$, semiconductor dielectric function $\epsilon_{rel} = 3.4 - i\,0.05$, dielectric constant of $SiO_2$ base $\epsilon_d = 4.85$, tip-radius $R$ = 40 nm, cantilever resonance frequency $f_c$ = 65 kHz, and tip-sample voltage $V_{ts}$ = 3 V.

$\epsilon_s = 3.4 - i\ 0.05$, and a static dielectric constant of $SiO_2$ $\epsilon_d = 4.85$ is used for the dielectric base. This is reasonable as model I in Fig. (4.1) is a simplified version of the organic transistor in Fig. (3.8). The thickness of the organic semiconductor layer with uniform carrier density in model I corresponds to the thickness of the molecularly doped polymer whose dielectric function is unknown in organic transistor in Fig. (3.8), while the semi-infinite dielectric base in the model corresponds to $SiO_2$ layer in organic transistor in Fig. (3.8) . The power spectrum is plotted for a wide range of frequencies to analyze fully the predictions from model I. The experimentally accessible frequencies range from tenths of Hz to 100 Hz.

In Fig. (4.3a), for a zero carrier density in the semiconductor layer of model I, $P_{\delta f_c}(f) \propto f^{-1}$, when a frequency-independent dielectric function is used in the calculation. Increasing the carrier density to $\rho = 10^{15}$ m$^{-3}$ gives a power spectrum that is same as that for zero carrier density. The three high carrier densities corresponding to that estimated from three gate voltages $V_G = 0, -20, -40$ V are shown in Fig. (4.3a). As described in Sec. 3.3, the areal carrier density from $V_G$ is estimated as follows: $\rho_A = C_i(|V_t - V_G|)/e = 3.0 \times 10^{16}\text{m}^{-2}$, with $C_i = 1.3 \times 10^{-4}$ Fm$^{-2}$, $V_G = -40$ V, and $V_t = -2.9$ V. The three dimensional carrier density is estimated from the areal carrier density using the relation, $\rho = \rho_A^{3/2}$. In this chapter, total carrier density $\rho \equiv 2\bar{\rho}$ is shown instead of the carrier density ($\bar{\rho}$) for positively or negatively charged carriers shown in Chapter 3. Thus, the three dimensional carrier densities corresponding to $V_G = -40, -20, 0$ V are $\rho = 5.2{\times}10^{24}, 1.6{\times}10^{24}, 1{\times}10^{23}\text{m}^{-3}$, respectively. In the asymptotic high frequency limit, the power spectrum of frequency fluctuations for these high carrier densities is same as the dielectric with no charge carriers, and no effects from carrier dynamics are seen in this limit in Fig. (4.3a). A decrease in frequency from the

asymptotic high-$f$ regime results in increase of spectral noise. This regime corresponds to the non-interacting carrier diffusion. Further decrease in frequency leads to a plateau region in the power spectrum for these three carrier densities. In this regime, the Coulomb interactions are significant but the dielectric response of the medium is negligible. In the asymptotic low-$f$ limit, there is suppression in frequency noise with increase in carrier density. In this regime, both Coulomb interactions, and the dielectric response of the medium contribute, and these inter-carrier interactions contribute to the suppression in frequency noise observed in the Fig. (4.3a). This analysis is the same as the interpretation provided in detail for the spectral noise from a semi-infinite semiconductor with varying carrier densities in Fig. (3.3) of Sec. 3.2 [32]. Figure (4.3b) shows the integrated frequency jitter calculated from Eq. (1.28) for the power spectrum in Fig. (4.3a), with $f_{\min} = 0.2$ Hz, and $f_{\max} = 3$ Hz. This is the frequency range of measurements on organic transistor in Sec. 3.3. For this frequency range, Fig. (4.3a) shows suppression in the power spectrum of frequency fluctuations with increase in charge density due to inter-carrier interactions. The integrated power spectrum shows the same behaviour, that is, the magnitude of frequency jitter $J_{\perp}$ decreases with increase in $\rho$.

The effects of finite thickness of the semiconductor layer on the cantilever frequency noise are not visible for a thickness of $h_{\mathrm{s}} = 70$ nm shown in Fig. (4.3a). Figure (4.4) shows the power spectrum of frequency fluctuations $P^{\perp}_{\delta f_c}(f)$ for different thicknesses ($h_{\mathrm{s}}$) of the semiconductor layer on the dielectric base $SiO_2$ as a function of frequency. The carrier density is $\rho = 5.2 \times 10^{24}$ m$^{-3}$, the tip-sample height is $d = 100$ nm, and the rest of the parameters are the same as that in the calculation of Fig. (4.3a). The power spectrum of frequency fluctuations is the same as that from the semi-infinite semiconductor result in Sec. 3.2, for thick-

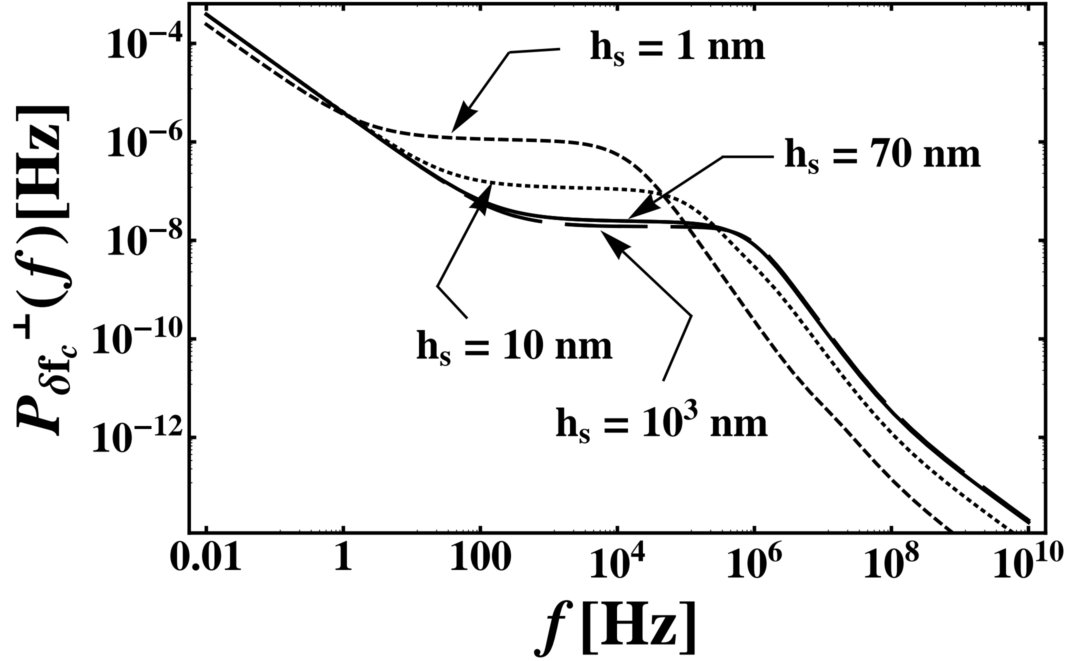


Figure 4.4: The power spectrum of frequency fluctuations vs. frequency at a tip-sample height of $d = 100$ nm from model I for different thicknesses $h_s$ of the semiconductor layer. The carrier density corresponds to a gate voltage of −40 V, $\rho = 5.2 \times 10^{24}$ m$^{-3}$. All the other parameters are the same as listed for Fig. (4.3a).

nesses $h_s = 70$ nm and $h_s = 1$ $\mu$m in Fig. (4.4). The thickness effects are significant when the semiconductor is only few monolayers thick over the $SiO_2$ dielectric base, as seen from the power spectrum calculations for $h_s = 10$ nm and $h_s = 1$ nm in Fig. (4.4). Since the thickness of the molecularly doped organic polymer in organic transistor used for the EFM measurements is $h_s \approx 70$ nm, the calculations from model I for organic transistor suggest that the frequency noise is indistinguishable from $h_s \to \infty$ (the semi-infinite semiconductor case), when model I is used. In account of no thickness effect from semiconductor, and the fact that charge carriers are only confined to a few monolayers in the semiconductor at the interface of semiconductor-dielectric base, another approximate model of organic transistor, model II as shown in Fig. (4.2) is designed.

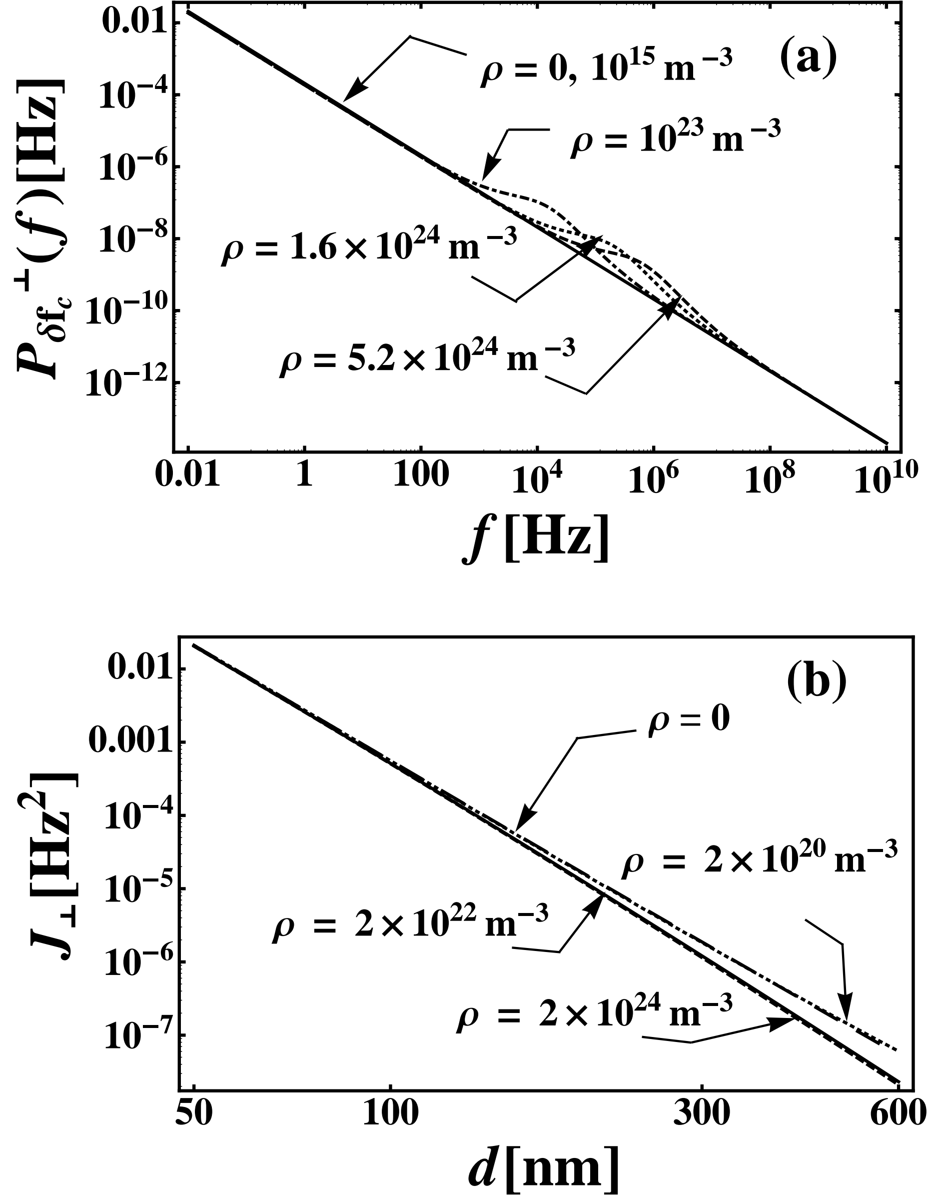


Figure 4.5: (a) The power spectrum of cantilever frequency fluctuations vs. frequency at tip-sample height of $d$ = 100 nm shown for model II for different charge carrier densities. (b) Integrated cantilever frequency jitter for different charge densities. The following parameters were used in the calculations from model II in (a), and (b): the thickness of the dielectric overlayer is $h_{\mathrm{d}}$ = 69 nm, the dielectric function of the dielectric and the semiconductor are taken to be $\epsilon_{\mathrm{rel}} = \epsilon_{\mathrm{d}} = 3.5 - i\,0.05$, and the rest of the parameters are the same as in Fig. (4.3a).

Model II consists of a dielectric overlayer of thickness $h_{\rm d}$ on a semi-infinite semiconductor as shown in Fig. (4.2). The calculations of the power spectrum and the frequency jitter for model II are shown in Figs. (4.5)-(4.7). Figure (4.5) is the power spectrum of frequency fluctuations calculated from potential autocorrelation determined for model II in Sec. 4.2, using Eqs. (1.27) and (1.30). The thickness of the dielectric overlayer is $h_{\rm d} = 69$ nm. This is obtained from the transistor configuration in Fig. (3.8), where the polymer thickness is 70 nm, and the charge carriers are assumed to be confined to a thickness of 1 nm at the semiconductor-$SiO_2$ interface. The dielectric function of the dielectric overlayer and the semiconductor are taken as $\epsilon_{\rm rel} = \epsilon_{\rm d} = 3.4 - i\ 0.05$. The carrier mobilty, the diffusion constant, and the other cantilever constants are same as that used for the calculation of Fig. (4.3a). Similar frequency regimes for the power spectrum to those observed in Fig. (4.3a) are seen in Fig. (4.5a). The only notable difference is seen in the asymptotic low-$f$ region. For high carrier densities, Fig. (4.3a) showed a significant suppression in noise from Coulomb interactions between charge carriers. This suppression in power spectrum of frequency fluctuations is not observed for the calculations from model II where a dielectric overlayer of thickness $h_{\rm d} = 69$ nm is added on the semiconductor, and the $P_{\delta f_c}^{\perp}$ thus calculated in Fig. (4.5a) is nearly independent of charge carrier density in the asymptotic low-$f$ region. The dielectric overlayer screens the noise from the semi-infinite semiconductor, and so no suppression in noise is seen in Fig. (4.5a). The unexplained feature in Chapter 3 in the experimental measurements on organic transistor discussed in Sec. 3.3 is that there is no effect of increasing the gate voltage of the organic transistor on the cantilever frequency noise. The increase in gate voltage is known to increase the carrier density in semiconductor for transistors. The model with dielectric overlayer of thickness $h_{\rm d} = 69$ nm on

the semiconductor reproduces the independence of cantilever frequency noise on carrier density. Figure (4.5b) is the frequency jitter from model II calculated similarly to that in Fig. (4.3b) for model I. As seen in Fig. (4.5b), the increase in charge density from $10^{22}$ to $10^{24}$ m$^{-3}$ does not change the frequency jitter much when compared to the significant supression in noise observed in Fig. (4.3b) for these charge densities in the absence of the dielectric overlayer.

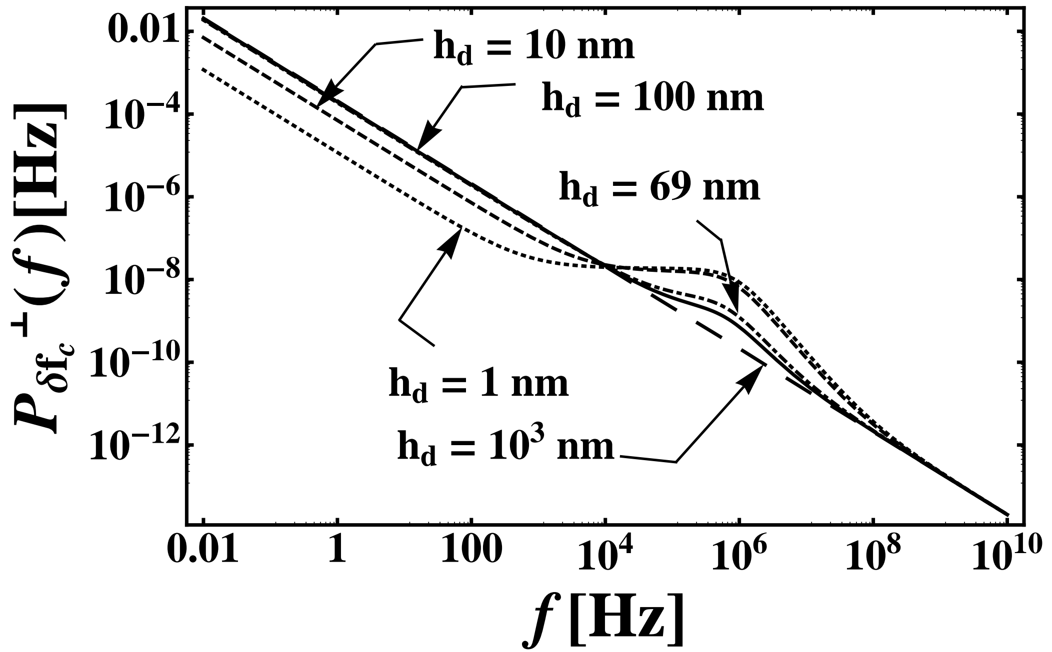


Figure 4.6: The power spectrum of cantilever frequency fluctuations vs. frequency at a tip-sample height of $d$ = 100 nm from model II for different thicknesses $h_{\mathrm{d}}$ of the dielectric overlayer. The carrier density is corresponding to a gate voltage of −40 V, $\rho$ = $5.2 \times 10^{24}$ m$^{-3}$. All the other parameters are the same as listed for Fig. (4.3a).

Figure (4.6) shows the power spectrum of frequency fluctuations $P^{\perp}_{\delta f_c}(f)$ for various thicknesses ($h_{\mathrm{d}}$) of the dielectric overlayer on a semi-infinite semiconductor. A carrier density of $\rho = 5.2 \times 10^{24}$ m$^{-3}$ is used here. For a thickness of $h_{\mathrm{d}} = 1\mu$m, $P^{\perp}_{\delta f_c}(f) \propto f^{-1}$, and is the same as that from a dielectric continuum. As

the thickness is decreased the carrier dynamic effects become prominent, and in the limit of $h_d \to 0$, the carrier dynamics effects similar to that observed from a semi-infinite semiconductor model in Chapter 3 for the same carrier density are observed in Fig. (4.6) as is expected for this limit. For the thicknesses of the dielectric overlayer applicable to the organic transistor $h_d = 69$ nm, the carrier dynamics are only seen at high frequencies that are not accessible in the jitter measurements which has frequency range, $f_{min} = 0.2$ Hz to $f_{max} = 3$ Hz. The cantilever frequency jitter calculations for this thickness show no dependence on carrier density consistent with the jitter measurements on organic transistor [32]. Figures (4.5), and (4.6) demonstrate that the carrier dynamics effects that are seen at high frequencies, are accessible in a noncontact friction measurement on organic transistor for these gate voltages.

Figure (4.7) shows the experimental jitter data for a gate voltage $V_G = -40$ V as solid dots. These jitter measurements are reported in Ref. [20, 32] and Sec. 3.3, for gate voltages $V_G = 0, -20, -40$ V of the organic transistor. The solid and the dashed lines in Fig. (4.7) are the jitter calculated for three charge densities $\rho = 5.2 \times 10^{24}, 1.6 \times 10^{24}, 10^{23}$ m$^{-3}$, and a dielectric function $\epsilon_d = \epsilon_s = 3.4 - i\epsilon''$. These three carrier densities are determined for gate voltages $V_G = -40, -20, 0$ V, respectively, as discussed earlier in the context of Fig. (4.3a). A carrier mobility of $\mu = 2.7 \times 10^{-10}$ m$^2$V$^{-1}$s$^{-1}$ estimated for charge carriers in organic transistor in Sec. 3.3 is used in the calculation of both the solid and dashed lines. $J_\perp$ is thus calculated from model II for thickness of the dielectric overlayer $h_d = 69$ nm from Eq. (1.28) with $f_{min} = 0.2$ Hz, and $f_{max} = 3$ Hz. For these three carrier densities corresponding to the gate voltages $V_G = -40, -20, 0$ V, $J_\perp$ is independent of carrier density, and all lie on the same solid line in Fig. (4.7). The magnitude of the jitter in experiment is reproduced in the calculations from

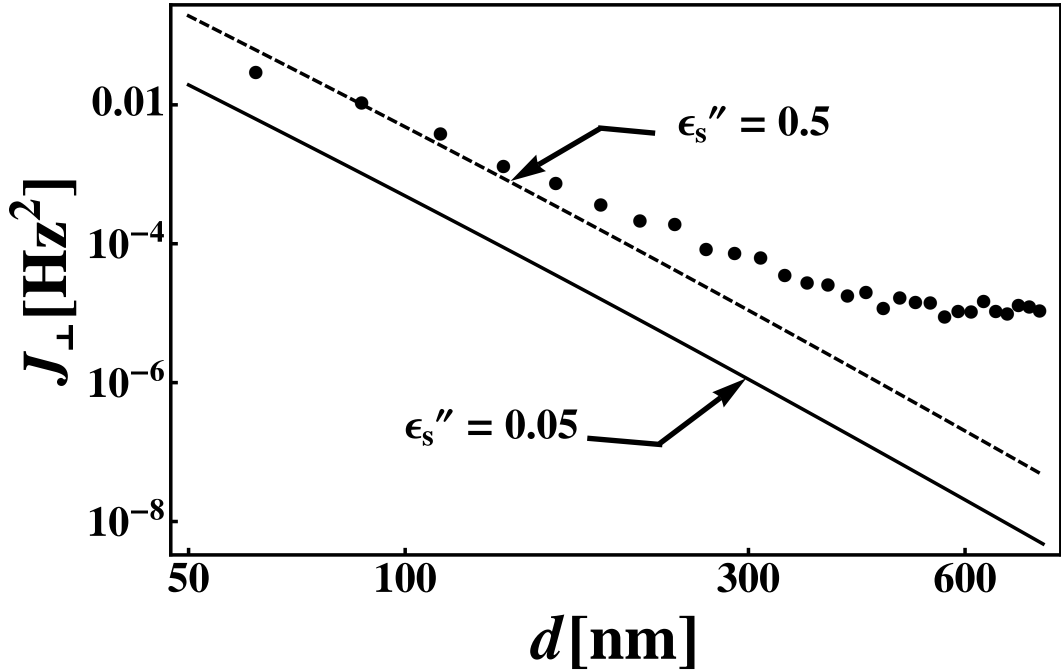


Figure 4.7: Measured cantilever frequency jitter $J_\perp$ for a gate voltage of $V_G = -40$ V in organic transistor shown as solid dots. The data for gate voltages $V_G = -20$ V, and $V_G = 0$ are indistinguishable from the solid dots, and are shown in Fig. (3.10), but not included here. The solid and the dashed lines are calculated from model II for a carrier density $\rho = 5.2 \times 10^{24}$ m$^{-3}$, corresponding to a gate voltage of $V_G = -40$ V. A relative dielectric function of $\epsilon_s = \epsilon_d = 3.4 - i\epsilon_s''$ with $\epsilon_s''$ as indictaed, is used in the calculation of these lines. The $J_\perp$ result from a different carrier density $\rho = 1.6 \times 10^{24}$ m$^{-3}$ corresponding to $V_G = -20$ V, is indistinguishable from these lines. The parameters used are relevant to the transistor measurements in Sec. 3.3: the dielectric overlayer has thickness $h_d = 69$ nm, the carrier mobility is $2.7 \times 10^{-10}$ m$^2$V$^{-1}$s$^{-1}$, and all the other parameters have the same values as in Fig. (4.3).

model II for a larger value of the dispersive part of the dielectric function. The calculation gives a stronger dependence on tip-sample separation compared to that measured in experiment, but the consistency is seen with the data in the independence of jitter on carrier density $\rho$. The disagreement of calculations with the experimental data in tip-sample height dependence may be attributed

to the oversimplified choice of the tip-sample capacitance from Eq. (3.38) in the calculation of $J_{\perp}$ from Eq. (1.30).

### 4.3.2 Noncontact friction

The models developed in Chapter 3 and in this chapter are useful in the calculation of the another experimental observable, noncontact friction. The noncontact friction measurements on doped Si are available from Ref. [57] for comparison with the calculations, while those on organic transistor are being done in Professor John Marohn's group. Stowe, et al. [57] have performed noncontact friction measurements using highly sensitive cantilever on n- and p-type silicon samples. These measurements are performed for the cantilever oscillating in parallel motion, as described in Sec. 1.1.1. Here, we provide a quantitative comparison between the noncontact friction measured on these samples, and the friction calculated from our semi-infinite semiconductor model in Sec. 3.1.1. The noncontact friction for parallel motion of the cantilever is calculated from Eqs. (1.23) and (1.24). In Eq. (1.24), the potential auto-correlation determined from Sec. 3.1.1 for a semi-infinite semiconductor is used because sample here is a doped Si. The noncontact friction, thus determined in terms of $\theta(k,\omega)$ (in Eq. (3.20) for $y \to kd$) for the parallel motion is

$$\gamma_{\parallel} = -\frac{q_c^2}{8\pi\epsilon_0\omega_c}\int_0^{\infty} dk k^2 e^{-2kd}\mathrm{Im}\left(\frac{\epsilon_{\mathrm{rel}}(\omega_c) - \theta(k,\omega_c)}{\epsilon_{\mathrm{rel}}(\omega_c) + \theta(k,\omega_c)}\right). \quad (4.15)$$

When $h_{\mathrm{s}} \to \infty$ in model I, and $h_{\mathrm{d}} \to 0$ in model II, these two models reduce to the semi-infinite semiconductor model in Sec. 3.1.1. The $\theta(k,\omega)$ for the semi-infinite semiconductor is also obtained by taking the limit $c \to \infty$ of Eq. (3.19), and setting $\epsilon_{\mathrm{rel}} = \epsilon_{\mathrm{s}}$. The calculations are shown for noncontact friction from this

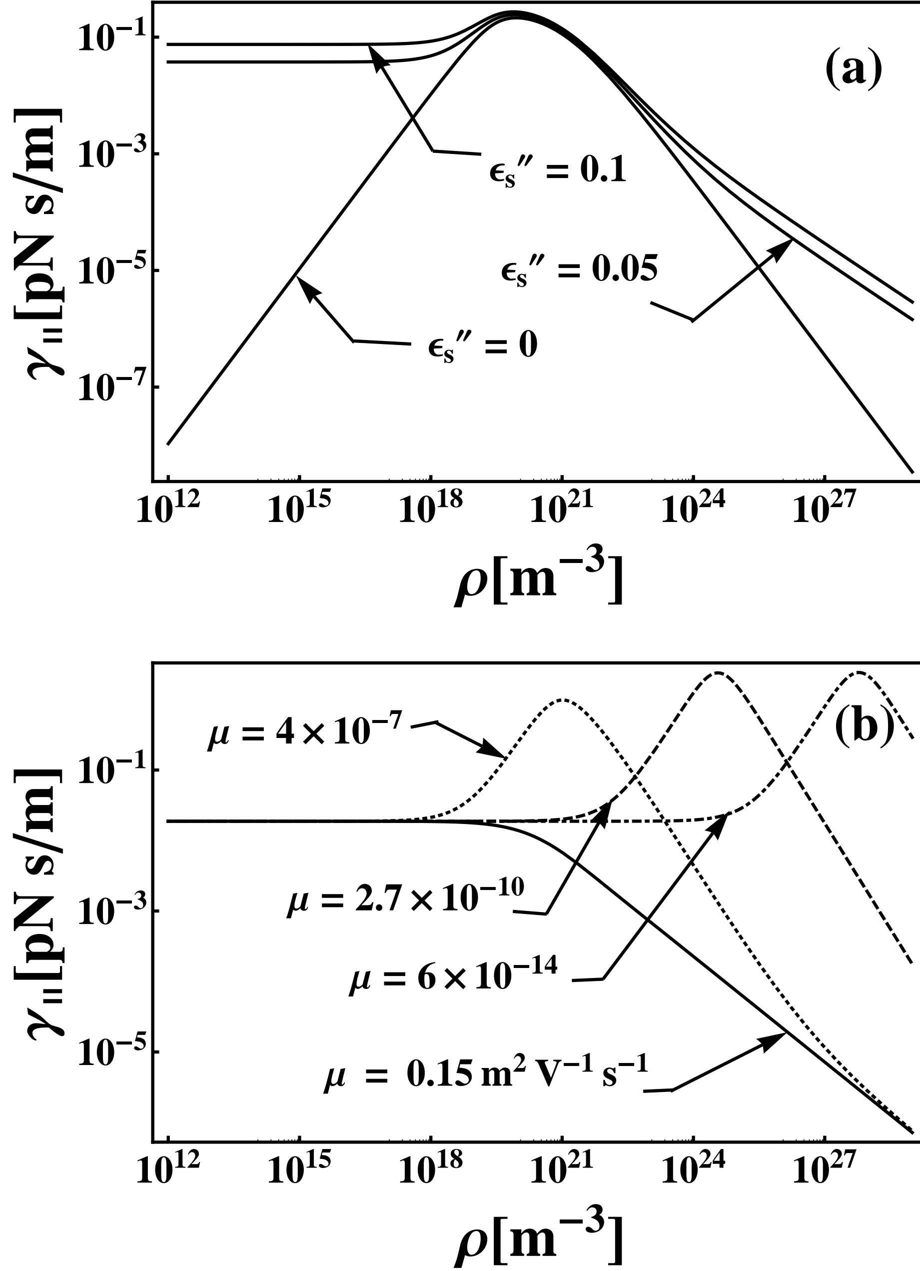


Figure 4.8: Noncontact friction for the parallel motion of the cantilever calculated from Eq. (4.15) for a semi-infinite seniconductor. (a) $\gamma_{\parallel}$ vs. carrier density for different values of dispersion $\epsilon_s''$ in the relative dielectric function of the semiconductor $\epsilon_{\mathrm{rel}} = 11.9 - i\,\epsilon_s''$. The carrier mobility is $\mu = 10^{-5}\ \mathrm{m^2V^{-1}s^{-1}}$ . (b) $\gamma_{\parallel}$ vs. carrier density for various mobility values are shown. The relative dielectric function $\epsilon_s = 3.4 - i\ 0.05$. In (a) and (b), the experimental constants are tip-sample radius $R = 80$ nm, cantilever frequency $f_c = 81$ kHz, and tip-sample voltage $V_{ts} = 3$ V.

semi-infinite semiconductor whose $\theta(k,\omega)$ is given by,

$$\theta(k,\omega) = \frac{\epsilon_{\mathrm{eff}}}{\epsilon_{\mathrm{s}}}\,(1-\lambda)\,, \tag{4.16}$$

where $\lambda$ is given by Eq. (4.10).

Figure (4.8a) shows the noncontact friction calculated from Eqs. (4.15) and (4.16). A tip-sample separation of $d = 300$ nm, and a dielectric function $\epsilon_{\mathrm{s}} = 11.9 - i\,\epsilon''$, are used in the calculation. The real part of $\epsilon_{\mathrm{s}}$ of the semiconductor is taken as the static dielectric constant of Si. The charge at the tip $q_c \equiv c(d)V_{\mathrm{ts}}$ in Eq. (4.15) is determined using the capacitance formula in Eq. (3.38) for $V_{\mathrm{ts}} = 3$ V. A tip-radius $R = 80$ nm and a relative dielectric function of Si $\epsilon_{\mathrm{s}}'(0) \equiv 11.9$, are used in the capacitance formula. All the noncontact friction calculations in this section use a cantilever resonance frequency $f_c = 81$ kHz, the value in Stowe's measurements [57]. A tip-sample voltage $V_{\mathrm{ts}} = 3$ V is used in Eq. (4.15) for Figs. (4.8a), and (4.8b). A mobility of $\mu = 10^{-5}\ \mathrm{m^2V^{-1}s^{-1}}$, and a diffusion constant estimated from Einstein relation for this mobility $D = 2.6 \times 10^{-7}\ \mathrm{m^2s^{-1}}$, are used in the calculation of Fig. (4.8a). Figure (4.8a) shows the noncontact friction calculated from Eq. (4.15) versus carrier density in semiconductor for different values of dispersion $\epsilon_{\mathrm{s}}''$ in the relative dielectric function $\epsilon_{\mathrm{s}} = 11.9 - i\,\epsilon_{\mathrm{s}}''$. The noncontact friction for parallel motion in the absence of dispersion ($\epsilon_{\mathrm{s}}'' = 0$) shows two regimes: 1) the low carrier density regime where the carrier density is sufficiently dilute, so inter-carrier interactions are negligible, and the friction increases linearly in $\bar{\rho}$, and 2) the high carrier density regime where the carrier density is high, the inter-carrier interactions result in suppression of friction, and $\gamma_{\|} \propto \bar{\rho}^{-1}$. A peak value for friction is attained in going from regime 1 to 2. For non-zero values of $\epsilon_{\mathrm{s}}''$, two additional carrier density regimes emerge with the peak approximately at the same carrier density, and the two regimes around the peak same as that for $\epsilon'' = 0$. Figure (4.8a) shows two additional regimes for

$\epsilon'' = 0.05$ and 0.1: 1) the asymptotic low carrier density limit where the friction is independent of carrier density, and is only from the dielectric fluctuations, and 2) the asymptotic high carrier density limit where the friction is $\propto \bar{\rho}^{-1/2}$, and the friction is both from dielectric fluctuations and inter-carrier interactions.

Figure (4.8b) shows the friction vs. carrier density for various carrier mobilities in the semiconductor. The three low mobilities: $\mu = 4 \times 10^{-7}, 2.7 \times 10^{-10}, 6 \times 10^{-14}\,\mathrm{m^2V^{-1}s^{-1}}$ correspond to the range of fast to slow mobilities in organic semiconductors [11]. A mobility corresponding to that of the electron mobility in Si, $\mu = 0.15\,\mathrm{m^2V^{-1}s^{-1}}$, is also shown. While the three low mobilities in organic semiconductors in Fig. (4.8b) exhibit all four carrier density regimes as discussed for the case of non-zero dispersion in Fig. (4.8a), the high electronic mobility of Si in Fig. (4.8b) only shows the asympotic low and high carrier density limits of non-zero dispersion. The peak is absent for the mobilities as high as the electron mobilities in Si. The four carrier density regimes seen in Figs. (4.8a) and (4.8b) are characterized and explained by using the interpretation developed for the frequency regimes of $P_{\delta fc}(f)$ in Fig. (3.3) of Chapter 3. The crossover frequencies in Eqs. (3.34)-(3.36) using which the four frequency regimes are explained for Fig. (3.3), are used to deduce the crossover carrier densities for the case of $\epsilon_{\mathrm{s}}''(\omega_c) << \epsilon_{\mathrm{s}}'(\omega_c)$. This is seen from determining these crossover carrier densities numerically. The friction is plotted for different parameters, and the change in the crossover frequencies with respect to the changed parameters is noted. From the crossover densities thus determined, in retrospect, it is found that these crossover carrier densities can be determined by equating the cantilever resonance frequency to the crossover frequency, and then rearranging the terms to give the three crossover carrier densities,

$$\rho_1 \quad = \quad \frac{\epsilon_{\mathrm{s}}''(\omega_c)}{|\epsilon_{\mathrm{s}}(\omega_c)|^2}\rho_x, \tag{4.17}$$

$$\rho_2 = \frac{|\epsilon_s(\omega_c)|^2}{\epsilon_s'(\omega_c)}\rho_x, \tag{4.18}$$

$$\rho_3 = \left(\frac{|\epsilon_s(\omega_c)|^4 \omega_c d^2}{\left(\epsilon_s''(\omega_c)\right)^2 D}\right)\rho_x, \tag{4.19}$$

$$\rho_x \equiv \frac{\omega_c \epsilon_0}{e\mu}. \tag{4.20}$$

These carrier densities are such that $\rho_1$ is determined from $f_3$, $\rho_2$ from $f_2$, and $\rho_3$ from $f_1$. All three crossover densities scale as $\rho_x$ in Eq. (4.20) which is inversely proportional to mobility. The first two crossover densities $\rho_1$ and $\rho_2$ are independent of tip-sample separation $d$, while the third crossover density $\rho_3 \propto d^2$. $\rho_x$ in Eq. (4.20) is also obtained from the condition $\kappa^2 D = \omega_c$. This condition occurs when the frequency scale associated with a charge carrier diffusing by a Debye screening length in vacuum is equated to the cantilever resonance frequency. With respect to the crossover densities, the four density regimes in Fig. (4.8b) are given physical interpretation similar to the crossover frequency regimes in Fig. (3.3) as follows: $\rho << \rho_1$ corresponds to the regime where friction is solely from the dielectric fluctuation in the sample, and the carrier dynamics is negligible. $\rho_1 < \rho < \rho_2$ corresponds to the regime where the friction is $\propto \rho$, and an analytical expression for friction in this regime is obtained,

$$\gamma_{\parallel} = \frac{q_c^2}{4\pi\epsilon_0\omega_c^2}\left(\frac{\epsilon_s'(\omega_c)}{(1+\epsilon_s'(\omega_c))^2}\right)\left(\frac{\kappa^2 D}{d^3}\right). \tag{4.21}$$

This is the limit where the inter-carrier interactions, and the dielectric fluctuations have negligible contributions to friction, and the carrier density is dilute. A maximum value for friction is seen around $\rho_2$. In the $\rho_2 < \rho < \rho_3$ regime, the contribution from the dielectric fluctuations is negligible while the Coulomb interactions between charge carriers contribute significantly, and friction is inversely proportional to $\rho$,

$$\gamma_{\parallel} = \frac{q_c^2}{16\pi\epsilon_0}\left(\frac{\epsilon_s'(\omega_c)}{\kappa^2 D d^3}\right). \tag{4.22}$$

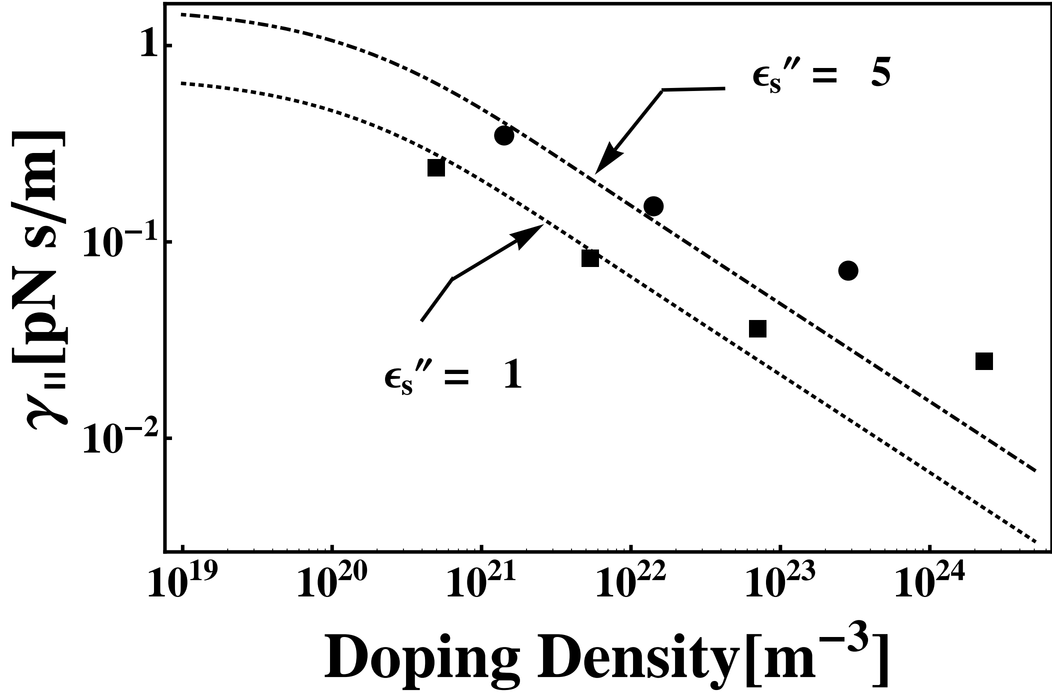


Figure 4.9: Noncontact friction of doped Si vs. doping density at a tip-sample height $d$ = 300 nm. Measured friction values for electrons(squares), and holes(circles) are obtained from Refs.[57, 56]. The curves are calculated from Eq. (4.15), with $\epsilon_s''$ as indicated. The carrier density used in the calculations is equal to the dopant density. The tip-sample voltage is $V_{ts}$ = 2 V. The rest of the parameters are the same as Fig. (4.8), and the experiment.

In the asymptotic high carrier density regime, friction is $\propto \rho^{-1/2}$, and given by

$$\gamma_{\|} = -\frac{3q_c^2}{32\pi\epsilon_0\omega_c d^4}\left(\frac{\mathrm{Im}\sqrt{\epsilon_s(\omega_c)}}{|\epsilon_s(\omega_c)|}\right)\kappa^{-1}. \tag{4.23}$$

In this limit, both the dielectric fluctuations and the inter-carrier interactions contribute to friction. The limits in Eqs. (4.21)-(4.23) are evaluated from Eq. (4.15) for the corresponding regimes. Figure (4.8a) and the limits evaluated in Eqs. (4.21) and (4.22), show that the friction around the peak is independent of dispersion $\epsilon_s''(\omega_c)$. An increase in $\epsilon_s''(\omega_c)$ leads to an increase in the carrier density ($\rho_1$) at which asymptotic low density limit stops, and a decrease in the carrier density ($\rho_3$) at which the asymptotic high density limit starts. For the three

mobilities observed in organic semiconductors, Fig. (4.8b) shows that the peak density increases with decrease in mobility, and the peak shifts to the right as predicted by Eq. (4.18). For a relatively high mobility as that of electron mobility in Si semiconductor, there is no peak seen in Fig. (4.8b).

In Figs. (4.9) and (4.10), a quantitative comparison of the noncontact friction calculated from Eq. (4.15) to the measurements of Stowe, et al. on doped Si samples of n- and p-type are shown. The use of the linear response assumption in Sec. 1.3 for the calculation of noncontact friction is validated by the quadratic dependence on tip-sample voltage of noncontact friction in Ref. [57]. The parameters used for the quantitative comparison are taken from Ref. [57]: cantilever resonance frequency $f_c = 81$ kHz and tip-sample voltage $V_{\mathrm{ts}} = 2$ V. The relative dielectric function is $\epsilon_{\mathrm{s}}(\omega_c) = 11.9 - \epsilon_{\mathrm{s}}''$, with $\epsilon_{\mathrm{s}}''$ taken as an adjustable parameter. The tip radius $R = 80$ nm, and the dielectric constant of Si $\epsilon_{\mathrm{s}}'(0) = 11.9$, are used in Eq. (3.38) for the tip-sample capacitance $c(d)$. Figure (4.9) uses a tip-sample height of $d = 300$nm in Eq. (4.15), and the carrier density is taken to be same as the dopant density of Si [56, 57]. The mobility of holes in Si is $\mu = 0.045\,\mathrm{m^2V^{-1}s^{-1}}$, and the mobility of electrons in Si is $\mu = 0.15\,\mathrm{m^2V^{-1}s^{-1}}$ for the concentrations of the carriers of the order of $10^{20} - 10^{21}\mathrm{m^{-3}}$ [61]. A fit function of mobility as a function of carrier density is obtained from the measured data in Ref. [61] for holes, and electrons in Si. This mobility as a function of carrier density is used in the friction formula in Eq. (4.15). The diffusion constant is obtained using the Einstein relation $D = \mu k_{\mathrm{B}}T/e$ for both electrons and holes. Figure (4.9) shows the friction data [56] from holes, and electrons as circles, and squares, respectively. Both the curves in Fig. (4.9) use the experimental values for all the parameters, except for $\epsilon_{\mathrm{s}}''$ whose value is as indicated. Stowe's friction data [57] show a $\rho^{-1/2}$ dependence in Fig. (4.9). For the mobilities as high as the

mobilities of electrons and holes in Si, the friction calculated from Eq. (4.15) has only the asymptotic low, and high charge density regimes as in Fig. (4.9). For the parameters used from Stowe's measurement [57], the calculated friction is in the asymptotic high carrier density regime as given by Eq. (4.23), in agreement with the $\rho^{-1/2}$ dependence observed for the data. Ref. [57] demonstrated that the friction is $\propto \mu^{-1}$ by plotting $\gamma_{\|}\mu$ for holes and electrons vs. dopant density, and finding it to be a straight line in this range of mobilities and carrier densities. Equation (4.23), the limit applicable for these charge densities, and mobilities, has no mobility dependence from the semi-infinite semiconductor model.

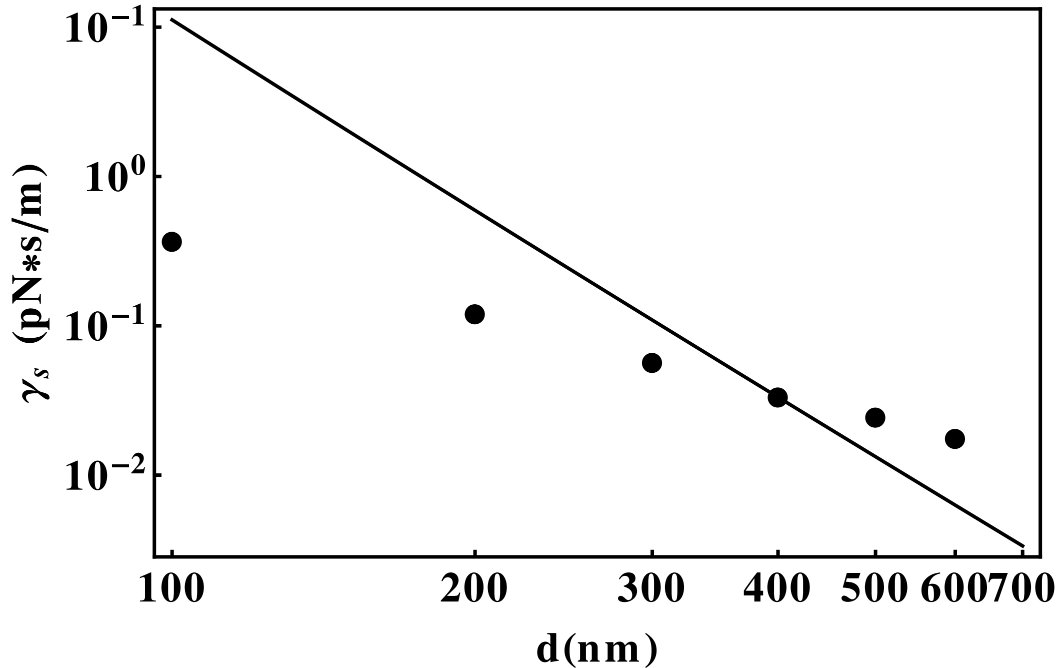


Figure 4.10: Noncontact friction vs. tip-sample height $d$. Dots are the measured friction data from Ref.[57], and the solid line is the friction calculated from Eq. (4.15) for a carrier density of $\rho = 1.4 \times 10^{23}\text{m}^{-3}$. The hole mobility in Si, $\mu = 0.045\ \text{m}^2\text{V}^{-1}\text{s}^{-1}$, $\epsilon''_{\text{rel}} = 5$, and $V_{\text{ts}} = -2$ V are used in the calculation.

Figure (4.10) shows friction vs. tip-sample height $d$. Circles in the figure

are the measured friction data [57], and the solid line in the figure is the calculated friction from Eq. (4.15). The carrier density is calculated using the relation $\rho = 1/(e\mu \times resistivity)$. For a $0.1\Omega$ cm p-type Si sample used in the measurements, the carrier density using this relation is $1.4 \times 10^{23}\,\mathrm{m}^{-3}$. The measured friction shows a dependence of $d^{-2}$, while the calculated friction shows a stronger dependence $d^{-4}$. This discrepancy may be attributed to the use of a simplified model for tip-sample capacitance $c(d)$ in the calculations. The quantitative comparison between the measured, and the calculated friction in Figs. (4.9), and (4.10), is summarized: 1) the calculation of friction using linear response assumption is valid as the measured friction has a quadratic voltage dependence in Ref. [57], 2) calculated friction shows the same $\rho^{-1/2}$ dependence as the measured data, 3) the calculated friction has both contributions from the Coulomb interactions and the dielectric fluctuations in the sample, and the suppression in friction with increase in carrier density is attributed to the inter-carrier interactions in Si at these carrier densities, 4) calculated friction in the range of carrier densities, and mobilities of Stowe data, is mobility independent as opposed to the demonstrated $\mu^{-1}$-dependence of data in Ref. [57], 5) the distance dependence of the calculated friction is stronger than the measured friction, and 6) the magnitude of calculated friction is good fit to the data with $\epsilon_s''$ as the sole parameter.

Figure (4.11) shows the friction predictions from model II for the perpendicular motion of cantilever described in Secs. 1.1.2 and 1.2. Noncontact friction for the perpendicular motion of cantilever is given by Eq. (1.26), and the potential auto-correlation to evaluate this friction is obtained from model II in Sec. 4.2. In Figs. (4.5)-(4.7), in the low frequency range ($f_{\mathrm{min}} = 0.2$ Hz to $f_{\mathrm{max}} = 3$ Hz) pertaining to jitter measurements, the calculations from model II rightly predicted the

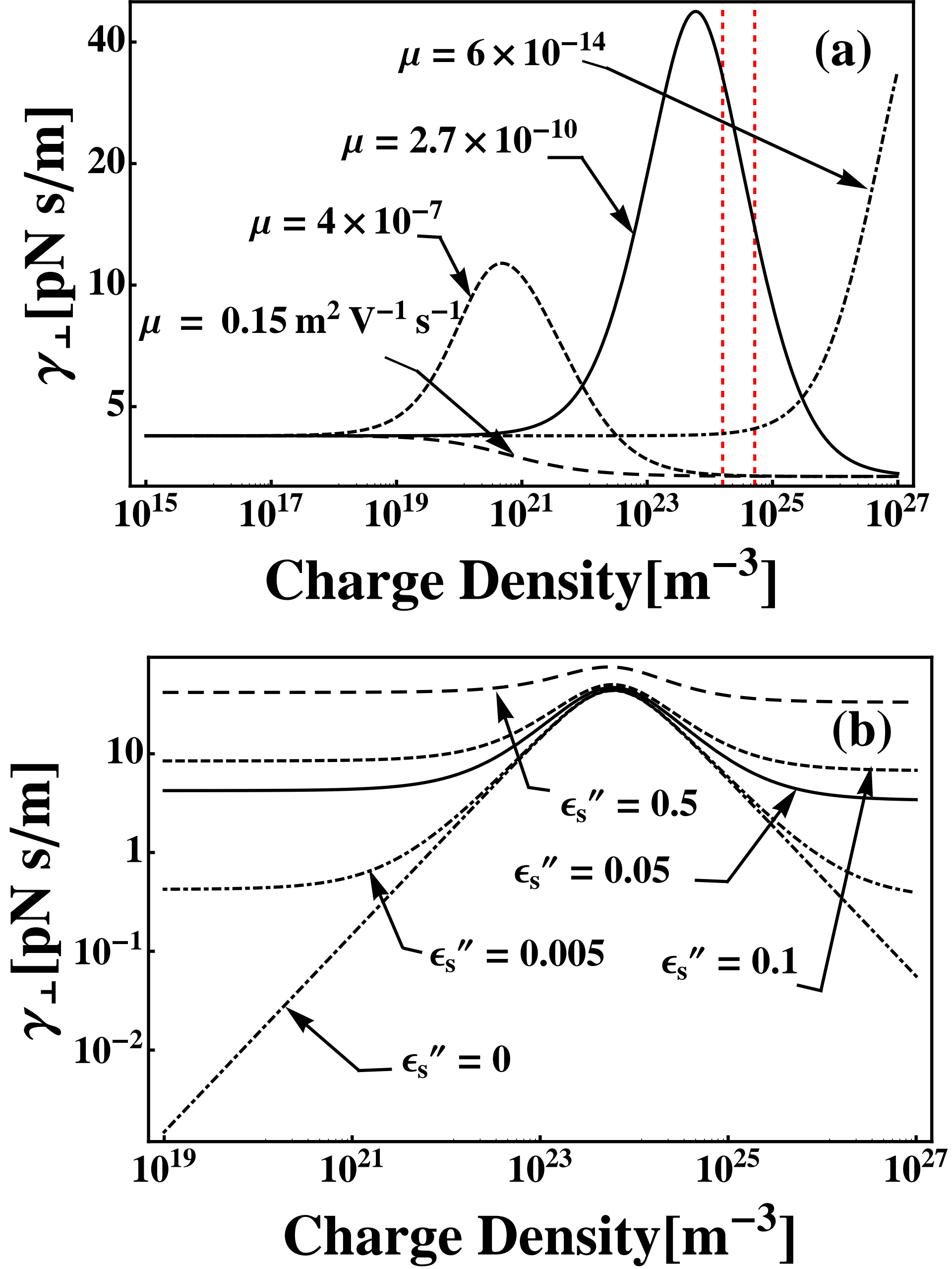


Figure 4.11: Noncontact friction for the perpendicular motion of the cantilever calculated from model II in Sec. 4.2, for an organic transistor. (a) $\gamma_\perp$ vs. carrier density for different carrier mobilities as indicated, with relative dielectric function of the semiconductor and the dielectric overlayer $\epsilon_d = \epsilon_s = 3.4 - i\ 0.05$. Red vertical lines on the $x$-axis correspond to the carrier densities estimated from gate voltages $V_G = -20, -40$ V, explained in the text. (b) $\gamma_\perp$ for various dispersion values $\epsilon_s''$ in the relative dielectric function $\epsilon_d = \epsilon_s = 3.4 - i\ \epsilon_s''$, and $\mu = 2.7\times10^{-10}\,\mathrm{m^2V^{-1}s^{-1}}$. The rest of the parameters are in the text.

carrier density independence of the power spectrum of frequency fluctuations, and the frequency jitter, as observed in EFM measurements on organic transistor in Sec 3.3. Figures (4.5)-(4.7) also predicted that the carrier density dependence is seen at high frequencies, allowing the friction measurements to capture the carrier dynamics. Figures (4.11a) and (4.11b) show these friction versus carrier density predictions for organic semiconductors. Figure (4.11a) shows friction versus the carrier density for different mobilities, and a relative dielectric function $\epsilon_{\mathrm{s}} = \epsilon_{\mathrm{d}} = 3.4 - i\ 0.05$, while Fig. (4.11b) shows the same for a mobility of $\mu = 2.7 \times 10^{-10}\,\mathrm{m^2 V^{-1} s^{-1}}$, and various dispersion values. In model II, the thickness of the dielectric overlayer is $h_{\mathrm{d}} = 69$ nm, and the tip-sample voltage is $V_{\mathrm{ts}} = 3$ V. The tip-sample capacitance $c(d)$ is calculated from Eq. (3.38), with the tip radius $R = 40$ nm, and the relative dielectric constant $\epsilon'_{\mathrm{rel}}(0) = 4$. The long dashed curve in Fig. (4.11a) is the friction for the electronic mobility in Si. This mobility is higher than the other three mobilities in organic semiconductors in the figure. The friction calculated from model II for the high mobility in Si is similar to that calculated for parallel motion of cantilever in Fig. (4.8b) for the same mobility. The three low mobilities that are relevant to organic materials show a peak in friction whose magnitude increases with decrease in mobility. The charge density at which the peak occurs is also inversely proportional to $\mu$. The solid curve in Fig. (4.11a) corresponds to the mobility estimated in the organic transistor in Ref. [32, 20], and the red dashed lines show the carrier densities corresponding to the gate voltages $V_G = -20, -40$ V of transistor in the experiment, estimated to be $\rho = 1.6 \times 10^{24}, 5.2 \times 10^{24}\ \mathrm{m^{-3}}$. The friction calculations in Fig. (4.11a) show that the effect of the carrier dynamics in organic transistor that were not measurable in frequency jitter, can be measured in a friction measurement. Figure (4.11a) uses a arbitrary relative dielectric function as the relative dielectric function of

the organic semiconductor is unknown (Sec. 3.3). Figure (4.11b) shows friction vs. carrier density for the transistor mobility for various dispersion values. For a particular mobility, it is seen in Fig. (4.11b) that increasing the dispersion $\epsilon_s''(\omega_c)$ does not change the peak location of friction, but the effects of carrier dynamics will be masked by the dielectric fluctuations in the sample for a high value of $\epsilon_s''(\omega_c)$.

## 4.4 Summary

The spectral density of frequency fluctuations and the frequency jitter from model I where there is a finite thickness for semiconductor on a dielectric base, are shown. These calculations are shown to be not different from semi-infinite semiconductor presented in Chapter 3, for the thickness of the organic semiconductor $h_s = 70$ nm in transistor. Significant finite thickness effects are seen only for small thicknesses $h_s = 1, 10$ nm from model I. The spectral density of frequency fluctuations, and the frequency jitter calculations from model II where there is a dielectric overlayer on a semi-infinite semiconductor are shown. This model includes the well-known physical feature in the organic transistor, the confinement of the charge carriers to about one nanometer at the semiconductor-$SiO_2$ interface. These calculations exhibited the same carrier density independence around 1 Hz similar to that observed in the EFM experiments[32, 20] for the corresponding gate voltages. The dielectric overlayer of thickness 69 nm is shown to significantly screen the suppression of frequency noise from semi-infinite semiconductor giving approximately the same result as the dielectric. The calculated jitter from model II is quantitatively compared to the jitter measurements on the organic transistor from Chapter 3. While

jitter magnitude is fitted with a large dispersion value in the dielectric function, a stronger tip-sample height dependence of jitter is observed in the calculation. The stronger tip-sample height dependence may be attributed to the the use of a simplified tip-sample capacitance expression in the jitter calculations.

The calculations from model II not only explain the jitter measurements on organic transistor, but also predict that the carrier dynamics may be seen at higher frequencies that are accessible in a friction measurement for a cantilever oscillating in a perpendicular motion. It is shown that the friction versus carrier density calculations for the organic transistor exhibit a peak at a density, and the location is inversely proportional to the carrier mobility. Depending on the carrier mobility and the carrier density in the transistor the friction measurements may fall into four different regimes: $\propto \rho^0$, $\propto \rho$, $\propto \rho^{-1}$, or $\propto \rho^{-1/2}$. It is also shown that increasing the dispersion $\epsilon_s''$ of the dielectric overlayer leads to masking of the carrier dynamics effects by stronger dielectric fluctuations in the friction calculations.

Noncontact friction measurements of Stowe, et.al. [57, 56] for the parallel motion of the cantilever on doped Si are shown, and quantitatively compared to the friction calculations from the semi-infinite semiconductor model applicable to this geometry. The friction vs. carrier density calculations are shown for the parallel motion of cantilever for different mobilities and dispersion values, and the same four regimes in the friction calculations for perpendicular motion of the cantilever for the organic transistor are seen. The calculations from the semiconductor model, particularly for the electronic and hole mobilities in Si, showed the same $\rho^{-1/2}$ dependence as observed in the Stowe data [57]. The magnitude of the friction is also fit with $\epsilon_s''$ as the sole adjustable parame-

ter. The stronger distance dependence observed in the calculation is attributed to the simplified tip-sample capacitance model, and the demonstrated mobility dependence of friction through arguments in Ref. [57] is not seen from the calculations. The suppression of friction with increase in carrier density is shown to arise from the inter-carrier interactions and the dielectric fluctuations in doped Si.

CHAPTER 5

# CONCLUDING REMARKS

Electric force microscopy employs a charged cantilever tip to sense the fluctuating electrical forces from a sample. The cantilever tip experiencing these fluctuating electrical forces is modelled as a point charge using the Langevin equation. The fluctuating electrical forces at the cantilever tip are obtained from the stochastic potential energy of the tip-sample system. These electrical forces from the sample are linked to the experimental observables in EFM: the frequency jitter that measures low frequency dynamics in the sample, and the noncontact friction that measures high frequency dynamics in the sample. These observables are calculable using a classical mechanical treatment based on linear response theory and classical electrodynamics of the tip-sample arrangement in the point charge model. The presence of charge carriers in the sample requires additionally a transport equation for the carriers in coupling to the Maxwell's equations. This macroscopic treatment implicitly includes carrier interactions and coupling between carrier dynamics and dielectric fluctuations which is not possible in the calculation of experimental observables from random walk models. The microscopic treatments that are generally used to study charge motion in organic semiconductors neglect long-range inter-carrier Coulomb interactions which are included in this macroscopic theory. The theory presented here moreover treats the coupling of charge carriers to molecular motions at the interface between two different materials.

The EFM observables thus calculated are related to the sample properties: molecular motions, carrier dynamics and inter-carrier interactions. Cantilever frequency jitter measurements on organic thin-film polymers are related to

molecular motions in polymers via the dielectric spectrum of the polymer. In principle, frequency jitter measurements on a sample with charge carriers are capable of probing the dielectric fluctuations, carrier dynamics, and inter-carrier interactions. In the experiment, what is probed depends on the sample geometry and the interplay between dielectric fluctuations, carrier dynamics, and inter-carrier interactions. A frequency jitter measurement on an organic transistor with an organic semiconductor thickness of 70 nm only probes dielectric fluctuations even when the gate voltage is varied to adjust the carrier concentration in the semiconductor sample. In an organic transistor, the charge carriers are confined to a few monolayers at the semiconductor-dielectric interface and the noise at low frequencies in a jitter measurements is screened by the semiconductor layers on the top of these few monlayers. The noncontact friction calculations predict that for attainable gate voltages in a typical organic transistor, carrier dynamics and inter-carrier interactions can be characterized in an organic semiconductor sample via a friction measurement.

# APPENDIX A
## APPENDIX TO CHAPTER 3

Maxwell's equations in the semiconductor are given by Eqs. (3.1)-(3.3). The current density **J** is taken to be related to charge density and electric field by Eq. (3.4). Here, the approach in Refs.[14, 59] is shown in detail to obtain the final form of current in Eq. (3.4). In this approach a simplifying assumption that both the positive, and the negative charge carriers have same dynamics is made. This current density is obtained from the general expression for the current density, in terms of the charge density $n$ (in Coulomb per cubic metre), and the mean velocity of carriers $\mathbf{v}$, $\mathbf{J} \equiv n\mathbf{v}$, and the Boltzmann transport equation given by

$$\left(\frac{\partial}{\partial t} + \mathbf{v}.\nabla\right)\mathbf{v} = -\frac{e}{m}\mathbf{E} - \frac{v_T^2}{n}\nabla n - \frac{\mathbf{v}}{\tau}, \tag{A.1}$$

where $m$ is the effective mass of the carriers in sample, $v_T$ is the thermal velocity given by $(k_B T/m)^{1/2}$, $T$ is the temperature, $k_B$ is the Boltzmann constant, $-e$ is the electronic charge, and $\tau$ is the relaxation time of the carriers. The charge density $n$ is written as a sum of two terms: a static part $n_0$ which is constant throughout space, and a spatially and temporally varying term $n(\mathbf{r})e^{i\omega t}$. Similarly, the static part of the mean velocity of carriers (drift) due to the external applied field is taken as 0 in this treatment, and the temporally and spatially varying term is $\mathbf{v}e^{i\omega t}$. Eq. (A.1) is linearized in $e^{i\omega t}$, and this gives

$$\left(i\omega + \frac{1}{\tau}\right)\mathbf{v} = -\frac{e}{m}\mathbf{E} - \frac{v_T^2}{n_0}\nabla n. \tag{A.2}$$

The assumption $\frac{1}{\tau} >> \omega$ is made next. The terms in Eq. (A.2) are rearranged to obtain the velocity as

$$\mathbf{v} = -\frac{e\tau}{m}\mathbf{E} - \frac{v_T^2\tau}{n_0}\nabla n. \tag{A.3}$$

Equation (A.3) is written in terms of the mobility of the carrier $\mu = e\tau/m$, and the diffusion constant $D = v_T^2\tau$, and substituted in the expression for current density $\mathbf{J} = n\mathbf{v}$. This is again linearized in $e^{i\omega t}$, and written in terms of the conductivity $\sigma_0 = -n_0\mu$ to give the final form in Eq. (3.4) which is then written in terms of electric field using Eq. (3.3) as follows

$$\mathbf{J} = \sigma_0\mathbf{E} - D\nabla n, \tag{A.4}$$

$$= \sigma_0\mathbf{E} - \epsilon(\omega)D\nabla(\nabla.\mathbf{E}) \tag{A.5}$$

Combining Eqs. (3.1), (3.2), and (A.5) gives the second-order differential equation for the electric field in Eq. (3.6). Here the following well known property for the curl is used.

$$\nabla \times (\nabla \times \mathbf{E}) = \nabla(\nabla.\mathbf{E}) - \nabla^2\mathbf{E} \tag{A.6}$$

The vector field equation in Eq. (3.6) is then written in terms of the electric field components $E_x$ and $E_z$. This gives the coupled equations for of $E_x$ and $E_z$, in Eq. (3.9)

Here the steps going from the second-order coupled equations in Eq. (3.9) to the fourth order uncoupled equations in Eq. (3.11) are shown. The first second-order coupled equation in Eq. (3.9) has the form

$$\frac{\partial^2 \hat{E}_x}{\partial z^2} + a\hat{E}_x = b\frac{\partial \hat{E}_z}{\partial z}, \tag{A.7}$$
$$a = \left(\tilde{s}^2 - ik^2\frac{Ds^2}{\omega}\right),$$
$$b = -ik\left(1 - \frac{is^2D}{\omega}\right),$$

. Equation (A.7) is differentiated twice with respect to z to give

$$\frac{\partial^4 \hat{E}_x}{\partial z^4} + a\frac{\partial^2 \hat{E}_x}{\partial z^2} = b\frac{\partial^3 \hat{E}_z}{\partial z^3}. \tag{A.8}$$

The term on the right hand side in Eq. (A.8) $\partial^3 \hat{E}_z/\partial z^3$, is obtained from the other coupled equation in Eq. (3.9) written as follows,

$$
\begin{aligned}
& d\frac{\partial^2 \hat{E}_z}{\partial z^2} + c\hat{E}_z = b\frac{\partial \hat{E}_x}{\partial z}, \\
& c = \left(\tilde{s}^2 - k^2\right), \\
& d = \frac{iDs^2}{\omega},
\end{aligned} \tag{A.9}
$$

after differentiating with respect to $z$ once. This when substituted into Eq. (A.8) gives

$$
\frac{\partial^4 \hat{E}_x}{\partial z^4} + a\frac{\partial^2 \hat{E}_x}{\partial z^2} = \frac{b^2}{d}\frac{\partial^2 \hat{E}_x}{\partial z^2} - \frac{bc}{d}\frac{\partial \hat{E}_z}{\partial z}. \tag{A.10}
$$

Using Eq. (A.7) in Eq. (A.10) gives the fourth order differential equation for $E_x$ in Eq. (3.11)

$$
\frac{\partial^4 \hat{E}_x}{\partial z^4} + (a - b^2/d + c/d)\frac{\partial^2 \hat{E}_x}{\partial z^2} + \frac{ac}{d}\hat{E}_x = 0. \tag{A.11}
$$

It can be easily shown that $ac/d = \eta_-^2\eta_+^2$, and $(a - b^2/d + c/d) = -\eta_-^2 - \eta_+^2$, using Eqs. (3.12), (3.13), and the definitions of the variables: a, b, c, and d from above. Similar derivation for $E_z$ gives the fourth order uncoupled equation for $E_z$, which has the same form as Eq. (A.11).

APPENDIX B

# APPENDIX TO CHAPTER 4

The boundary conditions for model I in Sec. 4.1, and model II in Sec. 4.2 are shown here. For model I, the continuity conditions for $E_x$, $\epsilon(\omega)E_z$ and $H_y$ at the vacuum-semiconductor interface at $z = 0$ are written. The equations for the fields in vacuum are Eqs. (2.9)-(2.11) and contain one unknown amplitude $A_{\text{rxn}}$. The fields in semiconductor for model I are given by Eqs. (4.1)-(4.3) and contain unknown amplitudes $A_{++}$, $A_{+-}$, $A_{-+}$, and $A_{--}$. Substituting $z = 0$ in these field equations, and equating the corresponding fields in vacuum and the semiconductor gives the boundary conditions at the vacuum-sample interface as

$$A_{++} + A_{+-} + A_{-+} + A_{--} = \frac{i\tilde{k}}{k}\left(\frac{q(z_1,\omega)}{2\epsilon_0}\right)e^{-\tilde{k}z_1} + \frac{i\tilde{k}}{k}A_{\text{rxn}}, \tag{B.1}$$

$$\epsilon_{\text{s}}(\omega)\left(\frac{i\eta_+}{k}(A_{++} - A_{+-}) + \frac{ik}{\eta_-}(A_{-+} + A_{--})\right) = -\frac{q(z_1,\omega)}{2\epsilon_0}e^{-\tilde{k}z_1} + A_{\text{rxn}}, \tag{B.2}$$

$$\frac{i\tilde{s}^2}{\eta_-}(A_{-+} - A_{--}) = \frac{\omega^2}{kc^2}\left(-\frac{q(z_1,\omega)}{2\epsilon_0}e^{-\tilde{k}z_1} + A_{\text{rxn}}\right). \tag{B.3}$$

Similarly, the boundary conditions at the semiconductor-dielectric interface at $z = -h_{\text{s}}$ are written using the field equations in the semiconductor in Eqs. (4.1)-(4.3), and the field equations in the dielectric in Eqs. (4.4)-(4.7), which contain the unknown amplitude $C$.

$$A_{++}e^{-\eta_+h_{\text{s}}} + A_{+-}e^{\eta_+h_{\text{s}}} + A_{-+}e^{-\eta_-h_{\text{s}}} + A_{--}e^{\eta_-h_{\text{s}}} = Ce^{-\eta h_{\text{s}}}, \tag{B.4}$$

$$\frac{i\eta_+}{k}(A_{++}e^{-\eta_+h_{\text{s}}} - A_{+-}e^{\eta_+h_{\text{s}}}) + \frac{ik}{\eta_-}(A_{-+}e^{-\eta_-h_{\text{s}}} + A_{--}e^{\eta_-h_{\text{s}}}) = \frac{ik\epsilon_{\text{d}}(\omega)}{\eta\epsilon_{\text{s}}(\omega)}Ce^{-\eta h_{\text{s}}}, \tag{B.5}$$

$$\frac{\tilde{s}^2}{\eta_-}(A_{-+}e^{-\eta_-h_{\text{s}}} - A_{--}e^{-\eta_-h_{\text{s}}}) = \frac{\omega^2\epsilon_d(\omega)}{\eta c^2}Ce^{-\eta h_{\text{s}}}. \tag{B.6}$$

Eqs. (B.1)-(B.6) are 6 equations in 6 unknowns, and these are soluble to obtain $A_{\text{rxn}}$ for model I as in Eq. (4.8) with $\theta_{\text{I}}$ given by Eq. (4.9).

Similarly, for model II in Fig. (4.2), the boundary conditions at the vacuum-dielectric interface at $z = 0$ and at the dielectric-semiconductor interface at $z = -h_\mathrm{d}$ are shown. Using the field equations in vacuum in Eqs. (2.9)-(2.11), and the field equations of the dielectric Eqs. (2.12)-(2.14), which contaun the unknown amplitudes $C_1$ and $C_2$, the boundary conditions at the interface at $z = 0$ are written as follows,

$$\frac{i\tilde{k}}{k}\left(\frac{q(z_1,\omega)}{2\epsilon_0}\right)e^{-\tilde{k}z_1} + \frac{i\tilde{k}}{k}A_\mathrm{rxn} = C_1 + C_2, \tag{B.7}$$

$$-\frac{q(z_1,\omega)}{2\epsilon_0}e^{-\tilde{k}z_1} + A_\mathrm{rxn} = \frac{ik\epsilon_\mathrm{d}}{\tilde{\eta}}(C_1 - C_2). \tag{B.8}$$

The continuity conditions of $\epsilon(\omega)E_z$ and $H_y$ at the vacuum-dielectric interface are the same, and hence at this interface only two conditions Eqs. (B.7), and (B.8) are obtained. The boundary conditions at the dielectric-semiconductor interface at $z = -h_\mathrm{d}$ are written using the field equations in the dielectric Eqs. (2.12)-(2.14), and the field equations in the semiconductor Eqs. (3.15)-(3.17) as shown below.

$$C_1e^{-\tilde{\eta}h_\mathrm{d}} + C_2e^{\tilde{\eta}h_\mathrm{d}} = A_+e^{-\eta_+h_\mathrm{d}} + A_-e^{-\eta_-h_\mathrm{d}}, \tag{B.9}$$

$$\frac{k\epsilon_\mathrm{d}(\omega)}{\tilde{\eta}\epsilon_\mathrm{s}(\omega)}(C_1e^{-\tilde{\eta}h_\mathrm{d}} - C_2e^{\tilde{\eta}h_\mathrm{d}}) = \frac{\eta_+A_+}{k}e^{-\eta_+h_\mathrm{d}} + \frac{kA_-}{\eta_-}e^{-\eta_-h_\mathrm{d}}, \tag{B.10}$$

$$\frac{\epsilon_\mathrm{d}(\omega)}{\tilde{\eta}c^2}(C_1e^{-\tilde{\eta}h_\mathrm{d}} - C_2e^{\tilde{\eta}h_\mathrm{d}}) = \frac{\tilde{s}}{\eta_-}A_-e^{-\eta_-h_\mathrm{d}}. \tag{B.11}$$

The 5 boundary conditions in Eqs. (B.7)-(B.11), when solved for the 5 unknown amplitudes give $A_\mathrm{rxn}$ for model II in Eq. (4.12) with $\theta_\mathrm{II}$ given by Eq. (4.13).

## BIBLIOGRAPHY


[1] T. R. Albrecht, P. Grütter, D. Horne, and D. Rugar. Frequency modulation detection using high-Q cantilevers for enhanced force microscopy sensitivity . *J. Appl. Phys.*, 69:668–673, 1991.

[2] J. A. Barker, C. M. Ramsdale, and N. C. Greenham. Modeling the current-voltage characteristics of bilayer polymer photovoltaic devices . *Phys. Rev. B*, 67:075205, 2003.

[3] H. Bässler. Charge Transport in Disordered Organic Photoconductors a Monte Carlo Simulation Study . *Phys. Status Solidi B*, 175:15–56, 1993.

[4] G. Binnig, H. Rohrer, Ch. Gerber, and E. Weibel. Tunneling through a controllable vacuum gap. *Appl. Phys. Lett.*, 40:178, 1982.

[5] P. M. Borsenberger and D. S. Weiss. *Organic Photoreceptors For Xerography*. Marcel Dekker, New York, 1998.

[6] M. Bouhassoune, S.L.M. van Mensfoort, P.A. Bobbert, and R. Coehoorn. Carrier-density and field-dependent charge-carrier mobility in organic semiconductors with correlated Gaussian disorder. *Org. Electron.*, 10:437–445, 2009.

[7] L. Bürgi, H. Sirringhaus, and R. H. Friend. Noncontact potentiometry of polymer field-effect transistors . *Applied Physics Letters*, 80:2913–2915, 2002.

[8] A. Carbone, B. K. Kotowska, and D. Kotowski. Space-Charge-Limited Current Fluctuations in Organic Semiconductors . *Phys. Rev. Lett.*, 95:236601, 2005.

[9] A. Carbone, C. Pennetta, and L. Reggiani. Trapping-detrapping fluctuations in organic space-charge layers. *Appl. Phys. Lett.*, 95:233303, 2009.

[10] O. Cherniavskaya, L. Chen, V. Weng, L. Yuditsky, and L. E. Brus. Quantitative noncontact electric force imaging of nanocrystal polarizability . *J. Phys. Chem. B*, 107:1525–1531, 2003.

[11] L.-L. Chua, J. Zaumseil, J.-F. Chang, E. C.-W. Ou, P K.-H. Ho, H. Sirringhaus, and R. H. Friend. General observation of n-type field-effect behaviour in organic semiconductors . *Nature*, 434:194–199, 2005.

[12] P. S. Crider, M. R. Majewski, Jingyun Zhang, H. Ouckris, and N. E. Israeloff. Local dielectric spectroscopy of polymer films. *Appl. Phys. Lett.*, 91:013102, 2007.

[13] P. S. Crider, M. R. Majewski, Jingyun Zhang, H. Ouckris, and N. E. Israeloff. Local dielectric spectroscopy of near-surface glassy polymer dynamics. *J. Chem. Phys.*, 128:044908, 2008.

[14] D. A. R. Dalvit and S. K. Lamoreaux. Contribution of drifting carriers to the Casimir-Lifshitz and Casimir-Polder interactions with semiconductor materials. *Phys. Rev. Lett.*, 101:163203, 2008.

[15] W. Denk and D. W. Pohl. Local electrical dissipation imaged by scanning force microscopy . *Appl. Phys. Lett.*, 59:2171–2173, 1991.

[16] I. Dorofeyev, H. Fuchs, G. Wenning, and B. Gotsmann. Brownian motion of microscopic solids under the action of fluctuating electromagnetic fields. *Phys. Rev. Lett.*, 83:2402–2405, 1999.

[17] D. H. Dunlap, P. E. Parris, and V. M. Kenkre. Charge-dipole model for the universal field dependence of mobilities in molecularly doped polymers. *Phys. Rev. Lett.*, 77:542–545, 1996.

[18] I. I. Fishchuk, V. I. Arkhipov, A. Kadashchuk, P. Heremans, and H. Bässler. Analytic model of hopping mobility at large charge carrier concentrations in disordered organic semiconductors: polarons versus bare charge carriers . *Phys. Rev. B*, 80:045210, 2007.

[19] H. Goldstein, C. P. Poole, and J. L. Safko. *Classical Mechanics*. 545-547. Addison Wesley, Menlo Park, CA, 2002.

[20] N. Hoepker. *Fluctuations near thin organic films, organic photovoltaics, and organic semiconductors as determined by electric force microscopy*. PhD thesis, Cornell University, 2012.

[21] N. Hoepker, S. Lekkala, R. F. Loring, and J. A. Marohn. Dielectric fluctuations over polymer films detected using an atomic force microscope . *J. Phys. Chem. B*, 115:14493–14500, 2011.

[22] P. M. Hoffmann, S. Jeffery, J. B. Pethica, H. O. Ozer, and A. Oral. Energy dissipation in atomic force microscopy and atomic loss processes . *Phys. Rev. Lett.*, 87:265502, 2001.

[23] N. E. Israeloff and T. S. Grigera. Low frequency dielectric fluctuations near the glass transition . *Europhys. Lett.*, 43:308–313, 1998.

[24] J. D. Jackson. *Classical Electrodynamics*. Wiley, New York, 1975.

[25] Michael Jaquith, Erik M. Muller, and John A. Marohn. Time-Resolved Electric Force Microscopy of Charge Trapping in Polycrystalline Pentacene. *J. Phys. Chem. B*, 111:7711–7714, 2007.

[26] N. E. Jenkins, L. P. DeFlores, J. Allen, T. N. Ng, S. R. Garner, S. Kuehn, J. M. Dawlaty, and J. A. Marohn. Batch fabrication and characterization of ultrasensitive cantilevers with submicron tips. *J. Vac. Sci. Tech. B*, 22, 2004.

[27] S. V. Kalinin and A. Gruverman, editors. *Scanning probe microscopy: electrical and electromechanical phenomena at the nanoscale*. Springer, New York, 2007.

[28] M. Kemerink, T. Hallam, M. J. Lee, N. Zhao, M. Caironi, and H. Sirringhaus. Temperature- and density-dependent channel potentials in high-mobility organic field-effect transistors . *Phys. Rev. B*, 80:115325, 2009.

[29] M. Kiguchi, M. Nakayama, T. Shimada, and K. Saiki. Electric-field-induced charge injection or exhaustion in organic thin film transistor. *Phys. Rev. B*, 71:035332, 2005.

[30] S. Kuehn, R. F. Loring, and J. A. Marohn. Dielectric fluctuations and the origin of noncontact friction . *Phys. Rev. Lett.*, 96:156103, 2006.

[31] S. Kuehn, J. A. Marohn, and R. F. Loring. Noncontact dielectric friction . *J. Phys. Chem. B*, 110:14525–14528, 2006.

[32] S. Lekkala, N. Hoepker, J. A. Marohn, and R. F. Loring. Probing charge carrier dynamics with an electric force microscope. *J. Chem. Phys.*, 137:ABC123, 2012.

[33] Y. Martin, D. W. Abraham, and H. K. Wickramasinghe. High-resolution capacitance measurement and potentiometry by force microscopy. *Appl. Phys. Lett.*, 52:1103–1105, 1988.

[34] Y. Martin, C. C. Williams, and H. K. Wickramasinghe. Atomic force microscope-force mapping and profiling on a sub 100-Å scale. *J. Appl. Phys.*, 61:4723–4729, 1987.

[35] J. Nelson. Diffusion-limited recombination in polymer-fullerene blends and its influence on photocurrent collection. *Phys. Rev. B*, 67:155209, 2003.

[36] T. N. Ng, W. R. Silveira, and J. A. Marohn. The dependence of charge injection on temperature, electric field, and energetic disorder in an organic semiconductor. *Phys. Rev. Lett.*, 98:066101, 2007.

[37] M. Nonnenmacher, M. P. Boyle, and H. K. Wickramasinghe. Kelvin probe force microscopy. *Appl. Phys. Lett.*, 58:2921, 1991.

[38] S. V. Novikov, D. H. Dunlap, V. M. Kenkre, P. E. Parris, and A. V. Vannikov. Essential role of correlations in governing charge transport in disordered organic materials. *Phys. Rev. Lett.*, 81:4472–4475, 1998.

[39] Yu. Obukhov, K. C. Fong, D. Daughton, and P. C. Hammel. Real time cantilever signal frequency determination using digital signal processing . *J. Appl. Phys.*, 101:034315, 2007.

[40] J. Y. Park, D. F. Ogletree, P. A. Thiel, and M. Salmeron. Influence of carrier density on the friction properties of silicon pn junctions. *Phys. Rev. B*, 76:064108, 2007.

[41] W. F. Pasveer, J. Cottaar, C. Tanase, R. Coehoorn, P. A. Bobbert, P. W. M. Blom, D. M. de Leeuw, and M. A. J. Michels. Unified Description of Charge-Carrier Mobilities in Disordered Semiconducting Polymers. *Phys. Rev. Lett.*, 94:206601, 2005.

[42] A. Pathak and S. Mandal. Classical and quantum oscillators of quartic anharmonicities: second-order solution. *Phys. Lett. A*, 286:261–276, 2001.

[43] B. N. J. Persson and Z. Zhang. Theory of friction: Coulomb drag between closely spaced solids. *Phys. Rev. B*, 57:7327–7334, 1998.

[44] L. P. Pitaevskii. Thermal Lifshitz force between an atom and a conductor with a small density of carriers . *Phys. Rev. Lett.*, 101:163202, 2008.

[45] Y. Qi, J. Y. Park, B. L. M. Hendriksen, D. F. Ogletree, and M. Salmeron. Electronic contribution to friction on GaAs: An atomic force microscope study . *Phys. Rev. B*, 77:184105, 2008.

[46] Kubo R. Statistical-mechanical theory of irreversible processes. *Journal of the Physical Society of Japan*, 12(6):570–586, 1957.

[47] R. Richert. The dielectric modulus: relaxation versus retardation. *Solid State Ionics*, 105:167–173, 1998.

[48] E. M. Roeling, W. C. Germs, B. Smalbrugge, E. J. Geluk, T. de Vries, R. A. J. Janssen, and M. Kemerink. Organic electronic ratchets doing work . *Nature Mater.*, 10:51–55, 2011.

[49] R. Ruiz, A. Papadimitratos, A. Mayer, and G. Malliaras. Thickness dependence of mobility in pentacene thin-film transistors. *ADVANCED MATERIALS*, 17:1795, 2005.

[50] E. Vidal Russell and N. E. Israeloff. Direct observation of molecular cooperativity near the glass transition . *Nature*, 408:695–698, 2000.

[51] E. Vidal Russell, N. E. Israeloff, L. E. Walther, and H. Alvarez Gomariz. Nanometer scale dielectric fluctuations at the glass transition . *Phys. Rev. Lett.*, 81:1461–1464, 1998.

[52] Jian-Huang She and Alexander V Balatsky. Noncontact friction and relaxational dynamics of surface defects. *Physical Review Letters*, 108(13):136101, 2012.

[53] Yulong Shen, Matthias W. Klein, Daniel B. Jacobs, J. Campbell Scott, and George G. Malliaras. Mobility-dependent charge injection into an organic semiconductor. *Phys. Rev. Lett.*, 86:3867–3870, 2001.

[54] W. R. Silveira and J. A. Marohn. Microscopic view of charge injection in an organic semiconductor. *Phys. Rev. Lett.*, 93:116104, 2004.

[55] B. C. Stipe, H. J. Mamin, T. D. Stowe, T. W. Kenny, and D. Rugar. Noncontact friction and force fluctuations between closely spaced bodies. *Phys. Rev. Lett.*, 87:96801, 2001.

[56] T. D. Stowe. *Chapter 7. Probing electrical dissipation near surfaces*. PhD thesis, Stanford University, 2000.

[57] T. D. Stowe, T. W. Kenny, D. J. Thompson, and D. Rugar. Silicon dopant imaging by dissipation force microscopy. *Appl. Phys. Lett.*, 75:2785–2787, 1999.

[58] T. D. Stowe, K. Yasumura, T. W. Kenny, D. Botkin, K. Wago, and D. Rugar.

Attonewton force detection using ultrathin silicon cantilevers. *Appl. Phys. Lett.*, 71:288–290, 1997.

[59] M. Sumi. Traveling wave amplification by drifting carriers in semiconductors . *Jpn. J. Appl. Phys.*, 6:688–698, 1966.

[60] V. B. Svetovoy. Application of the Lifshitz theory to poor conductors . *Phys. Rev. Lett.*, 101:163303, 2008.

[61] S. M. Sze. *Physics of Semiconductor Devices* . Wiley, Reading, MA, 1981.

[62] O. Tal, I. Epstein, O. Snir, Y. Roichman, Y. Ganot, C. K. Chan, A. Kahn, N. Tessler, and Y. Rosenwaks. Measurements of the Einstein relation in doped and undoped molecular thin films. *Physical Review B*, 77(20):201201, 2008.

[63] O. Tal, Y. Rosenwaks, Y. Preezant, N. Tessler, C. K. Chan, and A. Kahn. Direct Determination of the Hole Density of States in Undoped and Doped Amorphous Organic Films with High Lateral Resolution . *Phys. Rev. Lett.*, 95:256405, 2005.

[64] L. E. Walther, N. E. Israeloff, E. Vidal Russell, and H. Alvarez Gomariz. Mesoscopic scale dielectric relaxation at the glass transition . *Phys. Rev. B*, 57:112–115, 1998.

[65] L. E. Walther, E. Vidal Russell, N. E. Israeloff, and H. Alvarez Gomariz. Atomic force measurement of low-frequency dielectric noise . *Appl. Phys. Lett.*, 72:3223–3225, 1998.

[66] U. Wolf, V. I. Arkhipov, and H. Bässler. Current injection from a metal to a disordered hopping system. I. monte carlo simulation. *Phys. Rev. B*, 59:7507, 1999.

[67] S. M. Yazdanian. *Scanned probe microscopy studies of thin organic films using cantilever frequency noise*. PhD thesis, Cornell University, August 2009.

[68] S. M. Yazdanian, N. Hoepker, S. Kuehn, R. F. Loring, and J. A. Marohn. Quantifying Electric Field Gradient Fluctuations over Polymers Using Ultrasensitive Cantilevers. *Nano Lett.*, 9, 2009.

[69] S. M. Yazdanian, J. A. Marohn, and R. F. Loring. Dielectric fluctuations in

force microscopy: noncontact friction and frequency jitter . *J. Chem. Phys.*, 128:224706, 2008.

[70] Y. Zhang and P. W. M. Blom. Electron and hole transport in poly(fluorene-benzothiadiazole) . *Appl. Phys. Lett.*, 98:143504, 2011.